



**METHODS FOR ESTIMATING USER  
POSITION IN THE NEAR-FIELD REGIME**

**LARISSA AIDÊ ARAÚJO ROCHA**

**DISSERTAÇÃO DE MESTRADO  
EM ENGENHARIA ELÉTRICA**

**DEPARTAMENTO DE ENGENHARIA ELÉTRICA**

**FACULDADE DE TECNOLOGIA  
UNIVERSIDADE DE BRASÍLIA**

Universidade de Brasília  
Faculdade de Tecnologia  
Departamento de Engenharia Elétrica

Methods for Estimating User Position in the Near-Field Regime

Larissa Aidê Araújo Rocha

DISSERTAÇÃO DE MESTRADO SUBMETIDA AO PROGRAMA DE  
PÓS-GRADUAÇÃO EM ENGENHARIA ELÉTRICA DA UNIVERSIDADE DE  
BRASÍLIA COMO PARTE DOS REQUISITOS NECESSÁRIOS PARA A OB-  
TENÇÃO DO GRAU DE MESTRE.

APROVADA POR:

---

Prof. Dr. Daniel Costa Araujo, Universidade de Brasília - UnB  
(Orientador)

---

Prof. Dr. Felix Dieter Antreich, Instituto Tecnológico de Aeronáutica - ITA  
(Examinador Externo)

---

Prof. Dr. Adoniran Judson de Barros Braga, Universidade de Brasília - UnB  
(Examinador Interno)

Brasília/DF, maio de 2024.

## FICHA CATALOGRÁFICA

ROCHA, LARISSA

Methods for Estimating User Position in the Near-Field Regime. [Brasília/DF] 2024.

xxx, nnnp., 210 x 297 mm (ENE/FT/UnB, Mestre, Dissertação de Mestrado, 2024).

Universidade de Brasília, Faculdade de Tecnologia, Departamento de Engenharia Elétrica.

Departamento de Engenharia Elétrica

- |                    |                   |
|--------------------|-------------------|
| 1. Near-Field      | 2. DOA            |
| 3. User's Location | 4. Sub-array      |
| 5. ELAA            | 6. 3D Positioning |
| 7. URA             | 8. HOSVD          |
| I. ENE/FT/UnB      | II. Título        |

## REFERÊNCIA BIBLIOGRÁFICA

ROCHA, LARISSA (2024). Methods for Estimating User Position in the Near-Field Regime. Dissertação de Mestrado, Publicação PPGEE.811/2024, Departamento de Engenharia Elétrica, Universidade de Brasília, Brasília, DF, xxxxp.

## CESSÃO DE DIREITOS

AUTOR: Larissa Rocha

TÍTULO: Methods for Estimating User Position in the Near-Field Regime.

GRAU: Mestre ANO: 2024

É concedida à Universidade de Brasília permissão para reproduzir cópias desta Dissertação de Mestrado e para emprestar ou vender tais cópias somente para propósitos acadêmicos e científicos. O autor reserva outros direitos de publicação e nenhuma parte desta dissertação de mestrado pode ser reproduzida sem autorização por escrito do autor.

---

Larissa Rocha

Universidade de Brasília (UnB)

Campus Darcy Ribeiro

Faculdade de Tecnologia - FT

Departamento de Engenharia Elétrica(ENE)

Brasília - DF CEP 70919-970

## ACKNOWLEDGEMENTS

First and foremost, I would like to express my deepest gratitude to God, whose blessings have been a constant source of strength and guidance throughout my journey in pursuing this Master's degree.

I would also like to express my deepest gratitude to my supervisor, Professor Daniel Costa Araujo, for his patience, encouragement, and guidance during my master's dissertation study at the Universidade de Brasília. He is not only a diligent researcher but also an excellent advisor and teacher. He taught me how to develop the research of my topic, how to write papers, and how to give presentations. Without his suggestions and help, much of the work in the dissertation would not have been possible. It is a precious fortune for me to be advised by him.

I would like to thank the University of Brasilia for giving me the precious opportunity to work on such an interesting topic, and also CAPES and FAPDF for all the financial support for this research.

Finally, I extend my heartfelt gratitude to my friends, my boyfriend Kaio, and my family, particularly my mother Cinthia Gomes Araujo and my father Marcelo Daniel Ferreira Gomes, for their unwavering love, support, and encouragement throughout my journey, without which pursuit of my master's degree would not have gone so smoothly.

# ABSTRACT

## METHODS FOR ESTIMATING USER POSITION IN THE NEAR-FIELD REGIME

Parameter estimation using signal processing methods is a significant topic in various domains such as radar, seismic analysis, sonar, electronic surveillance, and more. This research has focused on two key areas within signal processing: antenna array processing and user position estimation.

In the context of antenna array processing, the user's localization involves estimating the position parameters of sources, often employing subspace methods such as Multiple Signal Classification (MUSIC) and estimation of Signal Parameters via Rotational Invariance Techniques (ESPRIT), among others. In far-field scenarios, a source is characterized solely by its direction of arrival (DOA). However, this assumption no longer holds in near-field situations where sources are close to the sensor array. In such scenarios, the wavefront of the signal becomes spherical, necessitating the consideration of two parameters for accurate source localization: the direction of arrival and the distance between the source and the sensor array.

The near-field user position estimation is crucial due to several factors, especially when considering advancing networks like sixth-generation (6G), where further improvements are expected in localization and tracking. These improvements will result from the joint use of high frequencies and large arrays. With the significant increase of the antenna number and carrier frequency in future 6G systems, the near-field region of extremely large antenna arrays (ELAAs) will expand by orders of magnitude. As a result, near-field communications will play a critical role in future 6G mobile networks, where the propagation model must account for differences from existing far-field fifth-generation (5G) systems. The spatial density and the capacity of electromagnetic interactions between neighboring elements in ELAAs introduce unique considerations for near-field position estimation. Understanding and addressing these complexities will be the primary focus of this research.

This dissertation delves into two interconnected aspects of source localization: two-dimensional

(2D) source localization in the near-field and three-dimensional (3D) source localization in the near-field.

In our 2D source localization approach, specifically for coordinates  $[x,y]$ , we propose an innovative method that combines the adaptive subspace estimation with the sub-array architecture to accurately locate users in near-field scenarios. By including the sub-array techniques tailored for ELAAs, we explore the rotational invariance in each sub-array to implement the PAST (Projection Approximation Subspace Tracking) algorithm. This approach is computationally efficient due to its recursive update formula, which negates the necessity for computationally intensive tasks like matrix inversions or eigenvalue decompositions. In terms of precision, our method surpasses existing approaches, as demonstrated in graphs of root-mean-square error (RMSE) and graphs of cumulative distributed function (CDF) evaluations. Furthermore, the accuracy of the PAST algorithm at a distance of 3.5 meters is 0.0250 meters at the 10<sup>th</sup> percentile, outperforming other source localization methods. Similarly, at 25 meters, PAST achieves an accuracy of 0.3983 (10<sup>th</sup> percentile). These results highlight PAST's accuracy and reliability for precise source localization in near-field scenarios, making it a robust choice for such applications.

For 3D source localization, specifically for coordinates  $[x,y,z]$ , we introduce a novel three-dimensional position (3D-P) estimation method designed for wireless systems employing Uniform Rectangular Arrays (URAs). This approach virtually partitions the array into subarrays, each is tasked with independently estimating azimuth and elevation angles. To handle the multi-dimensional data effectively, we employ Higher-Order Singular Value Decomposition (HOSVD), reducing tensor size for a more concise representation of data structure, particularly beneficial in URA applications. Additionally, we utilize Taylor series approximation to address non-linear least square problems, contributing to accurate position estimations, even in intricate scenarios with 8 scatters. Our approach showcases the algorithm's efficacy in mitigating multipath interference, with noise power exerting minimal influence. The results indicate that sub-meter accuracy is attainable at 30 and 40 dB SNRs for the 2 and 8 scatters in all percentiles, emphasizing the robustness of the technique in favorable conditions.

**Keywords:** Near-Field, DOA, User's Location, Sub-array, ELAA, 3D Positioning, URA,

HOSVD.

# RESUMO

## MÉTODOS DE ESTIMAÇÃO DA POSIÇÃO DO USUÁRIO NO REGIME DE CAMPO PRÓXIMO

A estimativa de parâmetros usando métodos de processamento de sinais é um tópico importante em várias áreas como radar, análise sísmica, sonar, vigilância eletrônica, entre outros. Esta pesquisa se concentra em duas áreas-chave dentro do processamento de sinais: processamento de arranjo de antenas e estimativa da posição de usuários.

No contexto do processamento de arranjos de antenas, a localização do usuário envolve a estimativa dos parâmetros de posição das fontes, muitas vezes empregando métodos subespaaciais como Classificação Múltipla de Sinais (MUSIC), Estimativa de Parâmetros de Sinais via Técnicas de Invariância Rotacional (ESPRIT), entre outros. Em cenários de campo distante, uma fonte é caracterizada apenas pela sua direção de chegada (DOA). No entanto, essa suposição não é mais válida quando considera-se o campo próximo, onde as fontes estão próximas do conjunto de sensores. Nesses cenários, a frente de onda do sinal torna-se esférica, necessitando da consideração de dois parâmetros para a localização precisa da fonte: a direção de chegada e a distância entre a fonte e o conjunto de sensores.

A estimativa da posição do usuário em campo próximo é crucial devido a vários fatores, especialmente quando consideramos as redes avançadas, como a sexta geração (6G), onde é esperado melhorias na localização e rastreamento. Essas melhorias serão resultados do uso de altas frequências e grandes conjuntos de antenas. Com esse aumento significativo do número de antenas e da frequência portadora em futuros sistemas 6G, a região de campo próximo dos arranjos de antenas extremamente grandes (ELAAs) se expandirá em ordens de magnitude. Como resultado, as comunicações de campo próximo desempenharão um importante papel nas futuras redes móveis 6G, onde o novo modelo de propagação deve levar em consideração as diferenças dos sistemas existentes da quinta geração (5G) de campo distante. A densidade espacial e a capacidade de interações eletromagnéticas entre os elementos vizinhos nos ELAAs

introduzem considerações únicas para a estimativa da posição no campo próximo. Compreender e abordar essas complexidades será o foco principal desta pesquisa.

Esta dissertação explora dois aspectos relacionados da localização de fontes: localização de fontes bidimensional (2D) em campo próximo e localização de fontes tridimensional (3D) em campo próximo.

Em nossa abordagem de localização de fonte 2D, especificamente para coordenadas  $[x,y]$ , propomos um método que combina a estimativa adaptativa de subespaço com a arquitetura de submatriz para localizar com precisão os usuários no campo próximos. Ao abranger as técnicas de sub-arranjos adaptados para ELAAs, exploramos a invariância rotacional de cada sub-arranjo para introduzir o algoritmo de aproximação de projeção de rastreamento subespacial (PAST). Esta abordagem é computacionalmente eficiente devido à sua fórmula de atualização recursiva, que nega a necessidade de tarefas computacionalmente intensivas, como inversões de matrizes ou decomposições de autovalores. Em termos de precisão, nosso método supera as abordagens existentes, conforme demonstrado nos gráficos da raiz do erro quadrático médio (RMSE) e nos gráficos da função de distribuição acumulada (CDF). Além disso, a precisão do algoritmo PAST a uma distância de 3,5 metros é de 0,0250 metros no percentil 10, superando outros métodos de localização de fonte. Da mesma forma, a 25 metros, o PAST atinge uma precisão de 0,3983 no 10<sup>th</sup> percentil). Esses resultados destacam a precisão e a confiabilidade do PAST para localização precisa da fonte em cenários de campo próximo, tornando-o uma escolha robusta para tais aplicações.

Para localização de fonte 3D, especificamente para coordenadas  $[x,y,z]$ , introduzimos um novo método de estimativa de posição tridimensional (3D-P) projetado para sistemas sem fio empregando Arranjos Retangulares Uniformes (URAs). Esta abordagem particiona virtualmente o arranjo em subarranjos, cada uma com a tarefa de estimar independentemente o ângulo de azimute e o ângulo de elevação. Para lidar com os dados multidimensionais de forma eficaz, empregamos a decomposição de valores singulares de ordem superior (HOSVD), reduzindo o tamanho do tensor para uma representação mais concisa da estrutura de dados, particularmente benéfica em aplicações URA. Além disso, utilizamos a aproximação da série de Taylor para resolver problemas não lineares de mínimos quadrados, contribuindo para estimativas de posição precisas, mesmo em cenários complexos com 8 dispersões. Nossa abordagem mostra a eficácia do algoritmo na mitigação da interferência de multipercurso, com a potência do ruído

exercendo influência mínima. Os resultados indicam uma precisão submétrica alcançável em SNRs em SNRs de 30 e 40 dB para os dispersões 2 e 8 em todos os percentis, enfatizando a robustez da técnica em condições favoráveis.

**Palavras-chave:** Campo-Próximo, DOA, Localização de Usuário, Sub-Arranjo, ELAA, Posicionamento 3D, URA, HOSVD

# TABLE OF CONTENTS

<b>Table of contents</b>	i
<b>List of figures</b>	iv
<b>List of tables</b>	vii
<b>List of symbols</b>	viii
<b>Glossary</b>	ix
<b>Chapter 1 – Introduction</b>	1
1.1 Background and Motivation . . . . .	1
1.1.1 Background . . . . .	1
1.1.2 Problem Statement and Motivation . . . . .	2
1.2 Comprehensive Review of Near-Field Source Localization Techniques . . . . .	3
1.3 Main Contributions . . . . .	5
1.4 Thesis Organization and Structure . . . . .	5
<b>Chapter 2 – Antenna Characterization and Measurements</b>	7
2.1 Antenna Parameters and Figures of Merit . . . . .	8
2.1.1 Antenna Radiation . . . . .	8
2.1.2 Field Regions . . . . .	9
2.1.2.1 Radiation Equations for Near-Field and Far-Field . . . . .	11
2.1.3 Radiation Power Density . . . . .	14
2.1.4 Radiation intensity . . . . .	14
2.1.5 Beamwidth . . . . .	14
2.1.6 Directivity . . . . .	16
2.1.7 Gain . . . . .	16
2.2 Type of Antenna . . . . .	17
2.3 Antenna Array . . . . .	18
2.3.1 Basic of Array Signal Processing . . . . .	18

2.3.2	Conventional Configurations of Sensor Arrays . . . . .	22
2.3.2.1	Uniform Linear Array . . . . .	22
2.3.2.2	Uniform Planar Array . . . . .	23
<b>Chapter 3</b>	<b>– Source Localization</b>	<b>27</b>
3.1	Measurement Models and Principles for Source Localization . . . . .	28
3.1.1	TOA . . . . .	28
3.1.2	TDOA . . . . .	31
3.1.3	TSOA . . . . .	33
3.1.4	RSS . . . . .	35
3.1.5	DOA . . . . .	37
3.2	DOA estimation . . . . .	39
<b>Chapter 4</b>	<b>– DOA Estimation Algorithm</b>	<b>41</b>
4.1	Covariance Matrices . . . . .	41
4.2	Beamformer Scan . . . . .	43
4.3	Capon’s Beamformer . . . . .	45
4.3.1	Concept of Subspaces . . . . .	47
4.3.1.1	SVD . . . . .	48
4.4	Multiple Signal Classification . . . . .	48
4.5	Estimation of signal parameter via rotational invariance . . . . .	51
4.5.1	Signal Subspace Estimation . . . . .	53
4.5.1.1	Eigenvalues and Eigenvectors of Covariance Matrice . . . . .	55
4.5.1.2	Angle Estimation . . . . .	56
<b>Chapter 5</b>	<b>– Fundamentals of Near-Field Localization</b>	<b>59</b>
5.1	Far-Field Communications vs. Near-Field Communications . . . . .	59
5.1.1	Spherical Wavefront Delay-and-Sum . . . . .	60
5.2	Symmetric Subarray Partitioning . . . . .	63
5.2.1	Signal Model for Symmetric Subarrays . . . . .	65
5.2.1.1	Eigen-Decomposition of the Array Output . . . . .	66
<b>Chapter 6</b>	<b>– 2D Source Location in Near-Field</b>	<b>68</b>
6.1	Signal Model . . . . .	68
6.2	Near-Field User Position Estimation . . . . .	70
6.2.1	DOA Estimation . . . . .	71
6.2.1.1	PAST Estimation . . . . .	71

---

6.2.2	Range Estimation . . . . .	74
6.3	Simulation and Numerical Results . . . . .	76
6.4	Conclusion . . . . .	78
<b>Chapter 7 – 3D User Location Estimation</b>		<b>80</b>
7.1	Signal Model . . . . .	80
7.2	Tensor . . . . .	81
7.2.1	Tucker Decompositions . . . . .	82
7.3	Subspace Separation . . . . .	83
7.3.1	HOSVD . . . . .	84
7.3.2	Azimuth and Elevation Estimation . . . . .	85
7.3.3	User Position Estimation . . . . .	86
7.3.4	Computational Complexity Analysis . . . . .	88
7.4	Simulation and Numerical Results . . . . .	89
7.5	Conclusion . . . . .	93
<b>Chapter 8 – Conclusion</b>		<b>95</b>
8.1	Final Considerations . . . . .	95
8.2	Future Directions . . . . .	96
<b>References</b>		<b>98</b>

## LIST OF FIGURES

2.1	Coordinate system for antenna analysis (BALANIS, 2016). . . . .	9
2.2	Field regions of an antenna (BALANIS, 2016). . . . .	10
2.3	Typical changes of antenna amplitude pattern shape from reactive near-field toward the far-field (BALANIS, 2016). . . . .	11
2.4	Linear plot of power pattern and its associated lobes and beamwidths (BALANIS, 2016). . . . .	15
2.5	Signal receiving model. Adapted from (YANG, 2020) and (TREES, 2002). . . .	19
2.6	Signal receiving model. Adapted from (YANG, 2020) and (TREES, 2002). . . .	22
2.7	Signal receiving model. Adapted from (YANG, 2020) and (TREES, 2002). . . .	24
4.1	DOA estimation with the conventional beamformer; the signal impinges at $10^\circ$ and $30^\circ$ . . . . .	44
4.2	DOA estimation with Capon's beamformer; the signal impinges at $10^\circ$ and $30^\circ$ . .	46
4.3	DOA estimation with MUSIC; the radio signals impinges at $10^\circ$ and $30^\circ$ . . . . .	51
4.4	Antenna array structure for ESPRIT-based algorithms. (CHEN <i>et al.</i> , 2010). . .	52
4.5	DOA estimation by ESPRIT method; the radio signals impinges at $10^\circ$ and $30^\circ$ . .	58
5.1	Difference in element delays and wavefront shape between a steered beam without focusing, simulated by a 17-element ULA at an operational frequency of 3GHz. .	60
5.2	Difference in element delays and wavefront shape between a steered beam without focusing, simulated by a 17-element ULA at an operational frequency of 3GHz. .	61
5.3	Antenna array structure for ESPRIT-based algorithms. Adapted by (BJÖRN-SON <i>et al.</i> , 2021). . . . .	62

5.4	Comparison of Far-Field Planar Wavefronts and Near-Field Spherical Wavefronts: FFC beamsteering resembles a 'flashlight' emitting light with a plane wavefront, while NFC beamfocusing is akin to a 'spotlight' emitting light with a spherical wavefront. The corresponding radiation patterns, simulated for a narrowband system with 512 antennas operating at 3 GHz, are depicted on the right . . . . .	63
5.5	Near-field ULA configuration with symmetric partition. Adapted from (ZHI; CHIA, 2007) . . . . .	65
6.1	In a near-field scenario with a transmitting source and a receiver array, the phase across antenna elements changes nonlinearly, while in a spatial wide-band setting, the delay across elements varies significantly (ZHI; CHIA, 2007). . . . .	69
6.2	RMSE curve of the method proposed in this paper PAST, an enhanced variant PAST and SVD, 2D-IFFT (ZHI; CHIA, 2007) and ESPRIT (WYMEERSCH, 2020) with respect the user distance. . . . .	76
6.3	Comparison of empirical CDFs between estimators, $\ x\  = 3,5$ m. . . . .	77
6.4	Comparison of empirical CDFs between estimators, $\ x\  = 25$ m. . . . .	78
7.1	A three-way array (third-order tensor) $\mathcal{Y} \in \mathbb{R}^{7 \times 5 \times 8}$ with elements $y_{itq}$ (CICHOCKI <i>et al.</i> , 2009) . . . . .	81
7.2	Tucker3 model is a weighted sum of the outer product of three vectors (factors) stored as columns of component matrices $\mathbf{A} \in \mathbb{R}^{I \times J}$ . $\mathbf{B} = \mathbf{X}^T \in \mathbb{R}^{T \times R}$ and $\mathbf{C} \in \mathbb{R}^{Q \times P}$ . The core tensor $\mathcal{G} \in \mathbb{R}^{J \times R \times P}$ defines a linking structure between the set of components and $J, R$ , and $P$ denote the number of components. In order to achieve uniqueness for the Tucker models it is necessary to impose additional constraints such as sparsity and nonnegativity (CICHOCKI <i>et al.</i> , 2009) . . . . .	82
7.3	Visual representation of a 32x32 planar antenna array with 4x4 subarrays. . . . .	90
7.4	CDF of the UE location error for SNR = -20 dB. . . . .	91
7.5	CDF of the UE Location Error for SNR = -10 dB. . . . .	91
7.6	CDF of the UE Location Error for SNR = 0 dB. . . . .	92

---

7.7	The curves represent different power levels (5 dBm, 10 dBm) and scatter scenarios (2, 4). . . . .	93
-----	---	----

## LIST OF TABLES

2.1	Types of Antennas . . . . .	17
3.1	Comparison of Location Estimation Techniques . . . . .	38
6.1	Summary of Percentiles for Cumulative Distribution Function ( $\ x\  = \{3.5, 25\}$ m) . . . . .	77
7.1	Comparison of 10 <sup>th</sup> , 50 <sup>th</sup> , and 90 <sup>th</sup> percentiles across scenarios with varied SNRs for LOS only, 2, 4 and 8 scatters. . . . .	92

## LIST OF SYMBOLS

$\beta$	Wave number
$\lambda$	Wavelength
$c$	Velocity of light
$f$	Frequency
$\omega$	Temporal frequency
$R$	Distance or radius from the source of the electromagnetic wave
$D$	Largest dimension of the antenna
$\tau$	Time delay
$\sigma^2$	Power of the noise
$\mathbf{x}$	Vector notation (lowercase and bold)
$\mathbf{X}$	Matrix notation (uppercase and bold)
$\mathcal{X}$	Tensor notation (uppercase and calligraphic)
$\otimes$	Kronecker product
$\circ$	Hadamard (element-wise) product between vectors or matrices
$\sim$	Distributed as
$\perp$	Perpendicularity or orthogonality
$\Gamma$	Number of modes and the order of the tensor
$\mathcal{N}(\mathbf{a}, \mathbf{C})$	Gaussian distribution with mean $\mathbf{a}$ and covariance $\mathbf{C}$
$\mathbb{E}\{\cdot\}$	Expectation operator
$\text{tri}\{\cdot\}$	Triangular matrix operator
$\text{Diag}(\cdot)$	Transform a diagonal of a matrix into a square matrix
$\text{diag}(\cdot)$	Converts a vector into a square matrix
$(\cdot)^+$	Pseudo-inverse
$(\cdot)^*$	Complex conjugate of $(\cdot)$
$(\cdot)^T$	Transpose of $(\cdot)$

## GLOSSARY

<b>1D</b>	One-Dimensional
<b>2D</b>	Two-Dimensional
<b>3D</b>	Three-Dimensional
<b>5G</b>	Fifth-Generation
<b>6G</b>	Sixth-Generation
<b>BS</b>	Base Station
<b>CBF</b>	Classical Beamforming
<b>CF</b>	Cell-Free
<b>CNN</b>	Convolutional Neural Network
<b>COA</b>	Curvature of Arrival
<b>CRLB</b>	Cramér-Rao Lower Bound
<b>DFT</b>	Discrete Fourier Transform
<b>DL</b>	Deep Learning
<b>DNN</b>	Deep Neural Network
<b>DOA</b>	Direction of Arrival
<b>dB</b>	Decibels
<b>EVD</b>	Eigenvector Decomposition
<b>ELAA</b>	Extremely Large Antenna Arrays

**ESPRIT** Estimation of Signal Parameters via Rotational Invariance Techniques

**FIM** Fisher Information Matrix

**GPS** Global Positioning Systems

**HOSVD** Higher Order Singular Value Decomposition

**IFFT** Inverse Fast Fourier Transform

**IoT** Internet of Things

**KPI** Key Performance Indicators

**LOB** Line of Bearing

**LOS** Line-of-Sight

**LS** Least-Squares

**MIMO** Multiple-Input-Multiple-Output

**ML** Maximum Likelihood

**mmWave** Millimeter-Wave

**MUSIC** Multiple Signal Classification

**MVDR** Minimum Variance Distortionless Response

**OFDM** Frequency Division Multiplexing

**OMP** Orthogonal Matching Pursuit

**PEB** Position Error Bound

**PAST** Projection Approximation Subspace Tracking

**PDF** Probability Density Function

**RIS** Reconfigurable Intelligent Surfaces

**RLS** Recursive Least-Squares

- 
- RSS** Received Signal Strength
- SVD** Singular Value Decomposition
- Tbps** Terabits per Second
- TDOA** Time Difference of Arrival
- THz** Terahertz
- TLS** Total Least Square
- TOA** Time of Arrival
- TSOA** Time of Stationary Arrival
- UE** User Equipment
- ULA** Uniform Linear Arrays
- UM** Ultra-Massive
- URA** Uniform Rectangular Arrays

# INTRODUCTION

This chapter will introduce the background and motivation behind researching near-field source localization. Furthermore, we will review the developments achieved in this area over the past decades. Lastly, we will summarize our main contributions and outline the organization of the dissertation. This work will include a comprehensive literature review on near-field source localization techniques, highlighting advancements, challenges, and potential future directions.

## 1.1 BACKGROUND AND MOTIVATION

### 1.1.1 Background

The advent of Sixth-Generation (6G) mobile networks announced a transformative era for emerging applications such as holographic video and digital replication. To realize these advancements, significant research endeavors are underway to innovate new wireless technologies that surpass the Key Performance Indicators (KPI)s of Fifth-Generation (5G). These technologies are positioned to significantly enhance spectral efficiency, capacity, and coverage in 6G networks (CUI *et al.*, 2022).

Ultra-Massive (UM) Multiple-Input-Multiple-Output (MIMO) and Cell-Free (CF) massive MIMO are anticipated to achieve a tenfold increase in spectral efficiency through vast spatial multiplexing and beamforming gains. Additionally, the introduction of Reconfigurable Intelligent Surfaces (RIS) promises further enhancements in capacity and coverage by dynamically manipulating the wireless environment using thousands of antennas. Moreover, Millimeter-Wave (mmWave) and Terahertz (THz) UM-MIMO are expected to provide substantial spectral resources supporting up to a 100-fold improvement in peak data rates, reaching Terabits per Second (Tbps) (LIU *et al.*, 2023).

Despite addressing diverse application scenarios with varied KPIs, these technologies share a common requirement: the utilization of Extremely Large Antenna Arrays (ELAA). Unlike the massive MIMO technology in 5G, ELAA for 6G necessitates not only a significant increase in the number of antennas but also leads to fundamental changes in electromagnetic characteristics (CUI *et al.*, 2022).

The electromagnetic radiation field is typically categorized into the far-field and radiation near-field regions, with the boundary delineated by the Rayleigh distance, also known as the Fraunhofer distance. The Rayleigh distance is proportional to the square of the array aperture and carrier frequency. While existing 5G communications predominantly operate within the far-field region due to a limited number of antennas, the substantial increase in antennas and carrier frequency in 6G will expand the near-field region of ELAA significantly (LIU *et al.*, 2023), (CUI; DAI, 2021).

Consequently, near-field communications will play a fundamental role in future 6G mobile networks, necessitating the consideration of spherical wave propagation models, distinct from the planar wave models used in 5G's far-field communications. However, the transition to near-field propagation poses new challenges for ELAA systems that must be identified and addressed to harness the full potential of 6G communications (CUI *et al.*, 2022).

### 1.1.2 Problem Statement and Motivation

Many source localization algorithms have been designed to estimate the Direction of Arrival (DOA) of signal sources, operating under the assumption that these sources are situated in the far-field. In the far-field scenario, the distance of a source extends well beyond the Fresnel region, and the signal wavefront is typically approximated as a plane wave upon reaching the sensor array. Here, each source is characterized solely by its DOA (LIU *et al.*, 2023).

However, in numerous real-world scenarios, sources may fall within the Fresnel region. In such cases, the assumption of a plane wave does not hold, and the signal wavefronts become spherical. Consequently, both the DOAs and ranges of sources become crucial for accurate localization, leading to a more complex localization problem (LIU *et al.*, 2023).

The computational complexity of near-field estimators is notably higher compared to far-

field estimators, posing a challenge for devices with limited computational power, such as portable devices. While advanced devices can handle this complexity for achieving high accuracy, energy efficiency and real-time processing remain critical concerns, this is especially true for long-time field applications, where the electronic energy can not be always guaranteed (KORSO *et al.*, 2013).

The developing source localization algorithms in the near-field of antenna systems, particularly for ELAA, encompasses several fundamental factors. Firstly, within the realm of ELAA, which encompasses both Two-Dimensional (2D) and Three-Dimensional (3D) array configurations such as Uniform Linear Arrays (ULA) and Uniform Rectangular Arrays (URA), precise source localization plays a critical role in optimizing the utilization of these massive antenna arrays. Accurate estimations of DOA and range in the near-field are important in enhancing spectral efficiency, minimizing interference, and overall system performance enhancement. Moreover, with the increasing reliance on ELAA technology in 6G and future wireless communication systems, advancements in near-field source localization algorithms are indispensable for unlocking the full potential of these next-generation networks. These advancements pave the way for high data rates, low-latency communications, and seamless connectivity across diverse deployment scenarios (CUI; DAI, 2021).

## 1.2 COMPREHENSIVE REVIEW OF NEAR-FIELD SOURCE LOCALIZATION TECHNIQUES

In recent years, numerous methods have emerged specifically tailored for near-field source localization. Noteworthy among these are the Maximum Likelihood (ML) method (CEKLI; CIRPAN, 2001), (CHEN *et al.*, 2002), Multiple Signal Classification (MUSIC) (ZHOU *et al.*, 2020), (LAVATE *et al.*, 2010), the 2D MUSIC method (HUANG; BARKAT, 1991), and Estimation of Signal Parameters via Rotational Invariance Techniques (ESPRIT) (LAVATE *et al.*, 2010). Traditional MUSIC-based approaches faced significant computational complexities due to the use of Eigenvector Decomposition (EVD) for segregating received signals into signal and noise spaces (HUANG *et al.*, 2021). The work (HUANG *et al.*, 2021) introduces a low-complexity localization algorithm, employing Discrete Fourier Transform (DFT) for DOA estimation and Orthogonal Matching Pursuit (OMP) for range estimation. Despite this advancement, chal-

lenges such as frequency bias in DFT leading to DOA and range estimation errors persist. Other techniques include the following method (STARER; NEHORAI, 1994), polynomial rooting method (WEISS; FRIEDLANDER, 1993), weighted linear prediction method (GROSICKI *et al.*, 2005), and higher-order ESPRIT method (YUEN; FRIEDLANDER, 1998), (CHALLA; SHAMSUNDER, 1995). Moreover, the innovative approach presented in (CHEN *et al.*, 2020) leverages compressive sensing and array interpolation to achieve high-resolution localization in complex near-field environments. However, many existing algorithms either necessitate multidimensional search, encounter pairing problems or suffer from poor resolution due to heavy aperture loss.

The advent of Deep Learning (DL) has also influenced source localization research, with studies like (LIU *et al.*, 2020), (CHAKRABARTY; HABETS, 2019), (LEE *et al.*, 2021), (LIU *et al.*, 2019), and (KAMILARIS; PRENAFETA-BOLDÚ, 2018) exploring DL-based techniques. These methods employ Deep Neural Network (DNN) or Convolutional Neural Network (CNN) with preprocessed data, categorized into grid-free and grid-based approaches. While grid-free methods lack resolution constraints but may risk errors, grid-based methods offer resolution at the expense of computational resources and training data (LEE *et al.*, 2021), (LIU *et al.*, 2019), (KAMILARIS; PRENAFETA-BOLDÚ, 2018).

Recent approaches like those described in (WYMEERSCH, 2020) and (ZHI; CHIA, 2007) propose transforming the 2D search involved in the parameter estimation to a One-Dimensional (1D) search strategy based on second-order statistics with symmetric-sub-array partitioning, avoiding high-order statistics computation and multidimensional search. However, these methods may incur low precision due to utilizing MUSIC and 2D- Inverse Fast Fourier Transform (IFFT) with Fisher Information Matrix (FIM) analysis for the user's estimation.

In the domain of 3D source localization, recent research has started to address the constraints of near-field positioning using 5G antenna arrays, as seen in preliminary studies cited in references (ELZANATY *et al.*, 2020), (GUSTAFSSON, 2010). However, these investigations primarily focus on static scenarios and utilize non-Bayesian methodologies. For instance, (GUERRA *et al.*, 2021) evaluates practical algorithms leveraging Curvature of Arrival (COA) but acknowledges its limitations tied to sensor geometry and placement accuracy, impacting adaptability across scenarios and environments.

Expanding on this context, papers referenced in (KORSO *et al.*, 2013), (ELZANATY *et al.*, 2020), (GUSTAFSSON, 2010) delve into derivations relevant to near-field sources, particularly in scenarios featuring transmitter-receiver synchronization. Notably, (KORSO *et al.*, 2013), (OZTURK *et al.*, 2023), (GUSTAFSSON, 2010), (EMENONYE *et al.*, 2023) and (ABU-SHABAN *et al.*, 2021) introduce models tailored for scenarios involving metasurfaces, offering insights into RIS-assisted localization scenarios.

### 1.3 MAIN CONTRIBUTIONS

In this study, we propose a comprehensive approach to near-field source localization leveraging ELAA in both 2D and 3D configurations. For both configurations, we partition the large array in symmetric subarrays, these subarrays demonstrate rotational invariance properties akin to far-field scenarios within the signal subspace.

For 2D configuration, our localization solution introduces an adaptive algorithm that tracks subspace variations along the ELAA. We utilize the Projection Approximation Subspace Tracking (PAST) algorithm, known for its efficiency and robustness in subspace tracking, minimizing computational complexity while maintaining accuracy. This stands in contrast to batch methods like EVD of the sample covariance matrix or Singular Value Decomposition (SVD) of the data matrix, which demand repetitive estimation of the subspace or eigenvectors. Our solution consists of two steps: 1) applying PAST to symmetric subarrays for DOA estimation, and 2) using the estimated angle of arrival for each subarray, we apply the intersection of lines method for range estimation.

- *Publication:* Rocha, Larissa, and Daniel Costa Araújo. "Adaptive Subspace-Based User Localization in Near-Field Regime Using Sub-Array Architecture," *XLI Simpósio Brasileiro de Telecomunicações e Processamento de Sinais*, 2023.

### 1.4 THESIS ORGANIZATION AND STRUCTURE

This thesis is organized into several distinct chapters, each focusing on key aspects of antenna array systems and source localization techniques.

In Chapter 2, we first present a brief introduction of the antenna characterization and measurements. This chapter delves into the fundamental parameters of antenna arrays, highlighting various types of antennas and highlighting the significance of array arrangements such as ULA and URA. Additionally, it addresses antenna measurement techniques essential for system characterization and performance evaluation.

The third chapter explores measurement models and principles crucial for source localization, including Time of Arrival (TOA), Time Difference of Arrival (TDOA), Time of Stationary Arrival (TSOA), Received Signal Strength (RSS), and DOA. The chapter particularly focuses on DOA estimation methods, elucidating why they offer superior performance compared to other localization techniques.

Chapter 4 delves into various DOA estimation algorithms such as the Classical Beamforming Method Classical Beamforming (CBF), Capon’s Beamformer, MUSIC, and ESPRIT. Each algorithm’s principles, advantages, and limitations are discussed in detail.

The fifth chapter contrasts Far-Field Communications with Near-Field Communications, highlighting the challenges posed by spherical wavefronts and introducing techniques like Taylor approximation and Symmetric Subarray Partitioning to mitigate non-linearity issues associated with spherical wavefronts in near-field localization.

In Chapter 6, we present a detail of our novel approach for 2D user location estimation in near-field for ELAA, focusing on the adaptive algorithm employing PAST for efficient subspace tracking. The chapter also discusses computational complexities and the methodology’s effectiveness compared to other methods.

In Chapter 7, we present our 3D tensor localization method tailored for ELAA with URA. Subarrays independently estimate azimuth and elevation angles, facilitated by Higher Order Singular Value Decomposition (HOSVD) for compact data representation. Taylor series approximation aids in solving non-linear least square problems, ensuring precise position estimations.

The thesis concludes with a comprehensive synthesis of findings from each chapter, highlighting key contributions, limitations, and future research directions in the field of antenna array systems and source localization techniques.

# ANTENNA CHARACTERIZATION AND MEASUREMENTS

Antennas constitute indispensable elements within wireless communication systems, serving as the conduits for signal transmission transforming electrical signals in wired systems into electromagnetic waves that propagate through space. Conversely, they facilitate the reception process, converting incoming electromagnetic waves into signals or voltages at their terminals for subsequent processing by the receiver. Maxwell's equations fully characterize the transmitting and receiving functionalities within the antenna structures, providing a comprehensive framework for understanding and optimizing antenna behavior in various communication scenarios. The foundation laid by these equations underscores the pivotal role antennas play in the seamless exchange of information, making them essential components in modern wireless communications (EIBERT; VOLAKIS, 2007).

In this study, our focus leans toward practical applications. For those seeking a deeper understanding of electromagnetism, the author recommends referring to the book (KRAUS, 1988). While electromagnetism is indeed described using mathematical foundations governing antenna radiation and ensures precision to avoid errors, our approach will not delve deeply into complex equations or mathematical proofs.

One of the most basic questions that may be asked concerning antennas is "How do they radiate?" A qualitative understanding of the radiation mechanism may be obtained by considering that antennas emit radiation through currents. Design involves managing currents to create a desired radiation pattern (BALANIS, 1992). The challenge often lies in preventing unintended radiation, especially in circuits. An antenna transforms bound circuit fields into propagating electromagnetic waves and, by reciprocity, collects power from passing electromagnetic waves. According to Maxwell's equations, any time-varying electric or magnetic field produces the opposite field and forms an electromagnetic wave. The wave has its two fields

oriented orthogonally, and it propagates in the direction normal to the plane defined by the perpendicular electric and magnetic fields. The electric field, the magnetic field, and the direction of propagation form a right-handed coordinate system. The propagating wave field intensity decreases by  $1/R$  away from the source, whereas a static field drops off by  $1/R^2$ . Any circuit with time-varying fields has the capability of radiating to some extent (MILLIGAN, 2005).

We consider only time-harmonic fields and use phasor notation with time dependence  $e^{(j\omega t)}$ . An outward-propagating wave is given by  $e^{-j(\beta R - \omega t)}$ , where  $\beta$  is the wave number given by  $2\pi/\lambda$ .  $\lambda$  is the wavelength of the wave given by  $c/f$ , where  $c$  is the velocity of light ( $3 \times 10^8$  m/s in free space) and  $f$  is the frequency (MILLIGAN, 2005).

## 2.1 ANTENNA PARAMETERS AND FIGURES OF MERIT

Numerous parameters and figures of merit contribute to defining the performance of an antenna system. The specific definitions of these metrics are available in references (BALANIS, 1992) and (IEEE..., 2014), with the terminologies used herein sourced from (IEEE..., 2014) indicated in quotation marks. In this document, we highlight a selection of the most crucial metrics in the following discussion.

### 2.1.1 Antenna Radiation

Antennas radiate spherical waves that propagate radially from the antenna's center in a designated coordinate system. As we move to significant distances, spherical waves can be effectively represented as plane waves, offering a simplified problem-solving approach. It is important to note that while plane waves are convenient for analysis, they are not physically realizable as they necessitate infinite power (MILLIGAN, 2005). The radiation property of most concern is the two- or three-dimensional spatial distribution of radiated energy as a function of the observer's position along a path or surface of constant radius. A convenient set of spherical coordinate systems is shown in Fig. 2.1. The amplitude field pattern is a trace of the received electric (magnetic) field at a constant radius. On the other hand, a graph of the spatial variation of the power density along a constant radius is called an amplitude power pattern. Often the

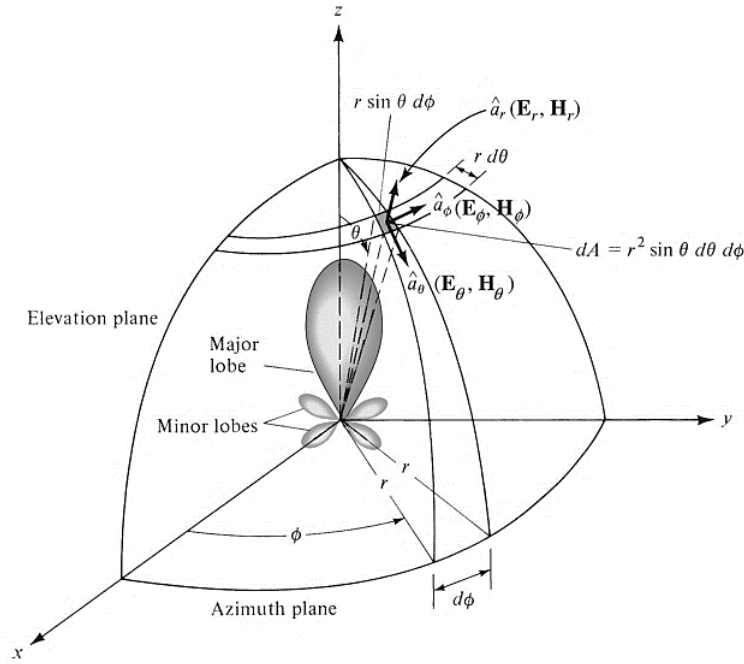


Figure 2.1: Coordinate system for antenna analysis (BALANIS, 2016).

field and power patterns are normalized concerning their maximum value, yielding normalized field and power patterns. Also, the power pattern is usually plotted on a logarithmic scale or more commonly in Decibels (dB) (BALANIS, 2016).

### 2.1.2 Field Regions

In this document, a fundamental aspect of antenna knowledge revolves around comprehending the distinct field regions associated with an antenna. The space surrounding an antenna is typically divided into three regions: (a) the reactive near-field, (b) the radiating near-field (Fresnel region), and (c) the far-field (Fraunhofer region), as depicted in Figure 2.2. These designations help characterize the field behavior within each region. While there are no sudden shifts in field configurations when crossing these boundaries, notable differences exist among them. Although the exact boundaries between these regions are not universally defined, various criteria have been established and are commonly employed to delineate these regions (BALANIS, 2016).

The *reactive near-field* is defined as that portion of the near-field region immediately surrounding the antenna wherein the reactive field predominates. For most antennas, the outer

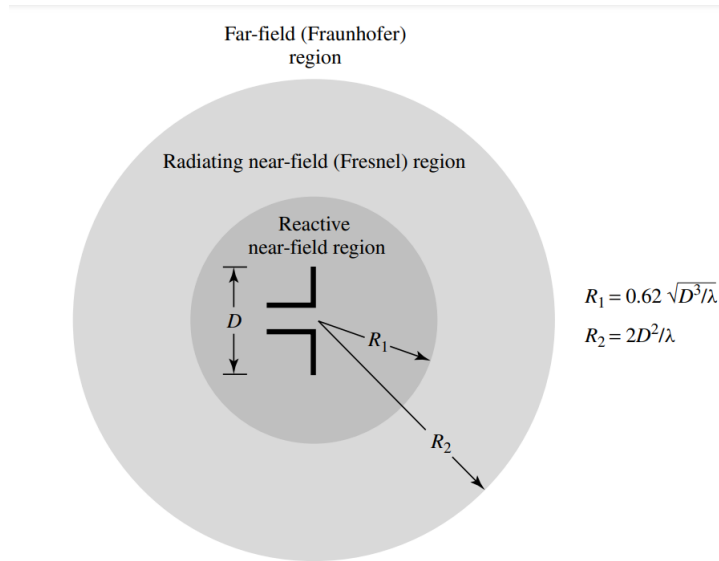


Figure 2.2: Field regions of an antenna (BALANIS, 2016).

boundary of this region is commonly taken to exist at a distance  $R < 0.62\sqrt{D^3/\lambda}$  from the antenna surface and  $D$  is the largest dimension of the antenna. For a very short dipole or equivalent radiator, the outer boundary is commonly taken to exist at a distance  $\lambda/2\pi$  from the antenna surface (BALANIS, 2016).

The *radiating near-field (Fresnel)* is the region of the field of an antenna between the reactive near-field region and the far-field region wherein radiation fields predominate and wherein the angular field distribution is dependent upon the distance from the antenna. The radial distance  $R$  over which this region exists is  $0.62\sqrt{D^3/\lambda} \leq R < 2D^2/\lambda$  (provided  $D$  is large compared to the wavelength).

The *far-field (Fraunhofer)* region is characterized as that portion of the antenna's field where the angular field distribution remains largely constant regardless of distance from the antenna. Here, the real part of the power density prevails. The radial distance  $R$  defining the extent of this region is  $R \geq 2D^2/\lambda$ .

The amplitude pattern of an antenna undergoes shape variations, both magnitude and phase, as the observation distance transitions from the reactive near-field to the far-field. Fig. 2.3 illustrates the typical evolution of the antenna shape, where  $D$  represents the largest dimension. In the reactive near-field region, the pattern is more spread out and nearly uniform, with slight variations. As the observation point shifts to the radiating near-field region (Fresnel), the pattern smoothness, forms lobes. In the far-field region (Fraunhofer), the pattern becomes

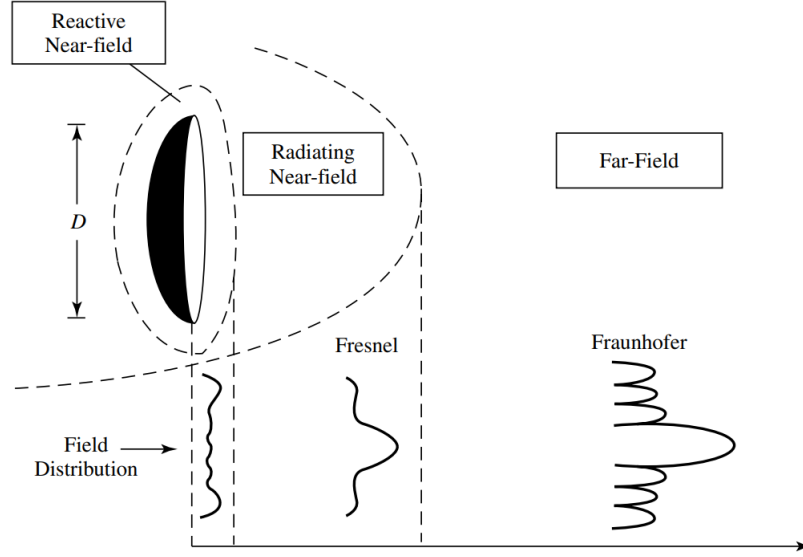


Figure 2.3: Typical changes of antenna amplitude pattern shape from reactive near-field toward the far-field (BALANIS, 2016).

well-defined, usually comprising a few minor lobes and one or more major lobes.

### 2.1.2.1 Radiation Equations for Near-Field and Far-Field

To describe the upcoming antenna parameters, it is essential first to understand the behavior of the electric and magnetic fields in the different regions, near and far fields. As mentioned previously, our approach will not delve into complex equations or mathematical proofs. For more detailed explanations and a deeper understanding, we encourage readers to consult the book (BALANIS, 2012), which serves as the primary reference for this section.

According to (BALANIS, 2012), In the near-field region, the vector potential  $\mathbf{A}$  due to a current density  $\mathbf{J}$  is given by:

$$\mathbf{A}(x, y, z) = \frac{\mu}{4\pi} \iiint_V \mathbf{J}(x', y', z') \frac{e^{-j\beta R}}{R} dv', \quad (2.1)$$

where  $\mu$  represents the magnetic permeability of the medium in which the electromagnetic fields are being calculated, and  $R = \sqrt{(x - x')^2 + (y - y')^2 + (z - z')^2}$  is the distance between the source point  $x', y', z'$  and the observation point  $x, y, z$ .

The magnetic field  $\mathbf{H}$  is derived from  $\mathbf{A}$  using:

$$\mathbf{H}_A = \frac{1}{\mu} \nabla \times \mathbf{A}. \quad (2.2)$$

Applying vector identities and interchanging integration and differentiation, we obtain:

$$\mathbf{H}_A(x, y, z) = -\frac{1}{4\pi} \iiint_V (\hat{\mathbf{R}} \times \mathbf{J}) \frac{1 + j\beta R}{R^2} e^{-j\beta R} dv', \quad (2.3)$$

where  $\hat{\mathbf{R}}$  is a unit vector directed along the line joining any point of the source and the observation point. This expression shows the intricate dependency on  $R$ , typical of near-field behavior.

Similarly, the electric field  $\mathbf{E}$  is calculated using:

$$\mathbf{E}_A = \frac{1}{j\omega\varepsilon} \nabla \times \mathbf{H}_A. \quad (2.4)$$

Resulting in components:

$$E_{Ax} = -\frac{j\eta}{4\pi\beta} \iiint_V \{C_1 J_x + (x - x')C_2 [(x - x')J_x + (y - y')J_y + (z - z')J_z]\} e^{-j\beta R} dv', \quad (2.5)$$

$$E_{Ay} = -\frac{j\eta}{4\pi\beta} \iiint_V \{C_1 J_y + (y - y')C_2 [(x - x')J_x + (y - y')J_y + (z - z')J_z]\} e^{-j\beta R} dv', \quad (2.6)$$

$$E_{Az} = -\frac{j\eta}{4\pi\beta} \iiint_V \{C_1 J_z + (z - z')C_2 [(x - x')J_x + (y - y')J_y + (z - z')J_z]\} e^{-j\beta R} dv', \quad (2.7)$$

where

$$C_1 = \frac{-1 - j\beta R + \beta^2 R^2}{R^3}, \quad (2.8)$$

$$C_2 = \frac{3 + j3\beta R - \beta^2 R^2}{R^5}. \quad (2.9)$$

On the other side, in the far-field approximation,  $R$  is simplified as  $R \approx r - \hat{\mathbf{r}} \cdot \mathbf{r}'$ , where  $r = |\mathbf{r}|$  is the distance from the origin to the observation point  $(x, y, z)$ ,  $\mathbf{r}'$  is the vector from the origin to the source point  $(x', y', z')$ ,  $\hat{\mathbf{r}} = \frac{\mathbf{r}}{r}$  is the unit vector in the direction of  $\mathbf{r}$ , and  $\hat{\mathbf{r}} \cdot \mathbf{r}'$  is the dot product of  $\hat{\mathbf{r}}$  and  $\mathbf{r}'$ , representing the projection of  $\mathbf{r}'$  onto  $\hat{\mathbf{r}}$ . This approximation simplifies the expression for  $\mathbf{A}$  (BALANIS, 2012):

$$\mathbf{A}(x, y, z) \approx \frac{\mu e^{-j\beta r}}{4\pi r} \iiint_V \mathbf{J}(x', y', z') e^{j\beta \hat{\mathbf{r}} \cdot \mathbf{r}'} dv', \quad (2.10)$$

where  $r$  is the distance from the source to the observation point.

The magnetic field  $\mathbf{H}$  in the far-field can be derived from  $\mathbf{A}$  using:

$$\mathbf{H}_A = \frac{1}{\mu} \nabla \times \mathbf{A}. \quad (2.11)$$

In the far-field, this simplifies to:

$$\mathbf{H}_A(x, y, z) \approx \frac{j\beta}{4\pi} \frac{e^{-j\beta r}}{r} \hat{\mathbf{r}} \times \iiint_V \mathbf{J}(x', y', z') e^{j\beta \hat{\mathbf{r}} \cdot \mathbf{r}'} dv'. \quad (2.12)$$

This expression indicates that the magnetic field in the far-field region predominantly depends on the current distribution and decays as  $1/r$ .

Similarly, the electric field  $\mathbf{E}$  is calculated using:

$$\mathbf{E}_A = \frac{1}{j\omega\epsilon} \nabla \times \mathbf{H}_A, \quad (2.13)$$

where  $\epsilon$  represents the electric permittivity of the medium. Applying the far-field approximation:

$$\mathbf{E}_A(x, y, z) \approx \eta \hat{\mathbf{r}} \times \mathbf{H}_A, \quad (2.14)$$

where  $\eta = \sqrt{\mu/\epsilon}$  is the intrinsic impedance of the medium.

To describe the antenna parameters comprehensively, understanding the behavior of electric and magnetic fields in both near-field and far-field regions is crucial. In the near-field, the fields exhibit complex dependencies on distance and current distribution. Both electric and magnetic fields decay slowly with distance, following intricate spatial variations. Conversely, in the far field, fields simplify to depend predominantly on  $1/r$ . Here, the electric and magnetic fields are orthogonal to each other and to the direction of propagation, and they decay significantly with distance from the source (EIBERT; VOLAKIS, 2007).

These field behaviors directly influence the calculation of antenna parameters such as Radiation Power Density, Gain, and Directivity. In the far-field region, these parameters can be more straightforwardly derived due to the simplified field expressions. Radiation Power Density is proportional to the square of the field intensity and inversely proportional to the square of the distance. Gain and Directivity calculations rely on the far-field radiation patterns, which are easier to characterize due to the uniformity and predictability of the fields. In the near-field region, however, these parameters require careful consideration of the complex field interactions and spatial variations, making the calculations more challenging and often necessitating numerical methods for accurate characterization (KRAUS, 1988).

### 2.1.3 Radiation Power Density

Electromagnetic waves are used to transport information through a wireless medium or a guiding structure, from one point to the other. It is then natural to assume that power and energy are associated with electromagnetic fields. In general, the power density is complex. In the reactive near-field, the imaginary component is dominant. In the far-field, the real part is dominant. The power density  $\mathbf{S}$  is expressed as (BALANIS, 2016):

$$\mathbf{S} = \frac{1}{2} \mathbf{E} \times \mathbf{H}^* = S_r + jS_i, \quad (2.15)$$

where  $(\cdot)^*$  indicates complex conjugate. The real part is usually referred to as radiation density.

### 2.1.4 Radiation intensity

The radiation intensity  $U$  quantifies the power emitted from an antenna per unit solid angle. Typically evaluated in the far-field, it represents the distribution of radiated power in different directions. Mathematically, it is linked to the real part of the power density by the relationship (VOLAKIS; VOLAKIS, 2007) (BALANIS, 2016):

$$U = r^2 S_r, \quad (2.16)$$

where  $r$  is the spherical radial distance.

### 2.1.5 Beamwidth

Beamwidth is the angular separation between two directions where the radiation intensity is identical, and there are no other intermediate points with the same value. When the intensity reaches half of the maximum, it is termed *Half-Power Beamwidth* (HPBW). A typical antenna pattern has a major lobe, side lobes, minor lobes, a back lobe, and several nulls, as illustrated in Fig. 2.4 (MILLIGAN, 2005).

A *major lobe* (also called the main beam) is defined as the radiation lobe containing the direction of maximum radiation. In Fig. 2.4 the major lobe is pointing in the  $\theta = 0$  direction.

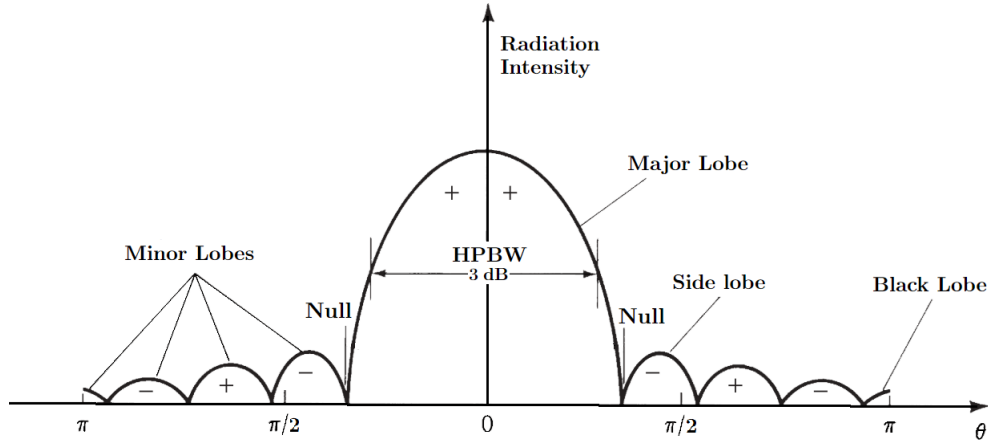


Figure 2.4: Linear plot of power pattern and its associated lobes and beamwidths (BALANIS, 2016).

In some antennas, such as split beam antennas, there may exist more than one major lobe (BALANIS, 1992).

A *minor lobe* is any lobe except a major lobe. In Fig. 2.4 all the lobes except the major can be classified as minor lobes.

A *side lobe* is a radiation lobe in any direction other than the intended lobe. (Usually, a side lobe is adjacent to the main lobe and occupies the hemisphere in the direction of the main beam).

A *back lobe* is a radiation lobe whose axis makes an angle of approximately  $180^\circ$  to the beam of an antenna. Usually, it refers to a minor lobe that occupies the hemisphere in a direction opposite to that of the major (main) lobe.

An isotropic radiator, a hypothetical and lossless antenna with uniform radiation intensity in all directions, serves as a convenient reference for expressing the directive properties of real antennas. Its radiation density  $S_{r0}$  and intensity  $U_0$  are defined as (BALANIS, 2016):

$$S_{r0} = \frac{P_r}{4\pi r_s^2}, \quad (2.17)$$

$$U_0 = \frac{P_r}{4\pi}, \quad (2.18)$$

where  $P_r$  represents the power radiated by the antenna.

### 2.1.6 Directivity

Directivity is one of the most important figures of merit that describes the performance of an antenna. It is defined as the ratio of the radiation intensity in a given direction from the antenna to the radiation intensity averaged over all directions. Using Eq. (2.18), it can be written as (VOLAKIS; VOLAKIS, 2007) (BALANIS, 2016):

$$D_r = \frac{U(\theta, \phi)}{U_0} = \frac{4\pi U(\theta, \phi)}{P_r}, \quad (2.19)$$

where  $U(\theta, \phi)$  is the radiation intensity in the direction  $\theta, \phi$ ,  $U_0$  is the radiation intensity of isotropic source and  $P_r$  is the radiated power. If the direction is not specified, it implies the direction of maximum radiation intensity (maximum directivity) expressed as:

$$D_{r0} = \frac{U_{max}(\theta, \phi)}{U_0} = \frac{4\pi U_{max}(\theta, \phi)}{P_r}. \quad (2.20)$$

The directivity is an indicator of the relative directional properties of the antenna.

### 2.1.7 Gain

Gain is defined as the ratio of the radiation intensity in a specific direction to the radiation intensity that would result from isotropic radiation of the power accepted by the antenna. This can be expressed using Eq. (2.18) as (VOLAKIS; VOLAKIS, 2007) (BALANIS, 2016):

$$G = \frac{U(\theta, \phi)}{U_a} = \frac{4\pi U(\theta, \phi)}{P_a}, \quad (2.21)$$

where  $P_a$  denotes the accepted (input) power to the antenna, it is crucial to note that when a specific direction is not specified, it implies the direction of maximum radiation, which corresponds to maximum gain. In simplest terms, the main difference between the definitions of directivity, as given by Eq. (2.19), and gain, as given by Eq. (2.21), is that directivity is based on the radiated power while the gain. Since all of the accepted (input) power is not radiated (because of losses), the two are related by:

$$P_r = e_r P_a, \quad (2.22)$$

where  $e_r$  is the radiation efficiency of the antenna as defined by the ratio of the total power radiated by an antenna to the net power accepted by an antenna from the connected transmitter. By using Eq. (2.22) and Eq. (2.19) the gain can be expressed as:

$$G = e_r \frac{4\pi U(\theta, \phi)}{P_r} = e_r D_r. \quad (2.23)$$

For a lossless antenna, its gain is equal to its directivity.

## 2.2 TYPE OF ANTENNA

In the preceding sections, we have discussed parameters that characterize the performance of antennas. Now, we delve into the main types of antennas, each designed with specific configurations tailored to diverse applications. Table 2.1 serves as a comprehensive guide, presenting an overview of these antenna types along with their distinctive configurations and applications.

In general, antenna arrays have higher efficiency in space, frequency, and time than ordinary antennas. Thus, an increasing number of ordinary antennas are replaced by antenna arrays in practice, and researchers have transferred their focus on antenna arrays from ordinary antennas. Consequently, in this work, we analyze the performance of antenna arrays, which are more widely used than ordinary antennas, in user position estimation (VOLAKIS; VOLAKIS, 2007).

Table 2.1: Types of Antennas

Type of Antenna	Examples	Applications
Wire Antennas	Dipole, Monopole, Helix, Loop	Personal, Buildings, Ships, Automobiles, Spacecrafts
Aperture Antennas	Waveguide, Horn	Flush-mounted, Aircraft, Spacecraft
Reflector Antennas	Parabolic, Corner	Microwave Communication, Satellite Tracking, Radio Astronomy
Lens Antennas	Convex-plane, Concave-plane, Convex-convex, Concave-concave	Very High-Frequency Applications
Microstrip Antennas	Circular, Rectangular Metallic Patch	Aircraft, Spacecraft, Satellites, Missiles, Cars, Mobile Phones
Array Antennas	Yagi-Uda, Microstrip Patch Array, Aperture Array, Slotted Waveguide Array	High-Gain Applications, Radiation Pattern Control

## 2.3 ANTENNA ARRAY

Antenna arrays play a crucial role in the realm of wireless communication, with their significance expected to escalate further in the context of emerging technologies like 6G, and that is why the antenna array is a pillar for this work. An antenna array, composed of multiple individual antennas working collaboratively, offers distinctive advantages such as enhanced directional sensitivity, increased data rates, improved spatial diversity, and facilitating MIMO configurations for improved reliability (LIBERTI; RAPPAPORT, 1999). In 6G communication systems, where the demand for unprecedented data speeds, ultra-reliable low-latency communication, and massive device connectivity is paramount, antenna arrays shine as a key enabling technology. Their ability to spatially focus and steer signals, mitigate interference, and support beamforming techniques positions antenna arrays as instrumental components for achieving the ambitious goals of 6G networks, heralding a new era of high-performance and versatile wireless communication (ELZANATY *et al.*, 2023).

An antenna array refers to a configuration of multiple antennas working together as a collective unit. These antennas are strategically arranged to achieve specific performance characteristics that may not be possible with a single antenna. In this section, we will cover crucial concepts regarding antenna arrays, which will be very important throughout this work (TREES, 2002).

### 2.3.1 Basic of Array Signal Processing

We investigate the array's response to an external signal field, comprising isotropic sensors positioned at locations  $\mathbf{p}_m$ , as depicted in Fig. 2.5. The spatial sampling of the signal field at these positions  $\mathbf{p}_m$ , for  $m = 0, 1, \dots, M-1$ . An external signal field impinges on the array from the direction  $(\theta, \phi)$ , with  $\theta$  and  $\phi$  denoting the elevation angle and azimuth angle respectively (TREES, 2002).

For simplicity, the external signal field is depicted as a plane wave. The input comprises a plane wave propagating in the direction  $\mathbf{u}$  with a temporal frequency  $\omega$  (expressed in radians). The temporal responses at the sensors induced by this input can be described in two equivalent

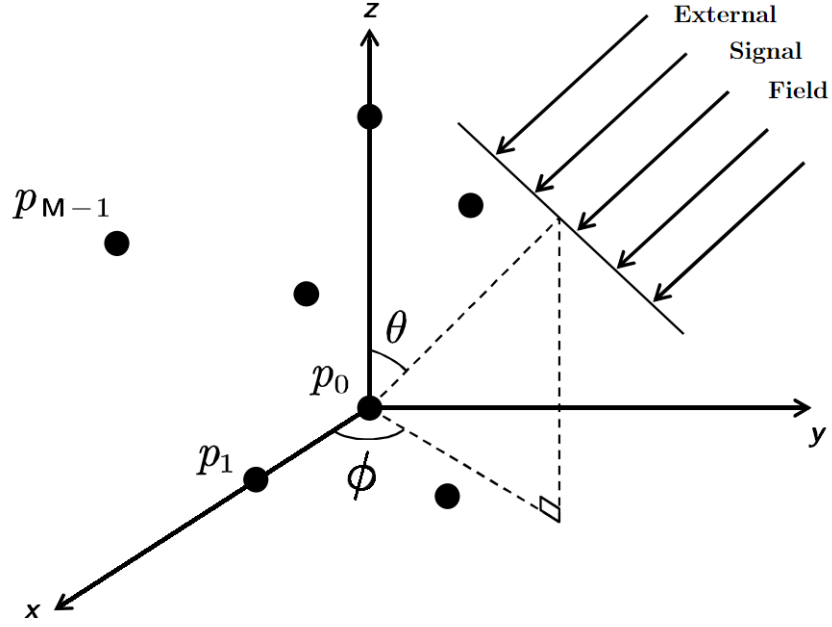


Figure 2.5: Signal receiving model. Adapted from (YANG, 2020) and (TREES, 2002).

ways. The first approach highlights the time delays associated with the arrival times at different sensors. Let  $s(t)$  be the signal observed at the origin of the coordinate system, and then the received signals at the sensor array can be given as (TREES, 2002):

$$\mathbf{s}(t, \mathbf{p}) = \begin{bmatrix} s(t - \tau_0) \\ s(t - \tau_1) \\ \vdots \\ s(t - \tau_{M-1}) \end{bmatrix}, \quad (2.24)$$

where

$$\tau_m = \frac{\mathbf{u}^T \mathbf{p}_m}{c} \quad (2.25)$$

and  $(\cdot)^T$  denotes the transpose operation.

The relationships between rectangular and spherical coordinates ( $x = r \sin \theta \cos \phi$ ,  $y = r \sin \theta \sin \phi$  and  $z = r \cos \theta$ ) the  $\mathbf{u}$  is a unit vector that can be expressed as:

$$\mathbf{u} = \begin{bmatrix} -\sin \theta \cos \phi \\ -\sin \theta \sin \phi \\ -\cos \theta \end{bmatrix}. \quad (2.26)$$

In many practical scenarios, signals are commonly modulated, and the signal observed at the origin of the coordinate system can be expressed as (YANG, 2020):

$$s(t) = m(t)e^{j2\pi f_0 t}, \quad (2.27)$$

where  $m(t)$  represents the modulation message or the complex envelope of  $s(t)$ , and  $f_0$  is the carrier frequency. Consequently, the received signal vector takes the form (YANG, 2020):

$$\mathbf{x}(t) = \begin{bmatrix} s(t - \tau_0) \\ s(t - \tau_1) \\ \vdots \\ s(t - \tau_{M-1}) \end{bmatrix} = \begin{bmatrix} m(t - \tau_0) e^{-j2\pi f_0 \tau_0} \\ m(t - \tau_1) e^{-j2\pi f_0 \tau_1} \\ \vdots \\ m(t - \tau_{M-1}) e^{-j2\pi f_0 \tau_{M-1}} \end{bmatrix} e^{j2\pi f_0 t}. \quad (2.28)$$

In practical scenarios, it is common for the complex envelope  $m(t)$  to exhibit narrowband characteristics, implying a much smaller bandwidth compared to the carrier frequency. This simplifies the signal expressions:

$$m(t) \simeq m(t - \tau_0) \simeq m(t - \tau_1) \simeq \cdots \simeq m(t - \tau_{M-1}). \quad (2.29)$$

Under this narrowband assumption, the received signal vector can be expressed as:

$$\mathbf{x}(t) = \begin{bmatrix} s(t - \tau_0) \\ s(t - \tau_1) \\ \vdots \\ s(t - \tau_{M-1}) \end{bmatrix} = m(t)e^{j2\pi f_0 t} \begin{bmatrix} e^{-j2\pi f_0 \tau_0} \\ e^{-j2\pi f_0 \tau_1} \\ \vdots \\ e^{-j2\pi f_0 \tau_{M-1}} \end{bmatrix} = s(t)\mathbf{a}(\theta, \phi). \quad (2.30)$$

Here, the steering vector the array manifold vector, denoted as  $\mathbf{a}(\theta, \phi)$ , is defined by:

$$\mathbf{a}(\theta, \phi) = \begin{bmatrix} e^{-j2\pi f_0 \tau_0} \\ e^{-j2\pi f_0 \tau_1} \\ \vdots \\ e^{-j2\pi f_0 \tau_{M-1}} \end{bmatrix}. \quad (2.31)$$

In an antenna array, the steering vector represents the spatial sensitivity pattern of the array with respect to the direction of incoming signals. It is a mathematical vector that describes how the signals from different directions are weighted or combined by the array elements. The steering vector is a crucial concept in array signal processing and beamforming (TREES, 2002).

Typically, there are multiple source signals, and the propagation environment introduces noise. Assuming there are  $K$  incoming signals, the signal received by the sensor array can be expressed as (YANG, 2020):

$$\mathbf{x}(t) = \begin{bmatrix} e^{-j2\pi f_0 \tau_{1,0}} & \dots & e^{-j2\pi f_0 \tau_{K,0}} \\ e^{-j2\pi f_0 \tau_{1,1}} & \dots & e^{-j2\pi f_0 \tau_{K,1}} \\ \vdots & \ddots & \vdots \\ e^{-j2\pi f_0 \tau_{1,M-1}} & \dots & e^{-j2\pi f_0 \tau_{K,M-1}} \end{bmatrix} \begin{bmatrix} s_1(t) \\ s_2(t) \\ \vdots \\ s_K(t) \end{bmatrix} + \begin{bmatrix} w_0(t) \\ w_1(t) \\ \vdots \\ w_{M-1}(t) \end{bmatrix}. \quad (2.32)$$

In this context,  $s_k(t)$  represents the signal transmitted by the  $k^{\text{th}}$  source and observed at the origin of the coordinate system ( $k = 1, 2, \dots, K$ ). Additionally,  $w_m(t)$  denotes the noise collected by the sensor element located at position  $\mathbf{p}_m$ . The term  $\tau_{k,m}$  signifies the time delay of the observation of  $s_k(t)$  at the sensor element at  $\mathbf{p}_m$  in relation to the observation at the origin of the coordinate system.

In matrix form, Eq. (2.32) can be expressed as:

$$\mathbf{x}(t) = \mathbf{A}\mathbf{s}(t) + \mathbf{w}(t). \quad (2.33)$$

Here,  $\mathbf{A}$  is the directional matrix of the sensor array, given by:

$$\mathbf{A} = [ \mathbf{a}(\theta_1, \phi_1) \quad \mathbf{a}(\theta_2, \phi_2) \quad \dots \quad \mathbf{a}(\theta_K, \phi_K) ], \quad (2.34)$$

where  $\mathbf{a}(\theta_k, \phi_k)$  is the directional vector associated with the  $k^{\text{th}}$  source. The incoming signal vector  $\mathbf{s}(t)$  is represented as:

$$\mathbf{s}(t) = [ s_1(t) \quad s_2(t) \quad \dots \quad s_K(t) ]^T \quad (2.35)$$

and the noise vector  $\mathbf{w}(t)$  is given by:

$$\mathbf{w}(t) = [ w_0(t) \quad w_1(t) \quad \dots \quad w_{M-1}(t) ]^T. \quad (2.36)$$

In general, the noise is assumed to be Gaussian white temporally and spatially, characterized by:

$$E \{ \mathbf{w}(t) \mathbf{w}^H(t) \} = \begin{bmatrix} \sigma^2 & & & \\ & \sigma^2 & & \\ & & \ddots & \\ & & & \sigma^2 \end{bmatrix} \quad (2.37)$$

where  $\sigma^2$  represents the power of the noise and is independent of the source signals.

The model for the signals observed by the sensor array comprises the directional matrix  $\mathbf{A}$ , the incoming signal vector  $\mathbf{s}(t)$ , and the noise vector  $\mathbf{w}(t)$ , as analyzed above.

## 2.3.2 Conventional Configurations of Sensor Arrays

### 2.3.2.1 Uniform Linear Array

A ULA, or Uniform Linear Array, is a type of sensor array configuration commonly used in signal processing and antenna systems. It consists of multiple sensor elements (or antennas) arranged linearly with uniform spacing between them. Fig. 2.6 illustrates a ULA with  $M$  sensors positioned along the  $X$ -axis, each spaced apart by a distance  $d$ . For mathematical convenience, we designate the first element of the array as the origin of the coordinate system (TREES, 2002).

The positions of the sensor elements can be written as:

$$\mathbf{p}_m = (md, 0, 0)^T \quad m = 0, 1, 2, \dots, M - 1. \quad (2.38)$$

Consider an incoming signal arriving at the ULA from a direction  $\theta$ . According to Eq. (2.25), the delay of the received signal at the sensor element positioned at  $\mathbf{p}_m$  relative to the signal observed at the origin of the coordinate system can be expressed as:

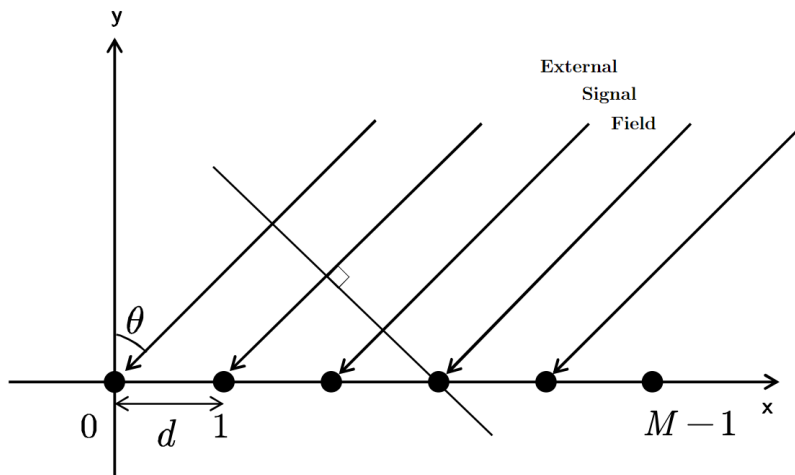


Figure 2.6: Signal receiving model. Adapted from (YANG, 2020) and (TREES, 2002).

$$\tau_m = -\frac{md \sin \theta}{c}. \quad (2.39)$$

Hence, the directional vector corresponding to the external signal field is expressed as:

$$\mathbf{a}_{ULA}(\theta) = \begin{bmatrix} 1 \\ e^{j2\pi f_0 \frac{d \sin \theta}{c}} \\ \vdots \\ e^{j2\pi f_0 \frac{(M-1)d \sin \theta}{c}} \end{bmatrix}. \quad (2.40)$$

For  $K$  source signals arriving from directions  $\{\theta_1, \theta_2, \dots, \theta_K\}$ , the signal received by the ULA is expressed as (YANG, 2020):

$$\mathbf{x}_{ULA}(t) = \mathbf{A}_{ULA} \mathbf{s}(t) + \mathbf{w}(t) \quad (2.41)$$

with the corresponding directional matrix of the ULA denoted as:

$$\mathbf{A}_{ULA} = [ \mathbf{a}_{ULA}(\theta_1) \quad \mathbf{a}_{ULA}(\theta_2) \quad \dots \quad \mathbf{a}_{ULA}(\theta_K) ]. \quad (2.42)$$

Typically, the inter-element spacing  $d$  of ULAs is set as  $d = \frac{\lambda}{2}$ . In this case,  $\mathbf{A}_{ULA}$  can be redefined as:

$$\mathbf{A}_{ULA} = \begin{bmatrix} 1 & 1 & \dots & 1 \\ e^{j\pi \sin \theta_1} & e^{j\pi \sin \theta_2} & \dots & e^{j\pi \sin \theta_K} \\ \vdots & \vdots & \ddots & \vdots \\ e^{j(M-1)\pi \sin \theta_1} & e^{j(M-1)\pi \sin \theta_2} & \dots & e^{j(M-1)\pi \sin \theta_K} \end{bmatrix}. \quad (2.43)$$

### 2.3.2.2 Uniform Planar Array

A Uniform Planar Array is a type of antenna array configuration that consists of multiple parallel ULAs arranged in a planar layout. Unlike a ULA, which is a one-dimensional array, a UPA enables the resolution of both elevation and azimuth angles. In a UPA, sensor elements are arranged in a grid pattern, forming rows and columns. This grid structure allows for improved spatial coverage and directional sensitivity. In Fig. 2.7, a UPA lies in the  $X - Z$  plane, containing  $M_y$  sensor elements in each column and  $M_x$  sensor elements in each row. The inter-element spacing is  $d$ , and the element in the first column and the first row serves as the origin of the coordinate system (TREES, 2002).

The position of the sensor elements is given by:

$$\mathbf{p}_{m_x, m_y} = (m_x d, 0, m_y d)^T \quad (2.44)$$

with  $m_x = 0, 1, 2, \dots, M_x - 1$  and  $m_y = 0, 1, 2, \dots, M_y - 1$ .

Suppose an incoming signal arrives at the UPA from direction  $(\theta, \phi)$ , with  $\theta$  and  $\phi$  representing the elevation and azimuth angles, respectively. For the ULA along the  $Z$ -axis, the time delay of the received signal at the sensor element located at  $\mathbf{p}_{0, m_y}$  concerning the signal observed at the origin is expressed as:

$$\tau_{0, m_y} = -\frac{m_y d \cos \theta}{c}. \quad (2.45)$$

The directional vector of the ULA associated with this incoming signal is:

$$\mathbf{a}_{ULA, Z}(\theta, \phi) = \begin{bmatrix} 1 \\ e^{j2\pi f_0 \frac{d \cos \theta}{c}} \\ \vdots \\ e^{j2\pi f_0 \frac{(M_y - 1)d \cos \theta}{c}} \end{bmatrix}. \quad (2.46)$$

For the ULA along the  $X$ -axis, the time delay of the received signal at the sensor element

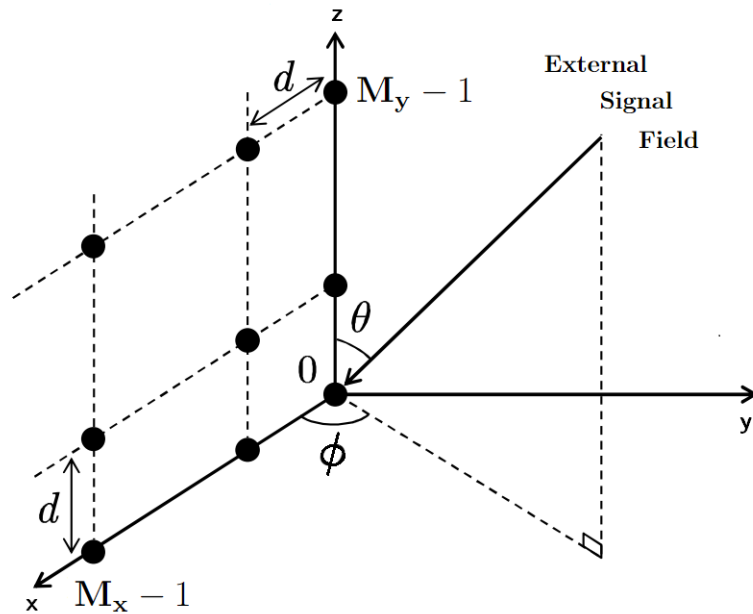


Figure 2.7: Signal receiving model. Adapted from (YANG, 2020) and (TREES, 2002).

located at  $\mathbf{p}_{m_x,0}$  concerning the signal observed at the origin is expressed as:

$$\tau_{m_x,0} = -\frac{m_x d \sin \theta \cos \phi}{c}. \quad (2.47)$$

The directional vector of the ULA associated with this incoming signal is:

$$\mathbf{a}_{ULA,X}(\theta, \phi) = \begin{bmatrix} 1 \\ e^{j2\pi f_0 \frac{d \sin \theta \cos \phi}{c}} \\ \vdots \\ e^{j2\pi f_0 \frac{(M_x-1)d \sin \theta \cos \phi}{c}} \end{bmatrix}. \quad (2.48)$$

The directional vector of the UPA associated with the incoming signal is then given by:

$$\mathbf{a}_{UPA}(\theta, \phi) = \mathbf{a}_{ULA,X}(\theta, \phi) \otimes \mathbf{a}_{ULA,Z}(\theta, \phi) \quad (2.49)$$

where  $\otimes$  represents the Kronecker product.

For  $K$  source signals arriving from directions  $\{(\theta_1, \phi_1) \quad (\theta_2, \phi_2) \quad \cdots \quad (\theta_K, \phi_K)\}$ , the signal received by the UPA is expressed as (YANG, 2020):

$$\mathbf{x}_{UPA}(t) = \mathbf{A}_{UPA} \mathbf{s}(t) + \mathbf{w}(t) \quad (2.50)$$

with the directional matrix of the UPA denoted as:

$$\mathbf{A}_{UPA} = \left[ \mathbf{a}_{UPA}(\theta_1, \phi_1) \quad \mathbf{a}_{UPA}(\theta_2, \phi_2) \quad \cdots \quad \mathbf{a}_{UPA}(\theta_K, \phi_K) \right]. \quad (2.51)$$

Setting the inter-element spacing  $d$  as  $\frac{\lambda}{2}$ , the directional matrix  $\mathbf{a}_{UPA}$  can be re-written as:

$$\mathbf{A}_{UPA} = \begin{bmatrix}
1 & \dots & 1 \\
e^{j\pi \cos \theta_1} & \dots & e^{j\pi \cos \theta_K} \\
\vdots & \ddots & \vdots \\
e^{j(M_y-1)\pi \cos \theta_1} & \dots & e^{j(M_y-1)\pi \cos \theta_K} \\
e^{j\pi \sin \theta_1 \cos \phi_1} & \dots & e^{j\pi \sin \theta_K \cos \phi_K} \\
e^{j\pi(\sin \theta_1 \cos \phi_1 + \cos \theta_1)} & \dots & e^{j\pi(\sin \theta_K \cos \phi_K + \cos \theta_K)} \\
\vdots & \ddots & \vdots \\
e^{j\pi(\sin \theta_1 \cos \phi_1 + (M_y-1) \cos \theta_1)} & \dots & e^{j\pi(\sin \theta_K \cos \phi_K + (M_y-1) \cos \theta_K)} \\
\vdots & \ddots & \vdots \\
e^{j(M_x-1)\pi \sin \theta_1 \cos \phi_1} & \dots & e^{j(M_x-1)\pi \sin \theta_K \cos \phi_K} \\
e^{j\pi((M_x-1) \sin \theta_1 \cos \phi_1 + \cos \theta_1)} & \dots & e^{j\pi((M_x-1) \sin \theta_K \cos \phi_K + \cos \theta_K)} \\
\vdots & \ddots & \vdots \\
e^{j\pi((M_x-1) \sin \theta_1 \cos \phi_1 + (M_y-1) \cos \theta_1)} & \dots & e^{j\pi((M_x-1) \sin \theta_K \cos \phi_K + (M_y-1) \cos \theta_K)}
\end{bmatrix}. \quad (2.52)$$

The antenna array, including ULA and URA configurations, holds a significant role in wireless communication due to their advantages. To enhance its performance even further, source localization has been studied extensively in the array processing literature. The next chapter explores measurement models and their intricacies for source localization.

# SOURCE LOCALIZATION

Recent years have seen rapidly increasing demand for services and systems that depend upon the accurate positioning of people and objects. This has led to the development and evolution of numerous positioning systems, that contribute significantly to fields such as acoustics, wireless communication, radar technology, and environmental monitoring. The process involves determining the spatial coordinates or position of a signal-emitting source based on measurements obtained from an array of sensors or receivers (GEZICI, 2008).

Source localization is a multidisciplinary field that combines principles from physics, signal processing, and mathematics. Researchers and engineers develop sophisticated algorithms and techniques to process sensor data, extract relevant information, and accurately estimate the source's location. The advancements in source localization methodologies contribute to the improvement of sensor technologies, enabling more precise and reliable measurements. Ultimately, the importance of source localization in scientific research lies in its ability to provide valuable insights, enhance decision-making processes, and contribute to the development of innovative solutions across a diverse range of applications (ZEKAVAT; BUEHRER, 2011).

In wireless communication, source localization plays a important role in locating mobile devices and identifying potential interference sources. The ability to determine the geographical location of signal-emitting devices is crucial for optimizing network performance, managing resources efficiently, and ensuring the security of wireless networks. Moreover, in radar systems, source localization enables the tracking and identification of objects in the airspace, facilitating applications in aviation, defense, and weather monitoring (BRENA *et al.*, 2017).

The significance of accurate source localization extends beyond traditional wireless communication applications, encompassing emerging technologies such as 5G and the Internet of Things (IoT). In 5G networks, where MIMO systems are deployed, antenna arrays enable the exploitation of spatial multiplexing and beamforming techniques, enhancing both data rates

and spectral efficiency. Furthermore, in IoT deployments, source localization contributes to the efficient management of connected devices by providing valuable spatial context. As wireless communication systems continue to evolve, the continued advancement of source localization techniques, particularly those leveraging antenna arrays, remains crucial for optimizing network performance and enabling novel applications in diverse domains (GEOK *et al.*, 2020).

### 3.1 MEASUREMENT MODELS AND PRINCIPLES FOR SOURCE LOCALIZATION

The determination of a source’s location based on measurements collected from an array of spatially separated sensors has been a pivotal challenge across various domains, including radar, sonar, Global Positioning Systems (GPS), mobile communications, multimedia, and wireless sensor networks. Commonly employed measurements for source localization encompass TOA, TDOA, TSOA, RSS, and DOA. Essentially, TOAs, TDOAs, TSOAs, and RSSs provide distance information between the source and sensors, whereas DOAs indicate the source bearings relative to the receivers. Despite their significance, achieving accurate positioning is intricate due to the nonlinear relationships inherent in these measurements with respect to the source location (GEZICI, 2008).

The primary learning objectives for this chapter encompass: (i) gaining a comprehensive understanding of the development of positioning algorithms utilizing TOA, TDOA, TSOA, RSS, and DOA measurements; and (ii) acquiring knowledge about the performance metrics associated with position estimation (ZEKAVAT; BUEHRER, 2011).

#### 3.1.1 TOA

TOA signifies the unidirectional time taken by a signal to traverse the distance between a source and a receiver. Achieving precise synchronization among the target and all receivers is essential for obtaining accurate TOA information, though this synchronization requirement can be relaxed if measuring the round-trip or two-way TOA. The distance between the source and the receiver is determined by multiplying the TOA by the known propagation speed of the electromagnetic wave in the air, denoted as  $c$  (GEZICI, 2008).

For instance, in scenarios where sound and light propagate through air, the speeds are approximate  $c_s \approx 340 \text{ ms}^{-1}$  and  $c \approx 3 \times 10^8 \text{ ms}^{-1}$  m/s respectively. Assuming no measurement error, each TOA corresponds to a circle centered at a receiver, where the source must lie in 2D space. As discussed previously, geometrically, three or more noise-free TOA-derived circles intersect uniquely at a point, representing the source position. This implies that at least three sensors are required for 2D positioning. However, two TOA circles typically intersect at two points, indicating two potential source locations. Despite this, the circles may not intersect or could have multiple intersections in the presence of disturbances, rendering direct circle-based solutions ineffective. With three or more receivers, it becomes more suitable to transform the noisy TOAs into a series of circular equations. These equations are then utilized within an optimization framework, considering the sensor array geometry, to determine the source position (ZEKAVAT; BUEHRER, 2011).

Mathematically, the TOA measurement model is formulated as follows. Let  $\mathbf{x} = [x \ y]^T$  be the unknown source position and  $\mathbf{x}_m = [x_m \ y_m]^T$  be the known coordinates of the  $M$  th sensor,  $m = 1, 2, \dots, M$ , for now  $M \geq 3$  is the number of receivers. The distance between the source and the  $M$  th sensor, denoted by  $d_m$ , is simply (ZEKAVAT; BUEHRER, 2011) (BRENA *et al.*, 2017):

$$d_m = \|\mathbf{x} - \mathbf{x}_m\|_2 = \sqrt{(x - x_m)^2 + (y - y_m)^2}, \quad m = 1, 2, \dots, M. \quad (3.1)$$

Rewriting Eq. (2.25) in terms of  $d_m$ , we make the assumption, without loss of generality, that the source emits a signal at time 0 and the  $M$ th sensor receives it at time  $t_{TOA}$  denoted as:

$$t_{TOA} = \frac{d_m}{c}, \quad m = 1, 2, \dots, M. \quad (3.2)$$

In practice, TOAs are susceptible to measurement errors. As a result, the range measurement based on multiplying  $t_{TOA}$  by  $c$ , denoted by  $y_{TOA,m}$ , is modeled as:

$$x_{TOA,m} = d_m + w_{TOA,m} = \sqrt{(x - x_m)^2 + (y - y_m)^2} + w_{TOA,m}, \quad m = 1, 2, \dots, M, \quad (3.3)$$

where  $w_{TOA,m}$  is the range error in  $x_{TOA,m}$ , which is resulted from the TOA disturbance.

The Eq. (3.3) can be succinctly expressed in vector form as:

$$\mathbf{x}_{\text{TOA}} = \mathbf{s}_{\text{TOA}}(\mathbf{x}) + \mathbf{w}_{\text{TOA}}, \quad (3.4)$$

where

$$\begin{aligned} \mathbf{x}_{\text{TOA}} &= [x_{\text{TOA},1} \ x_{\text{TOA},2} \ \cdots \ x_{\text{TOA},m}]^T, \\ \mathbf{w}_{\text{TOA}} &= [w_{\text{TOA},1} \ w_{\text{TOA},2} \ \cdots \ w_{\text{TOA},m}]^T, \end{aligned} \quad (3.5)$$

and

$$\mathbf{s}_{\text{TOA}}(\mathbf{x}) = \mathbf{d} = \begin{bmatrix} \sqrt{(x-x_1)^2 + (y-y_1)^2} \\ \sqrt{(x-x_2)^2 + (y-y_2)^2} \\ \vdots \\ \sqrt{(x-x_m)^2 + (y-y_m)^2} \end{bmatrix}. \quad (3.6)$$

In this context,  $\mathbf{s}_{\text{TOA}}(\mathbf{x})$  denotes the established function, inherently dependent on the parameter vector  $\mathbf{x}$  and essentially representing the noise-free distance vector. The source localization problem based on TOA measurements is to estimate  $\mathbf{x}$  given  $\mathbf{x}_{\text{TOA}}$ , defined in Eq. (3.4).

For streamlined algorithm development, rigorous analysis, and Cramér-Rao Lower Bound (CRLB) computation, we adopt the assumption that  $\{w_{\text{TOA},m}\}$  constitutes zero-mean uncorrelated Gaussian processes characterized by variances  $\{\sigma_{\text{TOA},m}^2\}$ . Notably, the zero-mean property signifies Line-of-Sight (LOS) transmission. The Probability Density Function (PDF) governing each scalar random variable  $x_{\text{TOA},m}$ , denoted as  $p(x_{\text{TOA},m})$ , takes the form of (ZEKAVAT; BUEHRER, 2011):

$$p(x_{\text{TOA},m}) = \frac{1}{\sqrt{2\pi\sigma_{\text{TOA},m}^2}} \exp\left(-\frac{1}{2\sigma_{\text{TOA},m}^2} (x_{\text{TOA},m} - d_m)^2\right) \quad (3.7)$$

which is characterized by its mean and variance,  $d_m$  and  $\sigma_{\text{TOA},m}^2$ , respectively. In other words, we can write  $x_{\text{TOA},m} \sim \mathcal{N}(d_m, \sigma_{\text{TOA},m}^2)$ . The PDF for  $\mathbf{x}_{\text{TOA}}$ , denoted by  $p(\mathbf{x}_{\text{TOA}})$ , is:

$$p(\mathbf{x}_{\text{TOA}}) = \frac{1}{(2\pi)^{M/2} |\mathbf{C}_{\text{TOA}}|^{1/2}} \exp\left(-\frac{1}{2} (\mathbf{x}_{\text{TOA}} - \mathbf{d})^T \mathbf{C}_{\text{TOA}}^{-1} (\mathbf{x}_{\text{TOA}} - \mathbf{d})\right), \quad (3.8)$$

where  $\mathbf{C}_{\text{TOA}}$  is the covariance matrix for  $\mathbf{x}_{\text{TOA}}$  which corresponds to:

$$\begin{aligned}\mathbf{C}_{\text{TOA}} &= E \left\{ (\mathbf{x}_{\text{TOA}} - \mathbf{d}) (\mathbf{x}_{\text{TOA}} - \mathbf{d})^T \right\} \\ &= E \left\{ \mathbf{w}_{\text{TOA}} \mathbf{w}_{\text{TOA}}^T \right\} \\ &= \text{diag} \left( \sigma_{\text{TOA},1}^2, \sigma_{\text{TOA},2}^2, \dots, \sigma_{\text{TOA},m}^2 \right).\end{aligned}\tag{3.9}$$

In Eq. (3.9), the third equality is deduced using the assumption of uncorrelated  $\{\mathbf{w}_{\text{TOA},l}\}$ . Using Eq. (3.9), into Eq. (3.8) we obtain: (ZEKAVAT; BUEHRER, 2011):

$$p(\mathbf{x}_{\text{TOA}}) = \frac{1}{(2\pi)^{M/2} \prod_{m=1}^M \sigma_{\text{TOA},m}} \exp \left( -\frac{1}{2} \sum_{m=1}^M \frac{(\mathbf{x}_{\text{TOA},m} - d_m)^2}{\sigma_{\text{TOA},m}^2} \right).\tag{3.10}$$

In other words, we can write  $\mathbf{x}_{\text{TOA}} \sim \mathcal{N}(\mathbf{d}, \text{diag}(\sigma_{\text{TOA},1}^2, \sigma_{\text{TOA},2}^2, \dots, \sigma_{\text{TOA},m}^2))$ .

### 3.1.2 TDOA

TDOA involves calculating the time difference in signal arrival between a pair of sensors, necessitating synchronized clocks across all receivers. However, it offers a simpler alternative to the TOA method, which demands source synchronization, incurring higher hardware costs. Analogous to TOA, multiplying the TDOA by the known propagation speed yields the range difference between a source and two receivers. As outlined in Chapter 1, each noise-free TDOA geometrically defines a hyperbola in the 2D space, with the source located at its intersection with at least two hyperbolae. In the presence of disturbances, our approach involves estimating  $\mathbf{x}$  from a set of hyperbolic equations derived from the TDOA measurements (GEOK *et al.*, 2020).

The TDOA measurement model is expressed mathematically as follows. We assume that the source emits a signal at the unknown time  $t_0$ , and the  $M$ -th sensor receives it at time  $t_m, m = 1, 2, \dots, M$ , with  $M \geq 3$ . There exist  $M(M-1)/2$  distinct TDOAs from all possible sensor pairs, denoted by  $t_{l,m} = (t_l - t_0) - (t_m - t_0) = t_l - t_m, m, l = 1, 2, \dots, L$ , where  $l > m$ . However, only  $(M-1)$  TDOAs are nonredundant. For instance, considering  $M = 3$ , the distinct TDOAs are  $t_{2,1}, t_{3,1}$ , and  $t_{3,2}$ , with the observation that  $t_{3,2} = t_{3,1} - t_{2,1}$  being redundant. To reduce complexity without compromising estimation performance, it is advisable to measure all  $M(M-1)/2$  TDOAs and then convert them into  $(M-1)$  nonredundant TDOAs for source

localization (SO *et al.*, 2008). Without loss of generality, we designate the first sensor as the reference, and the nonredundant TDOAs are  $t_{m,1}, m = 2, 3, \dots, M$  (ZEKAVAT; BUEHRER, 2011) (GEOK *et al.*, 2020).

Similar to Eq.(3.2) and Eq. (3.3), the range difference measurements deduced from the TDOAs are modeled as:

$$\mathbf{x}_{\text{TDOA},m} = d_{m,1} + \mathbf{w}_{\text{TDOA},m}, \quad m = 2, 3, \dots, M, \quad (3.11)$$

where

$$d_{m,1} = d_m - d_1, \quad (3.12)$$

and  $\mathbf{w}_{\text{TDOA},m}$  is the range difference error in  $\mathbf{x}_{\text{TDOA},m}$  which is proportional to the disturbance in  $t_{l,1}$ . Following Eq. (3.4) - Eq. (3.6), the TDOA measurement model in vector form is:

$$\mathbf{x}_{\text{TDOA}} = \mathbf{s}_{\text{TDOA}}(\mathbf{x}) + \mathbf{w}_{\text{TDOA}}, \quad (3.13)$$

where

$$\begin{aligned} \mathbf{x}_{\text{TDOA}} &= \left[ \mathbf{x}_{\text{TDOA},2} \quad \mathbf{x}_{\text{TDOA},3} \quad \cdots \quad \mathbf{x}_{\text{TDOA},M} \right]^T, \\ \mathbf{w}_{\text{TDOA}} &= \left[ \mathbf{w}_{\text{TDOA},2} \quad \mathbf{w}_{\text{TDOA},3} \quad \cdots \quad \mathbf{w}_{\text{TDOA},M} \right]^T, \end{aligned} \quad (3.14)$$

and

$$\mathbf{s}_{\text{TDOA}}(\mathbf{x}) = \mathbf{d}_1 = \begin{bmatrix} \sqrt{(x - x_2)^2 + (y - y_2)^2} - \sqrt{(x - x_1)^2 + (y - y_1)^2} \\ \sqrt{(x - x_3)^2 + (y - y_3)^2} - \sqrt{(x - x_1)^2 + (y - y_1)^2} \\ \vdots \\ \sqrt{(x - x_M)^2 + (y - y_M)^2} - \sqrt{(x - x_1)^2 + (y - y_1)^2} \end{bmatrix}. \quad (3.15)$$

The source localization problem based on TDOA measurements is to estimate  $\mathbf{x}$  given  $\{\mathbf{x}_{\text{TDOA},m}\}$  or  $\mathbf{x}_{\text{TDOA}}$ . Assuming that  $\mathbf{w}_{\text{TDOA}}$  is zero-mean and Gaussian distributed, the PDF for  $\mathbf{x}_{\text{TDOA}}$ , denoted by  $p(\mathbf{x}_{\text{TDOA}})$ , is (ZEKAVAT; BUEHRER, 2011):

$$p(\mathbf{x}_{\text{TDOA}}) = \frac{1}{(2\pi)^{(M-1)/2} |\mathbf{C}_{\text{TDOA}}|^{1/2}} \exp\left(-\frac{1}{2} (\mathbf{x}_{\text{TDOA}} - \mathbf{d}_1)^T \mathbf{C}_{\text{TDOA}}^{-1} (\mathbf{x}_{\text{TDOA}} - \mathbf{d}_1)\right), \quad (3.16)$$

where  $\mathbf{C}_{\text{TDOA}}$  is the covariance matrix for  $\mathbf{x}_{\text{TDOA}}$ . Alternatively, we can write  $\mathbf{x}_{\text{TDOA}} \sim \mathcal{N}(\mathbf{d}_1, \mathbf{C}_{\text{TDOA}})$ . Since all TDOAs are determined with respect to the first sensor,  $w_{\text{TDOA},m}$ ,  $m = 2, 3, \dots, M$ , are correlated. As a result,  $\mathbf{C}_{\text{TDOA}}$  is not a diagonal matrix (SO *et al.*, 2008).

### 3.1.3 TSOA

TSOA emerges in MIMO (LI; STOICA, 2008) and multistatic (RUI; HO, 2015) systems, comprising two sets of sensors: transmitters and receivers. A prominent example is the distributed MIMO radar, featuring widely spaced transmit and receive antennas. Similar to TDOA, achieving clock synchronization across all transmitters and receivers is essential. In this scenario, a transmitter emits a signal to the source, which reflects and is collected at a receiver. The total propagation time from the transmit antenna to the receive antenna is termed TSOA. Multiplying TSOA by the signal propagation speed provides the transmitter-target-receiver distance or range sum, representing the sum of the distances between the transmitter and source and between the source and receiver. Geometrically, each noise-free TSOA defines an ellipse in 2D space, on which the source must lie, with the target location determined by the intersection of at least three ellipses. In the presence of disturbances, we estimate  $\mathbf{x}$  from a set of elliptic equations derived from TSOA measurements. Notably, range, range difference, and range sum are key distance-based location-bearing measurements corresponding to circular, hyperbolic, and elliptic localization, respectively. Additionally, each range, range difference, and range sum define a sphere, hyperboloid, and ellipsoid, respectively, in the 3D case (GEZICI, 2008).

The TSOA measurement model is mathematically formulated as follows. To streamline notation, we introduce  $\mathbf{x}_l^t = [x_l^t \ y_l^t]^T$  as the known position of the  $l$ -th transmitter, where  $l = 1, 2, \dots, L$  and  $L \geq 1$ . We utilize  $\{\mathbf{x}_m\}$  to represent the positions of the  $M$  receivers. Drawing from Eq. (3.2) and Eq. (3.3), and recognizing that TSOA is the sum of two TOAs, the range sum measurements derived from the TSOAs, denoted by  $x_{\text{TSOA},l,m}$ , are modeled as (ZEKAVAT; BUEHRER, 2011) (GEOK *et al.*, 2020):

$$x_{\text{TSOA},l,m} = d_l^t + d_m + w_{\text{TSOA},l,m}, \quad l = 1, 2, \dots, L, \quad m = 1, 2, \dots, M, \quad (3.17)$$

where

$$d_l^t = \sqrt{(x - x_l^t)^2 + (y - y_l^t)^2} \quad (3.18)$$

and  $w_{\text{TSOA},l,m}$  is the range sum error in  $x_{\text{TSOA},l,m}$ , which is resulted from the TSOA disturbance.

Similar to Eq. (3.4) - Eq. (3.6), the TSOA measurement model in vector form is:

$$\mathbf{x}_{\text{TSOA}} = \mathbf{s}_{\text{TSOA}}(\mathbf{x}) + \mathbf{w}_{\text{TSOA}}, \quad (3.19)$$

where

$$\begin{aligned} \mathbf{x}_{\text{TSOA}} &= [x_{\text{TSOA},1,1} \quad x_{\text{TSOA},2,1} \quad \cdots \quad x_{\text{TSOA},L,1} \quad x_{\text{TSOA},1,2} \quad \cdots \quad x_{\text{TSOA},L,M}]^T, \\ \mathbf{w}_{\text{TSOA}} &= [w_{\text{TSOA},1,1} \quad w_{\text{TSOA},2,1} \quad \cdots \quad w_{\text{TSOA},L,1} \quad w_{\text{TSOA},1,2} \quad \cdots \quad w_{\text{TSOA},L,M}]^T \end{aligned} \quad (3.20)$$

and

$$\mathbf{s}_{\text{TSOA}}(\mathbf{x}) = \mathbf{d}_2 = \begin{bmatrix} \sqrt{(x - x_1^t)^2 + (y - y_1^t)^2} + \sqrt{(x - x_1)^2 + (y - y_1)^2} \\ \sqrt{(x - x_2^t)^2 + (y - y_2^t)^2} + \sqrt{(x - x_1)^2 + (y - y_1)^2} \\ \vdots \\ \sqrt{(x - x_L^t)^2 + (y - y_L^t)^2} + \sqrt{(x - x_1)^2 + (y - y_1)^2} \\ \sqrt{(x - x_1^t)^2 + (y - y_1^t)^2} + \sqrt{(x - x_2)^2 + (y - y_2)^2} \\ \vdots \\ \sqrt{(x - x_L^t)^2 + (y - y_L^t)^2} + \sqrt{(x - x_M)^2 + (y - y_M)^2} \end{bmatrix}. \quad (3.21)$$

The TSOA-based localization problem is to estimate  $\mathbf{x}$  given the  $LM$  measurements of  $\{x_{\text{TSOA},l,m}\}$  or  $\mathbf{x}_{\text{TSOA}}$ .

Assuming that  $\{w_{\text{TSOA},l,m}\}$  are zero-mean uncorrelated Gaussian processes with variances  $\{\sigma_{\text{TSOA},l,m}^2\}$ , the PDF for  $\mathbf{x}_{\text{TSOA}}$ , denoted by  $p(\mathbf{x}_{\text{TSOA}})$ , is:

$$\begin{aligned} p(\mathbf{x}_{\text{TSOA}}) &= \frac{1}{(2\pi)^{LM/2} |\mathbf{C}_{\text{TSOA}}|^{1/2}} \exp\left(-\frac{1}{2} (\mathbf{x}_{\text{TSOA}} - \mathbf{d}_2)^T \mathbf{C}_{\text{TSOA}}^{-1} (\mathbf{x}_{\text{TSOA}} - \mathbf{d}_2)\right) \\ &= \frac{1}{(2\pi)^{LM/2} \prod_{l=1}^L \prod_{m=1}^M \sigma_{\text{TSOA},l,m}^2} \exp\left(-\frac{1}{2} \sum_{l=1}^L \sum_{m=1}^M \frac{(x_{\text{TSOA},l,m} - d_l^t - d_m)^2}{\sigma_{\text{TSOA},l,m}^2}\right), \end{aligned} \quad (3.22)$$

where  $\mathbf{C}_{\text{TSOA}} = \text{diag}(\sigma_{\text{TSOA},1,1}^2, \sigma_{\text{TSOA},2,1}^2, \cdots, \sigma_{\text{TSOA},L,1}^2, \sigma_{\text{TSOA},1,2}^2, \cdots, \sigma_{\text{TSOA},L,M}^2)$  represents the covariance matrix for  $\mathbf{x}_{\text{TSOA}}$ . That is, we can also write  $\mathbf{x}_{\text{TSOA}} \sim \mathcal{N}(\mathbf{d}_2, \mathbf{C}_{\text{TSOA}})$ .

### 3.1.4 RSS

The RSS represents the average power received at a sensor originating from the emitted source. It is commonly assumed that the received power adheres to an exponential decay model, dependent on the transmitted power, path loss constant, and the distance between the source and the sensor. This positioning scheme offers simplicity compared to methods involving TOA, TDOA, or TSOA measurements, as it does not necessitate synchronization among the source and/or sensors. Once distances are derived from the RSS measurements, determining the source location becomes feasible, akin to the TOA scenario with the utilization of at least three receivers (GEOK *et al.*, 2020).

The RSS measurement model is formulated as follows. Assuming the source transmitted power is  $P_t$  and in the absence of disturbance, the average power received at the  $M$ -th sensor, denoted by  $P_{r,m}$ , is modeled as (SONG, 1994):

$$P_{r,m} = K_m P_t d_m^{-\alpha} = K_m P_t \|\mathbf{x} - \mathbf{x}_m\|_2^{-\alpha}, \quad m = 1, 2, \dots, M, \quad (3.23)$$

where  $K_m$  encompasses all other factors affecting the received power, such as antenna height and gain, while  $\alpha$  represents the path loss constant. Depending on the propagation environment,  $\alpha$  can vary from 2 to 5, with  $\alpha = 2$  specifically in free space. It is assumed that  $P_t, K_m, m = 1, 2, \dots, M$  with  $M \geq 3$  and  $\alpha$  are known a priori. Field trials have corroborated that disturbances in RSS follow a log-normal distribution. Thus, the log-normal path loss model can be expressed as:

$$\ln(P_{r,m}) = \ln(K_m) + \ln(P_t) - \alpha \ln(d_m) + w_{\text{RSS},m}, \quad m = 1, 2, \dots, M, \quad (3.24)$$

where the disturbance  $w_{\text{RSS},m}$  is now Gaussian distributed. For simplicity, we assume that  $w_{\text{RSS},m}, m = 1, 2, \dots, M$ , are zero-mean uncorrelated Gaussian processes with variances  $\{\sigma_{\text{RSS},m}^2\}$ . Let

$$x_{\text{RSS},m} = \ln(P_{r,m}) - \ln(K_m) - \ln(P_t). \quad (3.25)$$

The RSS measurement model is simplified to:

$$\mathbf{x}_{\text{RSS},m} = -\alpha \ln(d_m) + \mathbf{w}_{\text{RSS},m}, \quad m = 1, 2, \dots, M. \quad (3.26)$$

The vector form of Eq. (3.26) is then:

$$\mathbf{x}_{\text{RSS}} = \mathbf{s}_{\text{RSS}}(\mathbf{x}) + \mathbf{w}_{\text{RSS}}, \quad (3.27)$$

where

$$\begin{aligned} \mathbf{x}_{\text{RSS}} &= \begin{bmatrix} \mathbf{x}_{\text{RSS},1} & \mathbf{x}_{\text{RSS},2} & \cdots & \mathbf{x}_{\text{RSS},m} \end{bmatrix}^T, \\ \mathbf{w}_{\text{RSS}} &= \begin{bmatrix} \mathbf{w}_{\text{RSS},1} & \mathbf{w}_{\text{RSS},2} & \cdots & \mathbf{w}_{\text{RSS},m} \end{bmatrix}^T, \end{aligned} \quad (3.28)$$

and

$$\mathbf{s}_{\text{RSS}}(\mathbf{x}) = \mathbf{p} = -\alpha \begin{bmatrix} \ln \left( \sqrt{(x - x_1)^2 + (y - y_1)^2} \right) \\ \ln \left( \sqrt{(x - x_2)^2 + (y - y_2)^2} \right) \\ \vdots \\ \ln \left( \sqrt{(x - x_M)^2 + (y - y_M)^2} \right) \end{bmatrix}. \quad (3.29)$$

Comparing with Eq. (3.6), we observe that  $\mathbf{s}_{\text{RSS}}(\mathbf{x})$  also contains range information. The source localization problem based on RSS measurements is to estimate  $\mathbf{x}$  given  $\{\mathbf{x}_{\text{RSS},m}\}$  or  $\mathbf{x}_{\text{RSS}}$ . Following the development in Eq. (3.7) - Eq. (3.10), the PDF for  $\mathbf{x}_{\text{RSS}}$ , denoted by  $p(\mathbf{x}_{\text{RSS}})$ , is determined as:

$$\begin{aligned} p(\mathbf{x}_{\text{RSS}}) &= \frac{1}{(2\pi)^{M/2} |\mathbf{C}_{\text{RSS}}|^{1/2}} \exp \left( -\frac{1}{2} (\mathbf{x}_{\text{RSS}} - \mathbf{p})^T \mathbf{C}_{\text{RSS}}^{-1} (\mathbf{x}_{\text{RSS}} - \mathbf{p}) \right) \\ &= \frac{1}{(2\pi)^{M/2} \prod_{m=1}^M \sigma_{\text{RSS},m}^2} \exp \left( -\frac{1}{2} \sum_{m=1}^M \frac{(\mathbf{x}_{\text{RSS},m} + \alpha \ln(d_m))^2}{\sigma_{\text{RSS},m}^2} \right), \end{aligned} \quad (3.30)$$

where  $\mathbf{C}_{\text{RSS}} = \text{diag}(\sigma_{\text{RSS},1}^2, \sigma_{\text{RSS},2}^2, \dots, \sigma_{\text{RSS},L}^2)$ . In other words,  $\mathbf{x}_{\text{RSS}} \sim \mathcal{N}(\mathbf{p}, \mathbf{C}_{\text{RSS}})$ .

It is noteworthy that when the source transmitted power is unknown, leveraging the differential RSS measurements (LIN *et al.*, 2013), akin to range difference information in TDOA, becomes instrumental for positioning.

### 3.1.5 DOA

DOA represents the arrival angle of the emitted source signal observed at a receiver. Each DOA allows the drawing of a Line of Bearing (LOB) from the source to the receiver, and the intersection of at least two LOBs provides the source location. Although this scheme doesn't necessitate clock synchronization like RSS-based positioning, it does require an antenna array installation at each receiver for DOA estimation. Let  $\phi_m$  denote the DOA between the source and the  $M$ -th receiver, and we have (BRENA *et al.*, 2017):

$$\tan(\phi_m) = \frac{y - y_m}{x - x_m}, \quad m = 1, 2, \dots, M \quad (3.31)$$

with  $M \geq 2$ . Geometrically,  $\phi_m$  represents the angle between the LOB from the  $M$ -th receiver to the target and the  $x$ -axis. The DOA measurements in the presence of angle errors, denoted by  $\{x_{\text{DOA},m}\}$ , are modeled as (ZEKAVAT; BUEHRER, 2011):

$$x_{\text{DOA},m} = \phi_m + w_{\text{DOA},m} = \tan^{-1}\left(\frac{y - y_m}{x - x_m}\right) + w_{\text{DOA},m}, \quad m = 1, 2, \dots, M, \quad (3.32)$$

where  $\{w_{\text{DOA},m}\}$  are the noises in  $\{x_{\text{DOA},m}\}$ , assumed to be zero-mean uncorrelated Gaussian processes with variances  $\{\sigma_{\text{DOA},m}^2\}$ . The vector form of Eq. (3.32) is:

$$\mathbf{x}_{\text{DOA}} = \mathbf{s}_{\text{DOA}}(\mathbf{x}) + \mathbf{w}_{\text{DOA}}, \quad (3.33)$$

where

$$\begin{aligned} \mathbf{x}_{\text{DOA}} &= [x_{\text{DOA},1} \quad x_{\text{DOA},2} \quad \cdots \quad x_{\text{DOA},m}]^T, \\ \mathbf{w}_{\text{DOA}} &= [w_{\text{DOA},1} \quad w_{\text{DOA},2} \quad \cdots \quad w_{\text{DOA},m}]^T \end{aligned} \quad (3.34)$$

and

$$\mathbf{s}_{\text{DOA}}(\mathbf{x}) = \phi = \begin{bmatrix} \tan^{-1}\left(\frac{y-y_1}{x-x_1}\right) \\ \tan^{-1}\left(\frac{y-y_2}{x-x_2}\right) \\ \vdots \\ \tan^{-1}\left(\frac{y-y_m}{x-x_m}\right) \end{bmatrix}. \quad (3.35)$$

The source localization problem based on DOA measurements is to estimate  $\mathbf{x}$  given  $\mathbf{x}_{\text{DOA},m}$ ,  $m = 1, 2, \dots, M$ , or  $\mathbf{x}_{\text{DOA}}$ . Following the development in Eq. (3.7) - Eq. (3.10), the PDF for  $\mathbf{x}_{\text{DOA}}$ , denoted by  $p(\mathbf{x}_{\text{DOA}})$ , is

$$\begin{aligned} p(\mathbf{x}_{\text{DOA}}) &= \frac{1}{(2\pi)^{M/2} |\mathbf{C}_{\text{DOA}}|^{1/2}} \exp\left(-\frac{1}{2} (\mathbf{x}_{\text{DOA}} - \phi)^T \mathbf{C}_{\text{DOA}}^{-1} (\mathbf{x}_{\text{DOA}} - \phi)\right) \\ &= \frac{1}{(2\pi)^{M/2} \prod_{m=1}^M \sigma_{\text{DOA},m}} \exp\left(-\frac{1}{2} \sum_{m=1}^M \frac{(\mathbf{x}_{\text{DOA},m} - \phi_m)^2}{\sigma_{\text{DOA},m}^2}\right), \end{aligned} \quad (3.36)$$

where  $\mathbf{C}_{\text{DOA}} = \text{diag}(\sigma_{\text{DOA},1}^2, \sigma_{\text{DOA},2}^2, \dots, \sigma_{\text{DOA},M}^2)$ . In other words, we can write  $\mathbf{x}_{\text{DOA}} \sim \mathcal{N}(\phi, \mathbf{C}_{\text{DOA}})$ .

A comparative analysis of the five measurement models is presented in Table 3.1 (ZEKAVAT; BUEHRER, 2011):

Based on the comparison, the DOA technique stands out as advantageous for its simplicity, as it only requires at least two receivers and does not require time synchronization. However, it is worth noting that smart antennas are needed for DOA, and the method assumes LOS

Table 3.1: Comparison of Location Estimation Techniques

Model	Location Information	Advantages	Disadvantages
TOA	Range	- High accuracy.	- Requires time synchronization across sources and all receivers (Note: synchronization not needed for round-trip TOA). - Assumes LOS.
TDOA	Range difference	- High accuracy. - No time synchronization required at the source.	- Assumes LOS.
TSOA	Range sum	- High accuracy. - No time synchronization required at the source.	- Requires multiple transmitters and receivers. - Assumes LOS.
RSS	Range	- Simple and inexpensive. - No time synchronization required.	- Lower accuracy.
DOA	Bearing	- Only requires at least two receivers. - No time synchronization required.	- Requires smart antennas. - Assumes LOS.

conditions.

## 3.2 DOA ESTIMATION

DOA estimation is a key technique in the fields of signal processing and communication engineering and compared to other techniques, DOA estimation offers several key advantages, making it an essential tool in various industries (CHEN *et al.*, 2010).

1. **Precise Localization:** One of the primary reasons for the importance of DOA estimation is its ability to accurately localize a signal source. This is especially useful in applications such as radar systems, where the precise location of a target is crucial for effective tracking and detection. DOA estimation allows for localization with high accuracy, even in noisy environments (ABOUTANIOS *et al.*, 2017).
2. **Multiple Source Detection:** DOA estimation not only determines the direction of a single source but can also detect and estimate the directions of multiple sources simultaneously. This is possible through the use of smart antenna arrays that can distinguish and separate signals from different sources based on their angles of arrival. This capability is particularly useful in wireless communication systems, where multiple users may transmit signals at the same time (SAWADA *et al.*, 2003).
3. **Improved Signal Quality:** DOA estimation plays a vital role in improving the overall signal quality. By estimating the direction of a signal source, it is possible to filter out unwanted noise and interference, resulting in a cleaner and more reliable signal. This is especially important in applications such as audio processing, where accurate direction estimation can significantly enhance the listening experience (DEY; ASHOUR, 2018).
4. **Cost-Efficient:** Compared to other localization techniques, DOA estimation is relatively cost-efficient. It does not require expensive hardware or complex algorithms, making it accessible to a wide range of applications and industries. This is particularly beneficial for businesses and organizations that may not have the resources to invest in more sophisticated techniques (HUSAIN *et al.*, 2017).
5. **Efficient Resource Management:** DOA estimation can also help with efficient resource

management. By accurately locating the source of a signal, it is possible to focus transmission and reception in that direction, resulting in more efficient use of resources. This is particularly important in applications such as wireless sensor networks, where power and bandwidth are limited (ABOUTANIOS *et al.*, 2017).

6. Widely Applicable: DOA estimation is a widely applicable technique, making it invaluable in various industries and fields. It is used in areas such as defense, navigation, broadcast communication, healthcare, and transportation. This versatility makes DOA estimation an essential tool for researchers, engineers, and developers (DEY; ASHOUR, 2018).

Given its numerous advantages, we will employ DOA estimation in this work. We invite the reader to delve into the forthcoming chapter, where we present DOA estimation algorithms, exploring their intricacies and applications in greater detail.

# DOA ESTIMATION ALGORITHM

The DOA estimation is a crucial aspect in fields like radar systems and wireless communications, aiming to determine the angles from which signals arrive at a sensor array. Various algorithms are deployed for this critical task. beamformer scan aims to create a directive radiation pattern, aligning the array's sensitivity with the direction of interest while mitigating signals from other directions (KRIM; VIBERG, 1996). The MUSIC algorithm utilizes spectral analysis, offering a high resolution for the detection of closely spaced signals (SCHMIDT, 1986). Capon's Minimum Variance Distortionless Response (MVDR) (CAPON, 1969) focuses on minimizing output power while ensuring unity gain for the desired signal, making it effective in interference suppression.

Techniques such as beamforming, ESPRIT, and Bayesian approaches provide distinct perspectives, with adaptive beamformers excelling in interference handling, ESPRIT leveraging rotational invariance, and Bayesian methods presenting a probabilistic framework. Compressed sensing techniques exploit signal sparsity for accurate DOA estimation with fewer samples (ROY; KAILATH, 1989). The selection of an algorithm should consider aspects like application requirements and computational complexity, highlighting the continuous evolution of DOA estimation techniques to meet diverse real-world demands.

## 4.1 COVARIANCE MATRICES

Before delving into DOA estimation algorithms, it is crucial to acknowledge the real-world scenario where signals received by an array are typically contaminated by noise. In such contexts, the noises are commonly uncorrelated, whereas the pure signals captured by different elements tend to be correlated since they stem from the same sources. Leveraging this inherent property, one can effectively extract DOA information. This is achieved by exploiting

the concept of cross-covariance among the noise-corrupted signals, encapsulated in the spatial covariance matrix (SCHMIDT, 1986). This matrix, which incorporates both signals and noise, serves as a cornerstone in determining DOAs. The spatial covariance matrix of the data i.e., signals plus noises received by an array is defined as (FOUTZ *et al.*, 2022) (CHEN *et al.*, 2010):

$$\mathbf{R}_{xx} = E \{ \mathbf{x}(t) \mathbf{x}^H(t) \}, \quad (4.1)$$

where  $E \{ \cdot \}$  denotes the statistical expectation.

Eq. (4.1) quantifies the degree of correlation of the data signals received by array elements. The higher the values of its elements, the higher the degree of correlations among the signals. By substituting Eq. (2.33) with (4.1), we have (FOUTZ *et al.*, 2022) (CHEN *et al.*, 2010):

$$\mathbf{R}_{xx} = E \{ \mathbf{x}(t) \mathbf{x}^H(t) \} = \mathbf{A} \mathbf{R}_{ss} \mathbf{A}^H + \sigma_N^2 \mathbf{I}_M, \quad (4.2)$$

where  $\mathbf{R}_{ss} = E \{ \mathbf{s}(t) \mathbf{s}^H(t) \}$  is the signal covariance matrix and  $\sigma_N^2$  is the common variance of the noises.

In practical scenarios, finding the precise covariance matrix,  $\mathbf{R}_{xx}$ , is challenging due to the limited data sets processed by an array. Consequently, an estimation is employed. Assuming the ergodicity of all underlying random noise processes, we replace the ensemble average with a time average. In this context,  $L$  represents the number of snapshots, denoted by  $l = 1, 2, \dots, L$ . The matrix  $\mathbf{X}$  symbolizes the noise-corrupted signals or data, consisting of  $L$  snapshots of  $\mathbf{x}(t_l)$ , where  $1 \leq l \leq L$ .

$$\begin{aligned} \mathbf{X} &= [ \mathbf{x}(t_1) \quad \mathbf{x}(t_2) \quad \dots \quad \mathbf{x}(t_L) ]^T \\ &= \mathbf{A} [ \mathbf{s}(t_1) \quad \mathbf{s}(t_2) \quad \dots \quad \mathbf{s}(t_L) ]^T + [ \mathbf{w}(t_1) \quad \mathbf{w}(t_2) \quad \dots \quad \mathbf{w}(t_L) ]^T \\ &= \mathbf{A} \mathbf{S} + \mathbf{W}. \end{aligned} \quad (4.3)$$

Note that Eq. (4.3) is different from the basic data model Eq. (2.33) in that the left-hand side term,  $\mathbf{X}$ , is a stacked noised corrupted signal (or data) received by the array elements at different snapshots,  $\mathbf{x}(t_l), l = 1, 2, 3, \dots, L$ . Similarly, the stacking applies to the pure signal vector  $\mathbf{s}$  and the noise vector  $\mathbf{w}$ .

An estimate of the data covariance matrix  $\mathbf{R}_{xx}$  as a time average,  $\hat{\mathbf{R}}_{xx}$ , can then be computed

with:

$$\mathbf{R}_{xx} \approx \hat{\mathbf{R}}_{xx} = \frac{1}{L} \sum_{l=1}^L \mathbf{x}(t_l) \mathbf{x}^H(t_l) = \frac{1}{L} \mathbf{X}^H \mathbf{X}. \quad (4.4)$$

This matrix serves as the cornerstone in all subsequent explanations of DOA estimation algorithms. Numerous DOA estimation techniques aim to extract information from this array data covariance matrix. Armed with an understanding of data models and essential mathematical concepts, we proceed to explore some widely used DOA estimation techniques.

## 4.2 BEAMFORMER SCAN

The fundamental concept behind the Beamformer Scan method is to systematically direct the array towards a specific angle, measuring the resulting output power. When this directed angle aligns with the DOA of a signal, the system observes maximum output power (KRIM; VIBERG, 1996).

With knowledge of the array steering vector, electronic steering of the array becomes possible, akin to the mechanical steering of a fixed antenna. However, beyond changing orientation, the array pattern can also undergo shape variations. A weight vector, denoted as  $\boldsymbol{\nu}$ , can be crafted and subsequently used to linearly combine the data received by array elements, generating a singular output signal  $y(t)$  (SCHMIDT, 1986)(CHEN *et al.*, 2010),

$$y(t) = \boldsymbol{\nu}^H \mathbf{x}(t), \quad (4.5)$$

where the weighting vector  $\boldsymbol{\nu}$  is set as the following equation for a particular steering direction  $\theta_c$

$$\boldsymbol{\nu} = \frac{\mathbf{a}(\theta_c)}{M}. \quad (4.6)$$

Then the power of the output is calculated by

$$\begin{aligned}
P_{CBF}(\theta_c) &= \frac{1}{L} \sum_{t=1}^L |y(t)|^2 \\
&= \frac{1}{L} \sum_{t=1}^L \boldsymbol{\nu}^H \mathbf{x}(t) \mathbf{x}^H(t) \boldsymbol{\nu} \\
&= \frac{\mathbf{a}^H(\theta_c) \hat{\mathbf{R}}_{xx} \mathbf{a}(\theta_c)}{M^2}.
\end{aligned} \tag{4.7}$$

The DOA estimation performance of the beamformer scan method is depicted in Fig. 4.1. In this illustration, the method assumes the presence of two uncorrelated, far-field, and narrowband incoming signals impinging on a ULA with 10 sensor elements from directions  $10^\circ$ ,  $30^\circ$ . The chosen configuration includes 200 snapshots, and the SNR is set to 10 dB.

Two peaks are discernible in the DOA estimation plot at  $10^\circ$  and  $30^\circ$ , however, when two impinging angles are near, the resulting peaks may become blurred into a single pair. This suggests that the spread of each peak is substantial. These characteristics limit the method's effectiveness in scenarios where signals arrive from multiple directions and/or sources, resulting in poor resolution. Although enhancing resolution is possible by adding more array elements, it

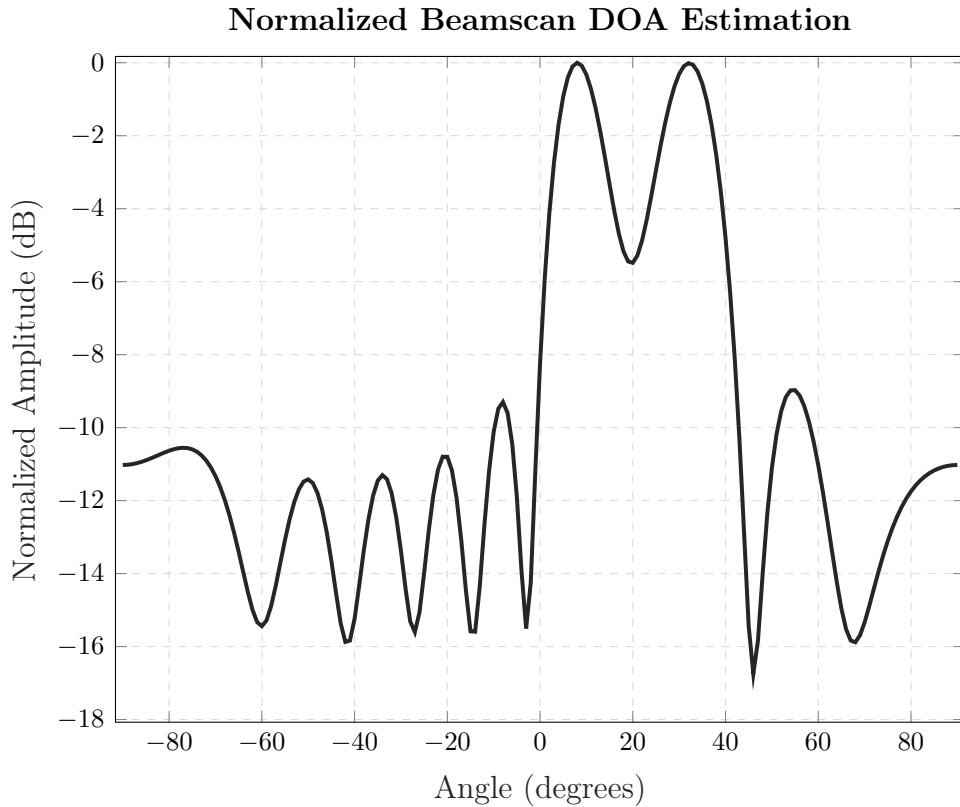


Figure 4.1: DOA estimation with the conventional beamformer; the signal impinges at  $10^\circ$  and  $30^\circ$ .

concurrently leads to an increase in the number of receivers and the amount of storage required for the data (CHEN *et al.*, 2010).

### 4.3 CAPON'S BEAMFORMER

The traditional beamformer operates under the assumption that directing the strongest beam toward a specific direction results in peak power arriving from that direction. It works effectively in the presence of a single incoming signal, utilizing all available degrees of freedom to form a beam in the desired direction. However, challenges arise in the presence of multiple signals, as the array output power includes contributions from both the desired and undesired angles (STOICA *et al.*, 2002).

Capon's method (CAPON, 1969) addresses this issue by leveraging the degrees of freedom to create a beam in the desired direction while simultaneously establishing nulls in other directions to reject unwanted signals. To achieve this, Capon's method strategically constrains the beam in the undesired directions, maintaining unity gain in the desired direction. This approach optimally utilizes all but one degree of freedom to minimize array output power, effectively enhancing performance in scenarios with multiple signals. The principle of the Capon method is to minimize the power contributed by the signals coming from other directions and noise than the current searching one  $\theta_c$  by:

$$\min_{\boldsymbol{\nu}} P(\boldsymbol{\nu}) \quad \text{subject to} \quad \boldsymbol{\nu}^H \mathbf{a}(\theta_c) = 1, \quad (4.8)$$

where  $P(\boldsymbol{\nu}) = \boldsymbol{\nu}^H \hat{\mathbf{R}}_{xx} \boldsymbol{\nu}$  (ZUO *et al.*, 2023).

The weight vector selected through this process is commonly known as the MVDR beamformer. This designation stems from its ability to minimize the variance (average power) of the array output signal for a specific look direction, ensuring distortion-free passage of the signal arriving from that direction. The resultant weight vector is expressed as (STOICA *et al.*, 2002) (CHEN *et al.*, 2010):

$$\boldsymbol{\nu} = \frac{\hat{\mathbf{R}}_{xx}^{-1} \mathbf{a}(\theta_c)}{\mathbf{a}^H(\theta_c) \hat{\mathbf{R}}_{xx}^{-1} \mathbf{a}(\theta_c)}. \quad (4.9)$$

Then the power of the output is given by:

$$P_{\text{Capon}}(\theta_c) = \frac{1}{\mathbf{a}^H(\theta_c) \hat{\mathbf{R}}_{xx}^{-1} \mathbf{a}(\theta_c)}. \quad (4.10)$$

The DOA estimation performance of Capon’s method is depicted in Fig. 4.2. The same simulation conditions as Fig. 4.1 are assumed.

In contrast to Fig. 4.1, the enhanced performance of Capon’s method is evident in the sharper and better-separated peaks at  $10^\circ$  and  $30^\circ$ , surpassing the conventional beamformer. The reduction of side lobes at other angles contributes to a clearer interpretation of output power. Despite its improved resolution over conventional beamforming, Capon’s method has drawbacks. It proves ineffective in the presence of correlated signals, as it unintentionally employs the singular correlation matrix  $\hat{\mathbf{R}}_{xx}^{-1}$  for such signals, leading to destructive combinations. Additionally, the computation of a matrix inverse, a requirement for Capon’s method, becomes costly for large arrays (CAPON, 1969).

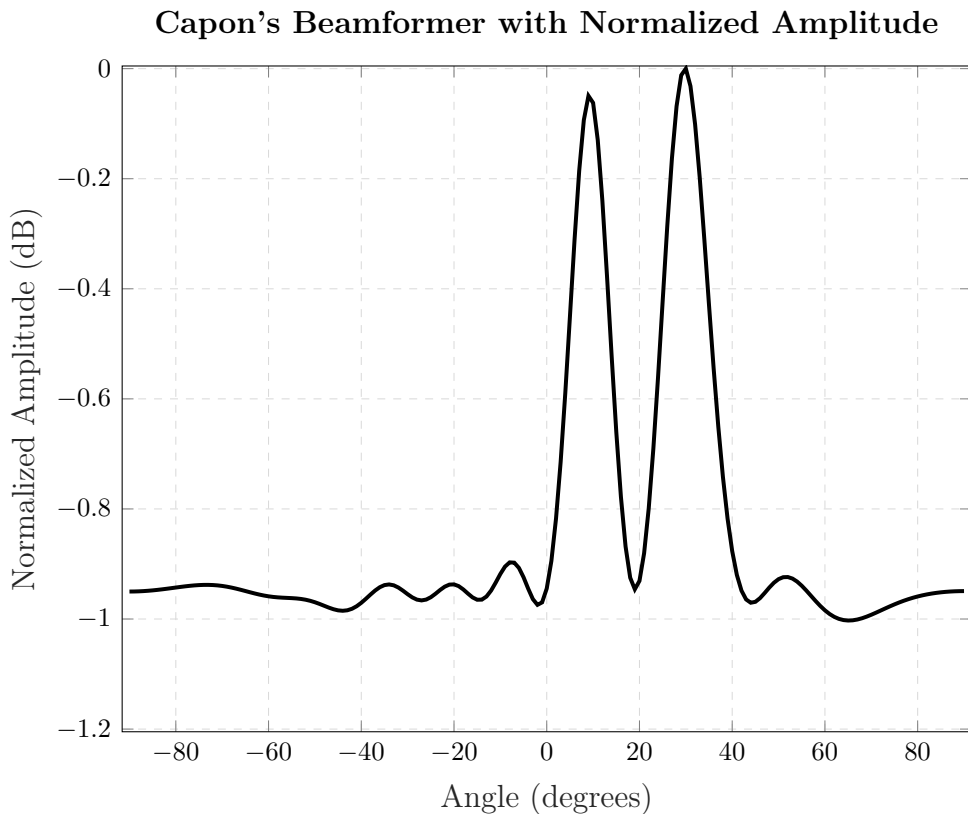


Figure 4.2: DOA estimation with Capon’s beamformer; the signal impinges at  $10^\circ$  and  $30^\circ$ .

### 4.3.1 Concept of Subspaces

To describe the next DOA estimation techniques, as MUSIC and ESPRIT, it is important to highlight the concept of subspace.

Given a matrix  $\mathbf{X}$  of size  $M \times N$ , the columns (rows) can be dependent or independent. If there are  $K$  independent columns in  $\mathbf{X}$ , forming a  $K$ -dimensional range or column space a subspace of  $M$ -dimensional Euclidean space  $\mathbb{C}^M$ , then the matrix is of rank  $K$ . If  $K = M$ , it is of full rank; otherwise, it is rank-deficient. Similarly,  $\mathbb{C}^N$  has a  $K$ -dimensional subspace as the row space of  $\mathbf{x}$  (CHEN *et al.*, 2010) (FOUTZ *et al.*, 2022).

Assume  $K \leq M$  and  $K \leq N$ , a unitary matrix  $\mathbf{U}$  can be selected such that the  $d$ -dimensional column space of  $\mathbf{X}$  is spanned by a subset of  $K$  columns of  $\mathbf{U}$  say, the first  $K$  columns, which together form a matrix  $\mathbf{U}_s$ . Let the remaining  $M_s - K$  columns together form a matrix  $\mathbf{U}_o$ . Then (CHEN *et al.*, 2010) (FOUTZ *et al.*, 2022),

$$\mathbf{U} = [ \mathbf{U}_s \quad \mathbf{U}_o ], \quad (4.11)$$

since  $\mathbf{U}$  is a unitary matrix, it can be observed that

1. From  $\mathbf{U}^H \mathbf{U} = \mathbf{I}_M$

$$\mathbf{U}_s^H \mathbf{U}_s = \mathbf{I}_K \quad (4.12)$$

$$\mathbf{U}_s^H \mathbf{U}_o = \mathbf{0} \quad (4.13)$$

$$\mathbf{U}_o^H \mathbf{U}_o = \mathbf{I}_{M-K}. \quad (4.14)$$

2. From  $\mathbf{U} \mathbf{U}^H = \mathbf{I}_M$

$$\mathbf{U}_s \mathbf{U}_s^H + \mathbf{U}_o \mathbf{U}_o^H = \mathbf{I}_M, \quad (4.15)$$

where  $\mathbf{I}_K$  is the identity matrix of rank  $K$ , and  $\mathbf{I}_{M-K}$  is the identity matrix of rank  $(M - K)$ .

The relationships (4.12) to (4.14) highlight the orthogonality and decomposition properties. These equations express that any vector  $\mathbf{u} \in \mathbb{C}^N$  can be decomposed into mutually orthogonal vectors  $\mathbf{u}_s$  and  $\mathbf{u}_o$  in  $K$ -dimensional and  $(M - K)$ -dimensional subspaces spanned by  $\mathbf{U}_s$  and  $\mathbf{U}_o$ , respectively. The direct sum of these subspaces forms  $\mathbb{C}^M$ . In signal processing, these

subspaces are identified as the signal subspace and the noise subspace, respectively. Singular value decomposition (SVD) is a method commonly used to perform such decompositions (CHEN *et al.*, 2010) (FOUTZ *et al.*, 2022).

#### 4.3.1.1 SVD

The SVD proves to be a robust computational method, providing high-resolution discrimination against noise space or contamination. For an  $M \times N$  matrix  $\mathbf{X}$  of rank  $K$ , the SVD yields the following decomposition (CHEN *et al.*, 2010) (FOUTZ *et al.*, 2022):

$$\mathbf{X} = \mathbf{U}\mathbf{\Sigma}\mathbf{V}^H = \begin{bmatrix} \mathbf{U}_s & \mathbf{U}_o \end{bmatrix} \begin{bmatrix} \mathbf{\Sigma}_s & \mathbf{0} \\ \mathbf{0} & \mathbf{\Sigma}_o \end{bmatrix} \begin{bmatrix} \mathbf{V}_s^H \\ \mathbf{V}_o^H \end{bmatrix}, \quad (4.16)$$

where  $\mathbf{\Sigma}$  is an  $M \times N$  diagonal matrix containing the singular values  $\Sigma_{si}$  of  $\mathbf{X}$ , ordered as  $\sigma_{s1} \geq \sigma_{s2} \geq \dots \geq \sigma_{sK} \geq \sigma_{sK+1} = \dots = 0$ .

Only the  $K$  largest singular values matter, corresponding to the nonzero singular values. The  $K$  columns of  $\mathbf{U}_s$  corresponding to these nonzero singular values span the column space of  $\mathbf{X}$  and are called left singular vectors. Similarly, the  $K$  rows of  $\mathbf{V}_o$  are called right singular vectors and span the row space of  $\mathbf{X}$ . An alternative decomposition is the eigenvalue decomposition of the data covariance matrix  $\mathbf{X}\mathbf{X}^H$ .

Subspace-based methods aim to find directions where the associated steering vectors are orthogonal to the noise subspace and lie within the signal subspace. These methods operate directly on the data matrix  $\mathbf{X}$  instead of  $\mathbf{X}\mathbf{X}^H$ , making them more effective in finite precision computations. These approaches facilitate the extraction of data model parameters once the signal subspace is determined, giving rise to various algorithms.

## 4.4 MULTIPLE SIGNAL CLASSIFICATION

MUSIC is one of the earliest proposed and a very popular method for super-resolution direction finding. The MUSIC algorithm operates on the fundamental principle of spectral analysis and demonstrates remarkable efficacy, particularly in scenarios involving correlated signals or when the number of sources exceeds the number of sensors in the array. This tech-

nique leverages the eigenvalues and eigenvectors of the sample covariance matrix to effectively decompose the signal subspace, enabling robust discrimination between signal and noise components (TANGSHENG *et al.*, 2012).

Considering the covariance matrix of received signals, denoted as  $\mathbf{R}_{xx}$  and described in (4.2), let the eigenvalues be  $\{\lambda_1, \dots, \lambda_M\}$ , satisfying (SCHMIDT, 1986) (CHEN *et al.*, 2010):

$$|\mathbf{R}_{xx} - \lambda_i \mathbf{I}_M| = 0. \quad (4.17)$$

Then, the substitution of Eq. (4.2) into Eq. (4.17) reads

$$|\mathbf{A}\mathbf{R}_{ss}\mathbf{A}^H + \sigma_N^2 \mathbf{I}_M - \lambda_i \mathbf{I}_M| = 0. \quad (4.18)$$

Assume that  $\mathbf{A}\mathbf{R}_{ss}\mathbf{A}^H$  has eigenvalues  $e_i$  then

$$e_i = \lambda_i - \sigma_N^2. \quad (4.19)$$

Given that  $\mathbf{A}$  consists of linearly independent steering vectors, it exhibits full column rank, and the signal correlation matrix  $\mathbf{R}_{ss}$  is nonsingular under low signal correlation conditions (SCHMIDT, 1986).

With a full column rank  $\mathbf{A}$  and a nonsingular  $\mathbf{R}_{ss}$ ,  $\mathbf{A}\mathbf{R}_{ss}\mathbf{A}^H$  becomes positive semidefinite with rank  $K$  when the number of incident signals  $K$  is less than the number of elements  $M$ . Consequently,  $M - K$  eigenvalues of  $\mathbf{R}_{xx}$  are equal to the noise variance  $\sigma_N^2$  and are the smallest. Thus, once the multiplicity  $d$  of the smallest eigenvalue is determined, the estimate of the number of signals,  $K$ , can be obtained accordingly with  $K = M - d$ .

The eigenvectors corresponding to eigenvalues  $\lambda_i$  for  $i = K + 1, K + 2, \dots, M$  are solutions to the equation (CHEN *et al.*, 2010):

$$(\mathbf{R}_{xx} - \lambda_i \mathbf{I}_M) \mathbf{q}_i = 0. \quad (4.20)$$

For these eigenvectors associated with the  $M - K$  smallest eigenvalues, we can express it as

$$\begin{aligned} (\mathbf{R}_{xx} - \sigma_i \mathbf{I}_M) \mathbf{q}_i &= \mathbf{A}\mathbf{R}_{ss}\mathbf{A}^H \mathbf{q}_i + \sigma_N^2 \mathbf{I}_M \mathbf{q}_i - \sigma_N^2 \mathbf{q}_i \\ &= \mathbf{A}\mathbf{R}_{ss}\mathbf{A}^H \mathbf{q}_i = 0. \end{aligned} \quad (4.21)$$

Since  $\mathbf{A}$  is full rank and  $\mathbf{R}_{ss}$  is nonsingular, it implies that

$$\mathbf{A}^H \mathbf{q}_i = \mathbf{0}. \quad (4.22)$$

This means the eigenvectors associated with the  $M - K$  smallest eigenvalues are orthogonal to the  $K$  steering vectors comprising  $\mathbf{A}$ ,  $\{\mathbf{a}(\theta_1), \dots, \mathbf{a}(\theta_K)\} \perp \{\mathbf{q}_{K+1}, \dots, \mathbf{q}_M\}$ .

This observation is fundamental to most subspace-based methods. It allows estimating the steering vectors associated with received signals by identifying vectors orthogonal to the  $M - K$  eigenvectors linked to eigenvalues of  $\mathbf{R}_{xx}$  approximately equal to  $\sigma_N^2$ . This analysis demonstrates that the eigenvectors of the covariance matrix  $\mathbf{R}_{xx}$  fall into either the principal eigensubspace (signal subspace) or the nonprincipal eigensubspace (noise subspace). Steering vectors corresponding to DOA lie in the signal subspace and are orthogonal to the noise subspace. By exploring array steering vectors to find those perpendicular to the space spanned by nonprincipal eigenvectors, the DOAs can be determined (LIBERTI; RAPPAPORT, 1999) (LITVA; LO, 1996).

To form the noise subspace, a matrix containing the noise eigenvectors need to be formed:

$$\mathbf{V}_n = [\mathbf{q}_{K+1}, \dots, \mathbf{q}_M]. \quad (4.23)$$

Since the steering vectors corresponding to signal components are orthogonal to the noise subspace eigenvectors,  $\mathbf{a}^H(\theta_c) \mathbf{V}_n \mathbf{V}_n^H \mathbf{a}(\theta_c) = 0$  for  $\theta_c = \theta_{ci}$  corresponding to the DOA of an incoming signal. Then the following MUSIC spectrum is constructed by taking the inverse of  $\mathbf{a}^H(\theta_{cc}) \mathbf{V}_n \mathbf{V}_n^H \mathbf{a}(\theta_c)$  (SCHMIDT, 1986)(CHEN *et al.*, 2010):

$$P(\theta_c) = P_{\text{MUSIC}}(\theta_c) = \frac{1}{\mathbf{a}^H(\theta_c) \mathbf{V}_n \mathbf{V}_n^H \mathbf{a}(\theta_c)}. \quad (4.24)$$

The DOAs of the multiple incident signals can be estimated by locating the peaks of the Eq. (4.24). The  $K$  largest peaks in the MUSIC spectrum above correspond to the DOAs of the signals impinging on the array. With the same simulation conditions introduced previously, the DOA estimation performance of the MUSIC method is shown in Fig. 4.3, which is significantly better than the beamforming-based methods.

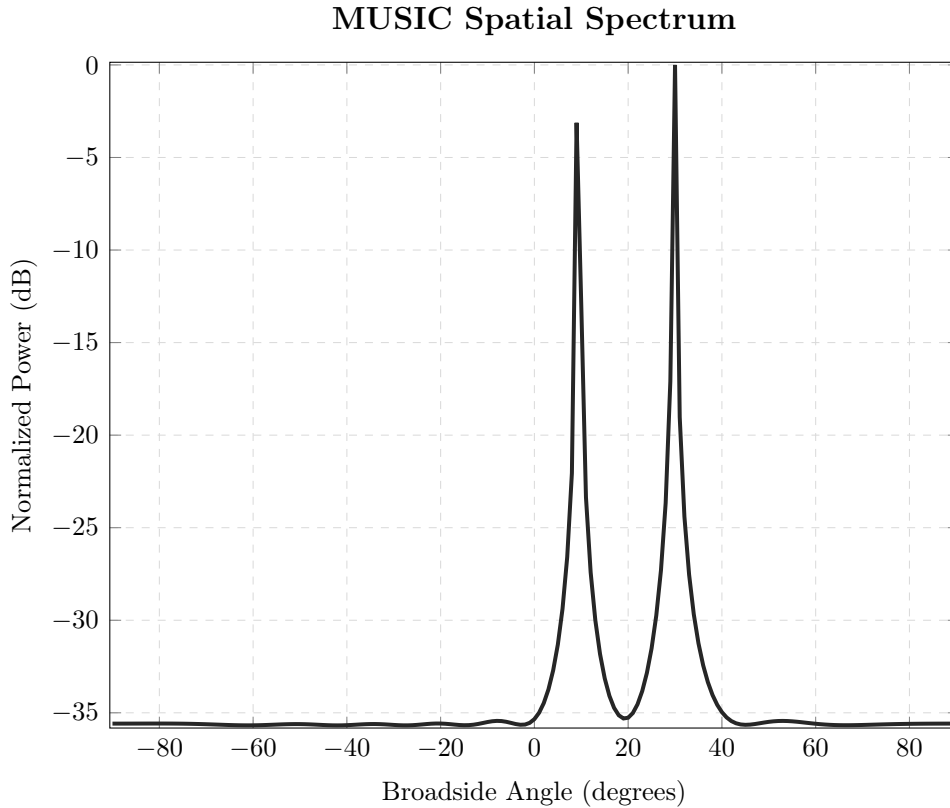


Figure 4.3: DOA estimation with MUSIC; the radio signals impinges at  $10^\circ$  and  $30^\circ$

In Fig. 4.3, a significantly sharper peak in angle estimation is evident, accompanied by nearly imperceptible side lobes. The MUSIC algorithm exhibits a notable advantage over Capon’s method and beamformer scan in scenarios with closely spaced sources. MUSIC excels in achieving higher resolution for distinguishing angles of arrival, particularly in cases where sources are correlated or the number of signals exceeds the number of sensors in the array. This capacity to effectively handle such challenging scenarios positions MUSIC as the preferred choice for high-resolution DOA estimation (TANGSHENG *et al.*, 2012).

#### 4.5 ESTIMATION OF SIGNAL PARAMETER VIA ROTATIONAL INVARIANCE

Developed as a subspace-based method, ESPRIT exploits the rotational invariance property of the array covariance matrix. The algorithm works by decomposing the received data into two subspaces: the signal subspace, containing information about the directions of arrival, and the noise subspace. By leveraging the eigenvalue decomposition of the covariance matrix, ESPRIT achieves a computationally efficient and high-resolution estimation of DOA. One notable feature

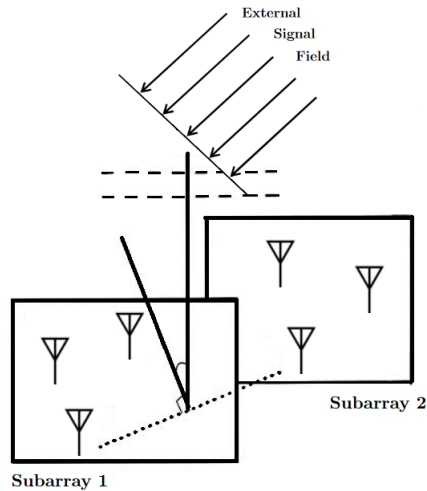


Figure 4.4: Antenna array structure for ESPRIT-based algorithms. (CHEN *et al.*, 2010).

is its ability to estimate DOA pairs accurately even in the presence of closely spaced signals.

The ESPRIT algorithm assumes that an antenna array is composed of two identical subarrays as shown in Fig. 4.4. The subarrays may overlap, that is, an array element may be a member of both subarrays. If there are a total of  $M$  elements in an array and  $m$  elements in each subarray, the overlap implies that  $M \leq 2m$ . For subarrays that do not overlap,  $M = 2m$  (ROY; KAILATH, 1989).

The subarrays' elements can exhibit diverse polarization, directional gain, and phase responses, as long as each has an identical counterpart in its companion subarray. Paired elements, or doublets, are assumed to be physically separated by a fixed displacement vector. This creates a displacement invariance in the array, where elements occur in matched pairs with identical displacement vectors. This property ensures rotational invariance in signal subspaces formed by the data vectors from spatially displaced subarrays. ESPRIT leverages this invariance to effectively determine DOAs (LAVATE *et al.*, 2010).

Assume  $k$  signals impinging onto the array. Let  $\mathbf{x}_1(t)$  and  $\mathbf{x}_2(t)$  represent the signals received by the two subarrays, each corrupted by additive noise  $\mathbf{w}_1(t)$  and  $\mathbf{w}_2(t)$ , respectively. Each subarray consists of  $m$  elements. As described in Eq. (2.33), the received signals can be expressed as (CHEN *et al.*, 2010) (FOUTZ *et al.*, 2022):

$$\mathbf{x}_1(t) = \mathbf{A}\mathbf{s}(t) + \mathbf{w}_1(t), \quad (4.25)$$

$$\mathbf{x}_2(t) = \mathbf{A}\Phi(t)\mathbf{s}(t) + \mathbf{w}_2(t). \quad (4.26)$$

where  $\mathbf{x}_1(t)$  and  $\mathbf{x}_2(t)$  are the  $m \times 1$  vectors representing the data received by the first and second subarrays, respectively. The  $\Phi = \text{diag} [e^{j\pi \sin \theta_1} \quad e^{j\pi \sin \theta_2} \quad \dots \quad e^{j\pi \sin \theta_K}]$  is a  $K \times K$  diagonal matrix that relates the signals received by the two subarrays and is called the rotation operator.

Equations (4.25) and (4.26) can be combined to form the total array output vector as:

$$\mathbf{x}(t) = \begin{bmatrix} \mathbf{x}_1(t) \\ \mathbf{x}_2(t) \end{bmatrix} = \begin{bmatrix} \mathbf{A} \\ \mathbf{A}\Phi \end{bmatrix} \mathbf{s}(t) + \begin{bmatrix} \mathbf{w}_1(t) \\ \mathbf{w}_2(t) \end{bmatrix} = \tilde{\mathbf{A}}\mathbf{s}(t) + \mathbf{w}(t). \quad (4.27)$$

Given  $L$  snapshots,  $\mathbf{x}(t_1), \mathbf{x}(t_2), \dots, \mathbf{x}(t_L)$ , the objective of the ESPRIT technique is to estimate the DOAs by determining  $\Phi = \text{diag} (e^{j\pi \sin \theta_1} \quad e^{j\pi \sin \theta_2} \quad \dots \quad e^{j\pi \sin \theta_K})$ . In doing so, two steps are required based on the data received by the array: estimating the signal subspace and then estimating the subspace rotation operator (HAARDT, 1996), (ROY; KAILATH, 1989) and (RAO; ARUN, 1992)

#### 4.5.1 Signal Subspace Estimation

In the case of  $K$  signals, the observed data vectors  $\mathbf{x}(t) = \mathbf{A}\mathbf{s}(t)$  are constrained to a  $K$ -dimensional signal subspace of  $\mathbb{C}^M$ , referred to as the signal subspace. The goal is to estimate this  $K$ -dimensional signal subspace.

Let  $\mathbf{E}_1$  and  $\mathbf{E}_2$  denote two sets of vectors that span the same signal subspace, ideally spanned by the columns of  $\mathbf{A}$ . The signal subspace can be obtained from the array output covariance matrix  $\mathbf{R}_{xx}$ . The data covariance matrix  $\mathbf{R}_{xx}$  takes the following form (CHEN *et al.*, 2010) (ROY; KAILATH, 1989):

$$\mathbf{R}_{xx} = E [\mathbf{x}(t)\mathbf{x}^H(t)] = \tilde{\mathbf{A}}\mathbf{R}_{ss}\tilde{\mathbf{A}}^H. \quad (4.28)$$

Both  $\mathbf{R}_s$  and the steering matrix  $\tilde{\mathbf{A}}$  are assumed to have a full rank  $K$ . Suppose that the signal subspace is spanned as  $\mathbf{E}_s = [\mathbf{e}_1, \dots, \mathbf{e}_d]$ . Since  $\mathbf{R}_s$  has a full rank,  $\mathbf{E}_s$  spans the same space as  $\tilde{\mathbf{A}}$ . As a result, there must exist a unique nonsingular matrix  $\mathbf{T}$  such that:

$$\mathbf{E}_s = \tilde{\mathbf{A}}\mathbf{T}, \quad (4.29)$$

$\mathbf{E}_s$  can be decomposed into  $\mathbf{E}_1$  and  $\mathbf{E}_2$  of the two subarrays such that:

$$\mathbf{E}_s = \begin{bmatrix} \mathbf{E}_1 \\ \mathbf{E}_2 \end{bmatrix} = \begin{bmatrix} \mathbf{A}\mathbf{T} \\ \mathbf{A}\Phi\mathbf{T} \end{bmatrix}, \quad (4.30)$$

from which it can be observed that:

$$\text{Range}\{\mathbf{E}_1\} = \text{Range}\{\mathbf{E}_2\} = \text{Range}\{\mathbf{A}\}. \quad (4.31)$$

Eq. (4.31) indicates that the two subarrays span the same signal subspace and have the same dimension; this is because they are identically configured. As a result, a nonsingular  $K \times K$  matrix denoted as  $\Psi$  can be found such that (YANG, 2020):

$$\mathbf{E}_1\Psi = \mathbf{E}_2 \Rightarrow \mathbf{A}\mathbf{T}\Psi = \mathbf{A}\Phi\mathbf{T} \quad (4.32)$$

and

$$\Psi = \mathbf{T}^{-1}\Phi\mathbf{T}. \quad (4.33)$$

Now,  $\Psi$  and  $\Phi$  are connected through an eigenvalue-preserving similarity transformation. The diagonal elements of  $\Phi$  correspond to the eigenvalues of  $\Psi$ , which rotates the  $m$ -dimensional signal subspace matrix  $\mathbf{E}_1$  associated with the first subarray to  $\mathbf{E}_2$  associated with the second subarray. This shift-invariance property is expressed in terms of signal eigenvectors that span the subspace.

In practical situations, only a finite number of noisy data are available. The matrix  $\mathbf{E}_s$  is estimated from the data matrix  $\mathbf{X}$  or covariance matrix  $\mathbf{R}_{xx} = E[\mathbf{x}(t)\mathbf{x}^H(t)] = \tilde{\mathbf{A}}\mathbf{R}_{ss}\tilde{\mathbf{A}}^H + \sigma_N^2\mathbf{I}_{2m}$ . Due to noise,  $\text{range}\{\mathbf{E}\} \neq \text{range}\{\tilde{\mathbf{A}}\}$  and  $\text{range}\{\mathbf{E}_1\} \neq \text{range}\{\mathbf{E}_2\}$ . Thus,  $\mathbf{E}_1\Psi = \mathbf{E}_2$  as in (4.32) cannot be solved exactly, necessitating an estimation approach for  $\Psi$ . Two common methods are Least-Squares (LS) (KARIYA; KURATA, 2004) and Total Least Square (TLS) (GOLUB; LOAN, 2013), leading to two versions of ESPRIT.

Considering (4.32) as a matrix model  $\mathbf{A}\mathbf{X} = \mathbf{B}$ , LS assumes matrix  $\mathbf{A}$  is known and attributes errors to noise in  $\mathbf{B}$ , giving the solution:

$$\hat{\mathbf{X}} = [\mathbf{A}\mathbf{A}^H]^{-1} \mathbf{A}^H \mathbf{B}, \quad (4.34)$$

where  $\hat{\mathbf{X}}$  is the estimate of  $\mathbf{X}$ . However,  $\mathbf{A}$  may also contain errors due to noise. Therefore, the TLS method is preferred, addressing noises in both  $\mathbf{A}$  and  $\mathbf{B}$ . TLS seeks residual matrices  $\mathbf{R}_A$  and  $\mathbf{R}_B$  of minimum Frobenius norm such that:

$$[\mathbf{A} + \mathbf{R}_A] \hat{\mathbf{X}} = \mathbf{B} + \mathbf{R}_B. \quad (4.35)$$

The computation procedure for TLS is detailed in various literatures, including (GOLUB; LOAN, 2013). Due to its robustness, we elaborated TLS in this study.

#### 4.5.1.1 Eigenvalues and Eigenvectors of Covariance Matrice

Without additive noise (i.e.,  $\sigma_N^2 = 0, \mathbf{R}_{xx}$ ),  $\mathbf{R}_{xx}$  would be rank deficient since (CHEN *et al.*, 2010)

$$\text{rank} \{ \mathbf{A}\mathbf{R}_{ss}\mathbf{A}^H \} = K < M. \quad (4.36)$$

In this case, its  $M - K$  smallest eigenvalues are equal to zero, and an eigenvalue decomposition of  $\mathbf{R}_{xx}$  can be expressed as:

$$\begin{aligned} \mathbf{R}_{xx}|_{\sigma_N^2=0} &= \sum_{d=1}^M \lambda_d \mathbf{u}_d \mathbf{u}_d^H \\ &= [\mathbf{U}_s \quad \mathbf{U}_o] \begin{bmatrix} \Lambda_K & \mathbf{0} \\ \mathbf{0} & \mathbf{0} \end{bmatrix} \begin{bmatrix} \mathbf{U}_s^H \\ \mathbf{U}_o^H \end{bmatrix} = \mathbf{U}_s \Lambda_K \mathbf{U}_s^H, \end{aligned} \quad (4.37)$$

where the diagonal matrix  $\Lambda_K = \text{diag}[\lambda_1, \lambda_2, \dots, \lambda_K]$  contains the nonzero eigenvalues. Here, the eigenvalues  $\lambda_d$  are ordered according to their magnitudes such that

$$\lambda_1 \geq \lambda_2 \geq \dots \geq \lambda_K \geq \lambda_{K+1} = \lambda_{K+2} = \dots = \lambda_M = 0. \quad (4.38)$$

The columns of

$$\mathbf{U}_s = [\mathbf{u}_1 \mathbf{u}_2 \dots \mathbf{u}_K] \quad \text{and} \quad \mathbf{U}_o = [\mathbf{u}_{K+1} \mathbf{u}_{K+2} \dots \mathbf{u}_M], \quad (4.39)$$

span the  $K$ -dimensional signal subspace  $S$  and its orthogonal complement is then called noise subspace (CHEN *et al.*, 2010). With additive noise, the eigendecomposition of the covariance matrix  $\mathbf{R}_{xx}$  in (4.2) gives

$$\begin{aligned} \mathbf{R}_{xx} &= \sum_{d=1}^M \rho_d \mathbf{u}_d \mathbf{u}_d^H \\ &= [\mathbf{U}_s \quad \mathbf{U}_o] \left( \begin{bmatrix} \boldsymbol{\Lambda}_K & \mathbf{0} \\ \mathbf{0} & \mathbf{0} \end{bmatrix} + \sigma_N^2 \mathbf{I}_M \right) \begin{bmatrix} \mathbf{U}_s^H \\ \mathbf{U}_o^H \end{bmatrix}. \end{aligned} \quad (4.40)$$

Obviously, from (4.37) and (4.40), the eigenvalues of  $\mathbf{R}_{xx}$  now become  $\rho_k = \lambda_k + \sigma_N^2$ ,  $1 \leq d \leq K$ ; they are shifted by  $\sigma_N^2$ , but their corresponding eigenvectors remain the same as those of (4.37). From (4.2) and (4.37), we can see that

$$\mathbf{R}_{xx}|_{\sigma_N^2=0} = \mathbf{A} \mathbf{R}_{ss} \mathbf{A}^H = \mathbf{U}_s \boldsymbol{\Lambda}_d \mathbf{U}_s^H. \quad (4.41)$$

From the above relation, it can be observed that the columns of the array steering matrix  $\mathbf{A}$  also span the  $K$ -dimensional signal subspace, that is,

$$S = \text{Range} \{\mathbf{A}\} = \text{Range} \{\mathbf{U}_s\}. \quad (4.42)$$

#### 4.5.1.2 Angle Estimation

There exists a nonsingular  $K \times K$  matrix  $\mathbf{T}_A$  such that  $\mathbf{A} = \mathbf{U}_s \mathbf{T}_A$ . Now, knowing that each row in the steering matrix  $\mathbf{A}$  corresponds to each element of the linear array, we choose a particular subarray configuration that can be made mathematically by applying a selection matrix to the overall steering matrix. Due to the shift-invariance property of all the  $K$  steering vectors, it can be expressed in a compact matrix form as (CHEN *et al.*, 2010) (YANG *et al.*, 2002):

$$\mathbf{J}_1 \mathbf{A} \boldsymbol{\Phi} = \mathbf{J}_2 \mathbf{A}, \quad (4.43)$$

where

$$\mathbf{J}_1 = \begin{bmatrix} 1 & 1 & \cdots & 1 \\ e^{j\pi \sin \theta_1} & e^{j\pi \sin \theta_2} & \cdots & e^{j\pi \sin \theta_K} \\ \vdots & \vdots & \ddots & \vdots \\ e^{j(M-2)\pi \sin \theta_1} & e^{j(M-2)\pi \sin \theta_2} & \cdots & e^{j(M-2)\pi \sin \theta_K} \end{bmatrix}, \quad (4.44)$$

$$\mathbf{J}_2 = \begin{bmatrix} e^{j\pi \sin \theta_1} & e^{j\pi \sin \theta_2} & \dots & e^{j\pi \sin \theta_K} \\ e^{j2\pi \sin \theta_1} & e^{j2\pi \sin \theta_2} & \dots & e^{j2\pi \sin \theta_K} \\ \vdots & \vdots & \ddots & \vdots \\ e^{j(M-1)\pi \sin \theta_1} & e^{j(M-1)\pi \sin \theta_2} & \dots & e^{j(M-1)\pi \sin \theta_K} \end{bmatrix}, \quad (4.45)$$

Hence, the shift-invariance property of (4.43) can be expressed in terms of the signal eigenvectors  $\mathbf{U}_s$  that span the signal subspace:

$$\mathbf{J}_1 \mathbf{U}_s \mathbf{T}_A \Phi = \mathbf{J}_2 \mathbf{U}_s \mathbf{T}_A \Leftrightarrow \mathbf{J}_1 \mathbf{U}_s \Psi = \mathbf{J}_2 \mathbf{U}_s. \quad (4.46)$$

After the estimation of the matrix  $\mathbf{U}_s$  that spans the estimated signal subspace, based on 4.46, the two known selection matrices  $\mathbf{J}_1$  and  $\mathbf{J}_2$  are applied to form the following invariance equation.

$$\mathbf{J}_1 \mathbf{U}_s \Psi \approx \mathbf{J}_2 \mathbf{U}_s \in \mathbb{C}^{m \times d}, \quad (4.47)$$

where  $\Psi$  is the signal subspace rotating operator, defined by (4.37). In contrast to (4.46), this invariance equation might not have an exact solution; this is because the signal subspace is estimated from an estimated data covariance matrix (4.16) that is not the true or exact signal covariance matrix. Also, the size of the subarrays  $M - 1$  should be at least equal to  $K$  in order to compute all the DOAs; otherwise, the invariance system 4.47 would be underdetermined.

Equation (4.47) is solved by using the LS or TLS solutions to get an estimate of the subspace rotating operator  $\Psi$  as explained in the previous section.

Once  $\Psi \in \mathbb{C}^{K \times K}$  is found, the desired DOA information can be estimated from it. The eigenvalues of the estimated  $\Psi \in \mathbb{C}^{K \times K}$  can be calculated by its eigendecomposition; this is because

$$\Psi = \mathbf{T} \Phi \mathbf{T}^{-1} \text{ where } \Phi = \text{diag} [1 e^{j\pi \sin \theta_1} e^{j\pi \sin \theta_2} \dots e^{j\pi \sin \theta_K}]. \quad (4.48)$$

Therefore, after the eigenvalue decomposition of  $\Psi$ , for ULA the DOAs can be obtained by (ROY; KAILATH, 1989):

$$\theta_c = \arcsin \left( \frac{\text{angle}(\Phi(k, k))}{\pi} \right). \quad (4.49)$$

Without the spectrum, the DOA estimation performance of the ESPRIT method is shown in Fig. 4.5 with the same simulation conditions introduced above.

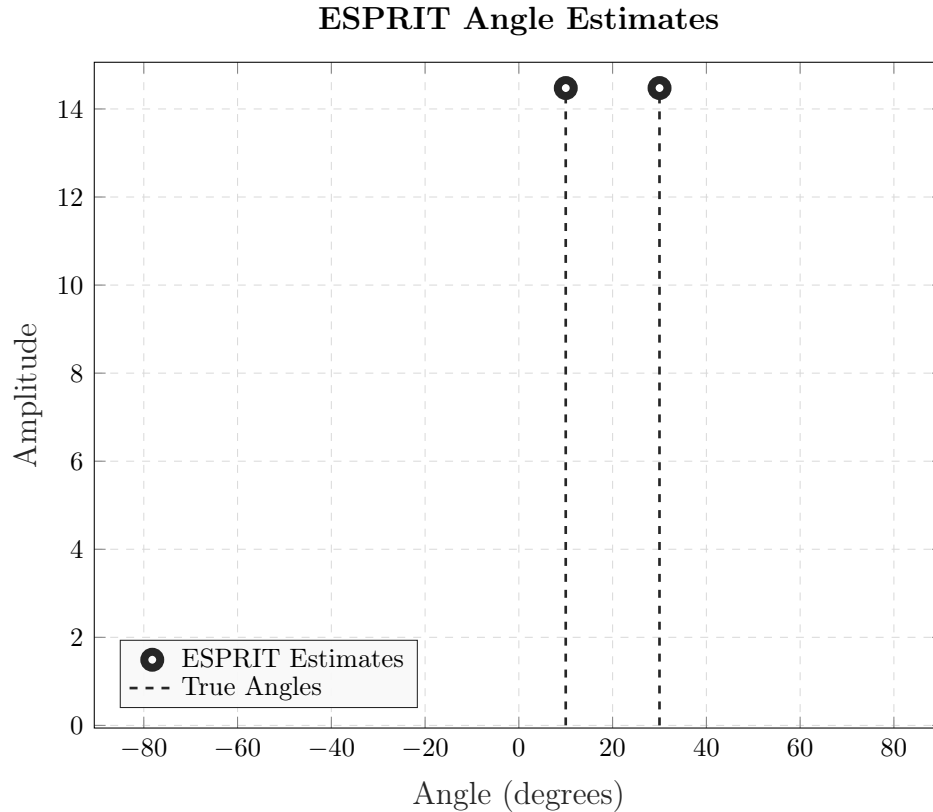


Figure 4.5: DOA estimation by ESPRIT method; the radio signals impinges at  $10^\circ$  and  $30^\circ$ .

The efficacy of ESPRIT relative to other DOA estimation techniques depends on the particular requirements and attributes of the application. It is worth highlighting that the ESPRIT presents advantages such as high angular resolution, especially in scenarios with closely spaced signals, and computational efficiency achieved through its subspace methods. Notably, ESPRIT demonstrates robustness in the presence of correlated signals, often outperforming methods that are sensitive to signal correlation in such scenarios. This robustness is a significant strength, contributing to the versatility of ESPRIT in various practical applications (CHEN *et al.*, 2010).

The DOA estimation algorithms discussed thus far have focused exclusively on the far-field region. In the upcoming chapter, we delve into the intricacies and obstacles the near field poses. We propose an approach that combines sub-array division and far-field techniques to overcome the challenges inherent in near-field scenarios. This approach enables us to employ generalized far-field DOA estimation algorithms like ESPRIT for accurate bearing estimation in near-field conditions.

# FUNDAMENTALS OF NEAR-FIELD LOCALIZATION

In the realm of mobile communication, there has been a notable emphasis on studying source localization in the far-field rather than the near-field of antenna arrays. This trend can be attributed to several key factors. Firstly, the far-field region is often considered more practical for mobile communication systems due to its clearer propagation characteristics and adherence to classical electromagnetic wave theory (JINGJING *et al.*, 2021). In this chapter, we first present the differences between far-field and near-field communications and the challenges for near-field localization. Subsequently, we delve deeper into developing the system model used in this study.

## 5.1 FAR-FIELD COMMUNICATIONS VS. NEAR-FIELD COMMUNICATIONS

In the context of the near-field antenna arrays, we are dealing with relatively short distances between the signal source and the antenna array. In this case, the near-field electric field dominates propagation, as mentioned in Section 2.1.2. This can result in significant diffraction and reflection effects, as well as challenges such as electromagnetic coupling between antennas in the array. Thus, spherical wavefront characteristics play a crucial role in the near-field region, which is typically within a few wavelengths of the antenna. Unlike in the far-field where the wavefront becomes planar and predictable, Another important factor is that due to reciprocity, in the far-field, the amplitude of the electric field is constant over the receive antenna and the phase variation only depends on the incident angle, not the distance, unlike the near-field (HUANG; BARKAT, 1991), (CUI *et al.*, 2022).

### 5.1.1 Spherical Wavefront Delay-and-Sum

A widely accepted metric for delineating between far-field and near-field regions is the Rayleigh distance, also known as the Fraunhofer distance, represented by  $R_F = 2D^2/\lambda$ , which typically marks the beginning of the far-field region, as discussed in Section 2.1.2. This distance is derived from analyzing the phase difference caused by the wave's curvature from its center to the edge. Consequently, eliminating the far-field assumption, as illustrated in Fig. 5.1, involves modeling the wavefront originating from a point source as a spherical surface centered at that source (LIU *et al.*, 2023). This spherical wavefront intersects the elements of the phased array, leading to relative time delays determined by the hyperbolic range across collinear elements, as illustrated in Fig. 5.2. This figure demonstrates the variation in element delays and wavefront shape between a steered beam with and without focusing, with element delays being relative to the array center.

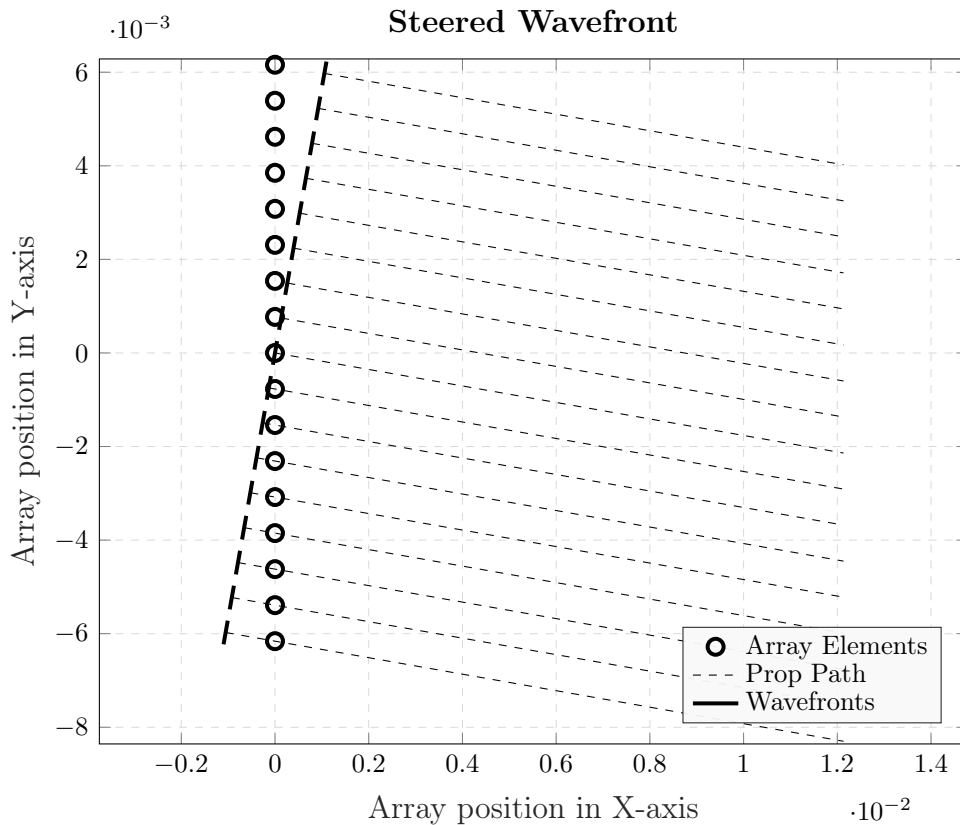


Figure 5.1: Difference in element delays and wavefront shape between a steered beam without focusing, simulated by a 17-element ULA at an operational frequency of 3GHz.

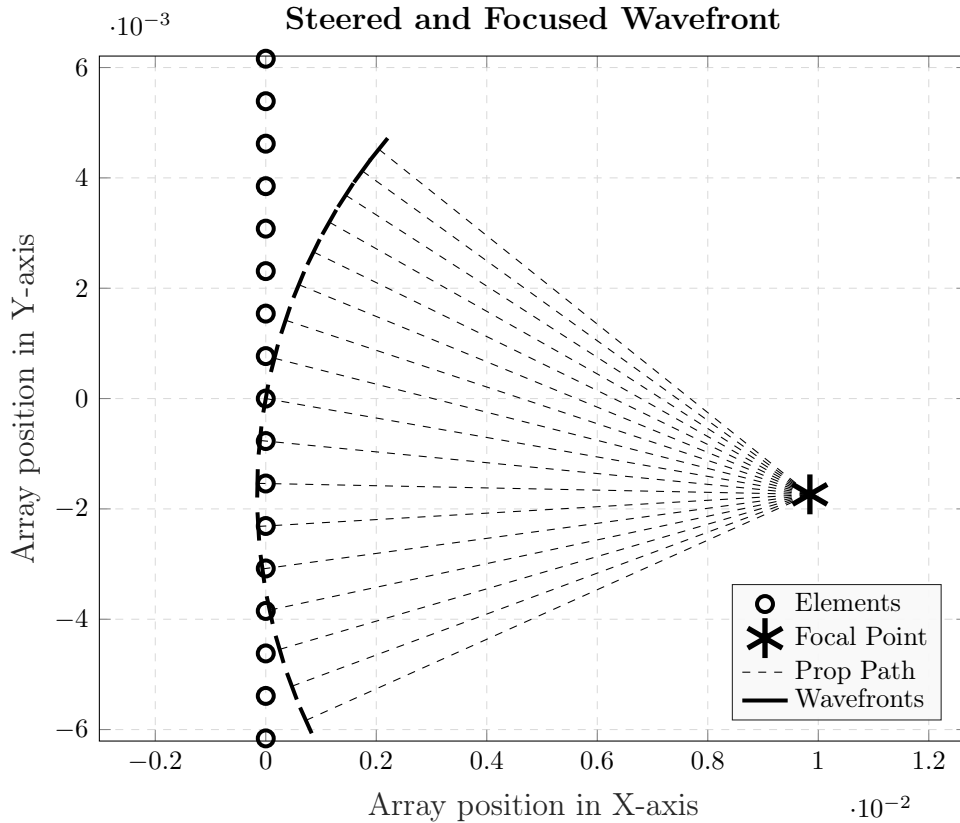


Figure 5.2: Difference in element delays and wavefront shape between a steered beam without focusing, simulated by a 17-element ULA at an operational frequency of 3GHz.

As the spherical wavefront approaches a receiver or encounters a surface, the points closer to the center of the wavefront reach the receiver or surface earlier than the points located toward the edge of the wavefront. This is because the points near the center have a shorter path length to travel compared to the points at the edge, which have to traverse a longer distance along the curved surface of the wavefront (BJÖRNSON *et al.*, 2021).

If the center is positioned at the Fraunhofer distance  $R = R_F$ , then  $R'$  in Fig. 5.3 is given by  $R' = \sqrt{R_F^2 + (D/2)^2}$ . Consequently, the phase difference can be expressed as:

$$\frac{2\pi}{\lambda} \left( \sqrt{R_F^2 + \frac{D^2}{4}} - R_F \right) \approx \frac{2\pi}{\lambda} \frac{D^2}{8R_F} = \frac{\pi}{8}, \quad (5.1)$$

which is negligible when analyzing antenna patterns. We utilized the Taylor approximation  $\sqrt{1+x} \approx 1 + \frac{x}{2}$  for  $x = D^2/4R_F^2$  in Eq. (5.1). The approximation error is smaller than  $3.5 \times 10^{-3}$  if  $R_F \geq 1.2D$ , which imposes an additional lower limit on the far-field region (SHERMAN, 1962). This limit represents an angular difference between the center and edge of at most  $\pi/8$ , leading to a negligible amplitude difference  $d/d' \geq 1.2D/\sqrt{(1.2D)^2 + D^2/4} \approx$

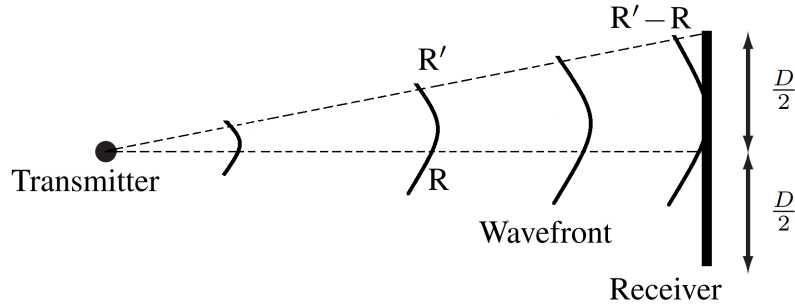


Figure 5.3: Antenna array structure for ESPRIT-based algorithms. Adapted by (BJÖRNSON *et al.*, 2021).

$\cos(\pi/8) \approx 0.92$ . The range of propagation distances between  $1.2D$  and  $d_F$  is called the Fresnel region and is characterized by the fact that the amplitude variations can be neglected, but not the phase variations. The Fresnel region only exists if  $d_F \geq 1.2D$ , which implies  $D \geq 0.6\lambda$ , thus the Fraunhofer distance is only applicable to electrically large antennas (BJÖRNSON *et al.*, 2021).

The difference in electromagnetic propagation characteristics leads to distinct beamforming properties in the near-field and far-field regions. In the far-field, beamforming resembles a divergent flashlight effect, as depicted in Fig. 5.4, known as beamsteering. Here, planar wavefronts steer beam energy towards specific angles across varying distances. However, this concise linear phase fails to fully capture spherical wave information (CUI *et al.*, 2022).

Conversely, in the near-field, beamforming resembles a concentrated spotlight, as shown in Fig. 5.4, termed beamfocusing. Here, the phase of spherical waves must be accurately derived based on physical geometry, a non-linear function of the antenna index. This phase encodes incident angle and distance information for each path between the BS and UE (CUI *et al.*, 2022), (LIU *et al.*, 2023).

Near-field beamforming achieves precise energy focusing at specific locations by leveraging the additional distance information within spherical wavefronts. This capability extends to both angle and distance domains, enabling targeted energy concentration in both dimensions (LIU *et al.*, 2023).

For precise user localization in the near-field, one cannot simply overlook the impact of spherical wavefronts on the communication system. Unlike the location of sources in the far-field in which only the angle estimation is necessary, for the far-field region it is necessary to

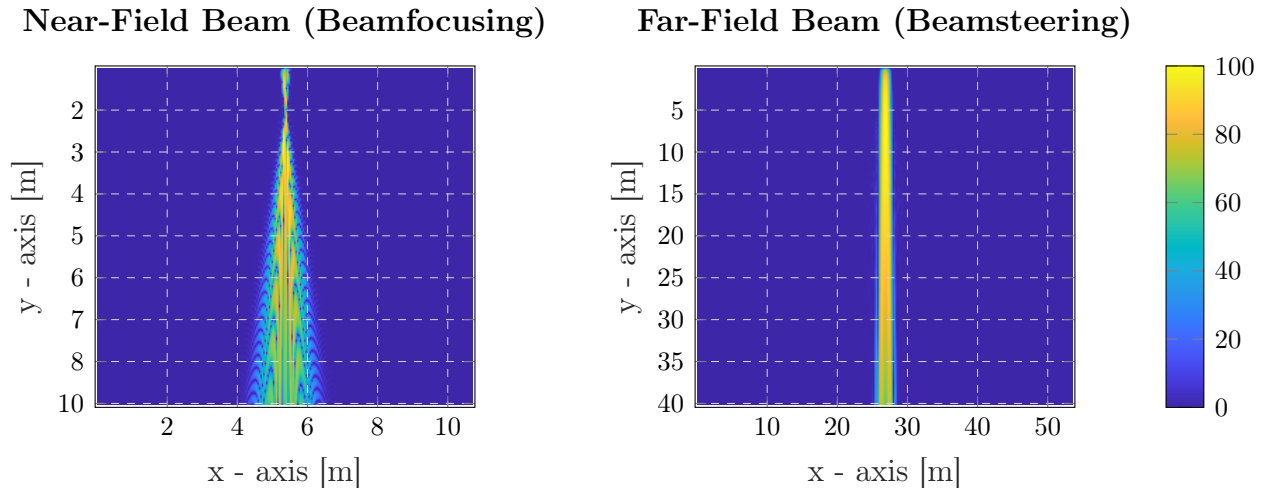


Figure 5.4: Comparison of Far-Field Planar Wavefronts and Near-Field Spherical Wavefronts: FFC beamsteering resembles a ‘flashlight’ emitting light with a plane wavefront, while NFC beamfocusing is akin to a ‘spotlight’ emitting light with a spherical wavefront. The corresponding radiation patterns, simulated for a narrowband system with 512 antennas operating at 3 GHz, are depicted on the right

estimate the angle and also the distance, that is, it is a problem involving 2D search. This study introduces an approach to tackle the nonlinearity from spherical wavefronts and simplify the search process from 2D to 1D. Our method, a second-order statistics-based 1D algorithm with symmetric subarray partition based in (ZHI; CHIA, 2007), efficiently localizes multiple near-field sources. Unlike conventional methods, our algorithm doesn’t require high-order statistics computation, parameter pairing, or multidimensional search. By dividing the array into symmetric subarrays, the steering vectors of the corresponding subarrays yield the far-field-like rotational invariance property in the signal subspace. We capitalize on this property to partition the problem into multiple smaller arrays, each of which is responsible for estimating its azimuth and elevation.

## 5.2 SYMMETRIC SUBARRAY PARTITIONING

This section delves into the concept of subarrays, a key element discussed throughout this work. To introduce this topic, we analyze a simplified near-field scenario involving  $K$  uncorrelated narrowband signals. These signals are directed towards a  $(2M + 1)$ -element ULA with an interelement spacing of  $d$ . Let the array center be the phase reference point. The received

signal, as previously described in Eq. (2.28), but now in near-field at the  $m$ -th sensor can be modeled as: (HE *et al.*, 2008):

$$\mathbf{x}_{NF}(t) = \sum_{k=1}^K e^{j\tau_{m,k}} s_k(t) + \mathbf{w}(t), \quad m = -M, \dots, M, \quad (5.2)$$

where  $s_k(t)$  is the  $k$  th source signal,  $\mathbf{w}(t)$  is the additive noise, and  $\tau_{m,k}$  is the phase shift associated with the propagation time delay between sensor 0 and sensor  $m$  of the  $k$  th source signal, which is a function of source signal parameters, range  $r_k$ , angle  $\theta_k$  and wavelength  $\lambda$ , given by:

$$\tau_{m,k} = \frac{2\pi}{\lambda} \left( \sqrt{r_k^2 + (md)^2} - 2r_k m d \sin \theta_k - r_k \right). \quad (5.3)$$

When the source  $k$  is in the Fresnel region, which is defined by  $r_k$  locating in the range,  $0.62(D^3/\lambda)^{1/2} < r_k < 2D^2/\lambda$ , with  $D$  representing the aperture of the array, as previously described in 5.1.1, the delay  $\tau_{m,k}$  can be approximated by using the second-order Taylor expansion:

$$\tau_{m,k} = \left( -\frac{2\pi d}{\lambda} \sin \theta_k \right) m + \left( \frac{\pi d^2}{\lambda r_k} \cos^2 \theta_k \right) m^2 + O\left(\frac{d^2}{r_k^2}\right), \quad (5.4)$$

where  $O(d^2/r_k^2)$  denotes terms of order greater than or equal to  $d^2/r_k^2$ .

Using this approximation, the signal in (5.2) can be reduced to:

$$\mathbf{x}_{NF}(t) = \sum_{k=1}^K e^{j\left(-\frac{2\pi d}{\lambda} \sin \theta_k\right)m + j\left(\frac{\pi d^2}{\lambda r_k} \cos^2 \theta_k\right)m^2} s_k(t) + \mathbf{w}(t). \quad (5.5)$$

Considering  $(2M + 1)$ -element ULA, the received signal vector  $\mathbf{x}_{NF}(t) = [\mathbf{x}_{-M}(t), \dots, \mathbf{x}_M(t)]^T$ , can be written in

$$\mathbf{x}_{NF}(t) = \mathbf{A}\mathbf{s}(t) + \mathbf{w}(t), \quad (5.6)$$

where  $\mathbf{s}(t) = [s_1(t), \dots, s_K(t)]^T$  is the signal vector,  $\mathbf{w} = [\mathbf{w}_{-M}(t), \dots, \mathbf{w}_M(t)]^T$  is the noise vector, and  $\mathbf{A}$  is the array manifold matrix in near-fiel given by:

$$\mathbf{A} = [\mathbf{a}(r_1, \theta_1), \dots, \mathbf{a}(r_K, \theta_K)] \quad (5.7)$$

with the steering vector  $\mathbf{a}(r_k, \theta_k)$  being expressed as:

$$\begin{aligned}
\mathbf{a}(r_k, \theta_k) &= \begin{bmatrix} a_{k,-M} \\ \vdots \\ a_{k,M} \end{bmatrix} \\
&= \begin{bmatrix} e^{j\left(\frac{2\pi d}{\lambda} \sin \theta_k\right)M + j\left(\frac{\pi d^2}{\lambda r_k} \cos^2 \theta_k\right)M^2} \\ \vdots \\ e^{-j\left(\frac{2\pi d}{\lambda} \sin \theta_k\right)M + j\left(\frac{\pi d^2}{\lambda r_k} \cos^2 \theta_k\right)M^2} \end{bmatrix}.
\end{aligned} \tag{5.8}$$

### 5.2.1 Signal Model for Symmetric Subarrays

Observing that the elements in Eq. (5.7) are symmetric with respect to the second term, we divide the ULA into two subarrays as shown in Fig. 5.5.

The first subarray is formed with the first  $N$  sensors in ascending order from sensor  $-M$  to sensor  $-M + N - 1$ , and the second subarray is formed with the last  $N$  sensors in descending order from sensor  $M$  to sensor  $M - N + 1$ . The received signal vectors of the two subarrays can be written as (ZHI; CHIA, 2007):

$$\mathbf{x}_{n1}(t) = [x_{-M}(t), x_{-M+1}(t), \dots, x_{-M+(N-1)}(t)]^T \tag{5.9}$$

and

$$\mathbf{x}_{n2}(t) = [x_M(t), x_{M-1}(t), \dots, x_{M-(N-1)}(t)]^T \tag{5.10}$$

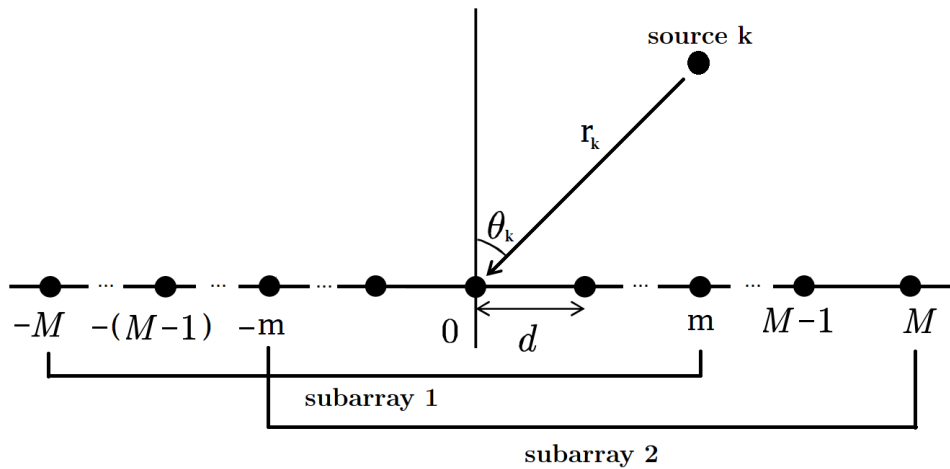


Figure 5.5: Near-field ULA configuration with symmetric partition. Adapted from (ZHI; CHIA, 2007)

where  $K < N < 2M + 1$ . These two subarray vectors have a similar form:

$$\mathbf{x}_{n1}(t) = \mathbf{A}_1 \mathbf{s}(t) + \mathbf{w}_1(t), \quad (5.11)$$

and

$$\mathbf{x}_{n2}(t) = \mathbf{A}_2 \mathbf{s}(t) + \mathbf{w}_2(t), \quad (5.12)$$

where  $\mathbf{w}_1(t) = [w_{-M}, w_{-M+1}(t), \dots, w_{-M+(N-1)}]^T$  and  $\mathbf{w}_2(t) = [w_M, w_{M-1}(t), \dots, w_{M-(N-1)}]^T$  are subarray noise vectors. The matrix  $\mathbf{A}_1$  is the first  $N$  rows of  $\mathbf{A}$  and  $\mathbf{A}_2$  is constructed with the last  $N$  rows of  $\mathbf{A}$  in reverse order. The relationship between  $\mathbf{A}$  and  $\mathbf{A}_1, \mathbf{A}_2$  is:

$$\mathbf{A} = \begin{bmatrix} \mathbf{A}_1 \\ \text{last}(M-N) \text{ rows} \end{bmatrix} = \begin{bmatrix} \text{first}(M-N) \text{ rows} \\ \mathbf{J}\mathbf{A}_2 \end{bmatrix}, \quad (5.13)$$

where  $\mathbf{J}$  is the anti-identity matrix satisfying  $\mathbf{J}^2 = \mathbf{I}$ . Define  $\mathbf{A}_1$  as:

$$\mathbf{A}_1 = [\mathbf{a}_1(r_1, \theta_1), \dots, \mathbf{a}_1(r_K, \theta_K)] \quad (5.14)$$

with

$$\mathbf{a}_1(r_k, \theta_k) = \begin{bmatrix} a_{k,-M} \\ \vdots \\ a_{k,-M+N-1} \end{bmatrix}. \quad (5.15)$$

The symmetric property gives

$$\mathbf{A}_2 = [\mathbf{D}(\theta_1) \mathbf{a}_1(r_1, \theta_1), \dots, \mathbf{D}(\theta_K) \mathbf{a}_1(r_K, \theta_K)], \quad (5.16)$$

where

$$\mathbf{D}(\theta_k) = \text{diag} \left[ e^{-j \left( \frac{4\pi d}{\lambda} \sin \theta_k \right) M}, \dots, e^{-j \left( \frac{4\pi d}{\lambda} \sin \theta_k \right) (M-N+1)} \right] \quad (5.17)$$

which is only related with the angle  $\theta_k$ .

### 5.2.1.1 Eigen-Decomposition of the Array Output

As described in Eq. (4.41) of Section 4.5.1.1, the eigendecomposition of the array covariance matrix  $\mathbf{R}_{xx} = \text{E} [\mathbf{x}(t)\mathbf{x}^H(t)]$  is given by  $\mathbf{R}_{xx} = \mathbf{U}_s \mathbf{\Lambda}_s \mathbf{U}_s^H + \mathbf{U}_n \mathbf{\Lambda}_n \mathbf{U}_n^H$ . Here,  $\mathbf{U}_s \in \mathbb{C}^{(2M+1) \times K}$  contains  $K$  eigenvectors spanning the signal subspace of  $\mathbf{R}_{xx}$ , with  $\mathbf{\Lambda}_s \in \mathbb{C}^{K \times K}$  representing the corresponding eigenvalues. Similarly,  $\mathbf{U}_n \in \mathbb{C}^{(2M+1) \times (2M+1-K)}$  contains  $2M+1-K$  eigenvectors

in the noise subspace of  $\mathbf{R}_{xx}$ , and  $\Lambda_n \in \mathbb{C}^{(2M+1-K) \times (2M+1-K)}$  is the diagonal matrix comprising the corresponding eigenvalues.

Simplifying the problem to 1D search and distributing it across multiple smaller arrays enables us to employ far-field algorithms for estimating azimuth and elevation. This approach leverages the benefits of far-field techniques while addressing the complexities associated with near-field scenarios, ultimately improving the accuracy and efficiency of the estimation process. In the following chapter, we will introduce a more robust and realistic near-field scenario. Additionally, we will outline an approach that utilizes the subarrays division discussed earlier to estimate both angle and range accurately.

## 2D SOURCE LOCATION IN NEAR-FIELD

2D source localization in the near-field region is substantiated by estimating the range and azimuth angle. It holds immense significance in various fields such as wireless communication, radar systems, and IoT applications.

The localization approach presented in this chapter leverages the intrinsic properties of ULAs, such as their directional sensitivity and spatial arrangement, to achieve precise 2D source localization, i.e DOA and range. Our methodology builds upon recent advancements in adaptive algorithms tailored for ELAA systems. Specifically, we employ the PAST algorithm (YANG, 1995), renowned for its efficiency and robustness in subspace tracking tasks.

### 6.1 SIGNAL MODEL

In the context of near-field considerations, the representation of the ULA shown in Fig. 2.6 in Section 2.3.2.1 has been modified to the depiction illustrated in Fig. 6.1. Here, we assume that the Base Station (BS) is located near a single-antenna User Equipment (UE) whose position is unknown and denoted by  $\mathbf{x} = [x, y]^T$ . The BS is equipped with an  $M$ -element linear antenna array, with a spacing of  $d$  between each element. The phase reference point is situated at the array center, and the array elements locations are represented as  $\mathbf{x}_m = [md, 0]^T$ , where  $m \in \{-M/2, \dots, M/2 - 1\}$ .

The UE transmits to the BS an Frequency Division Multiplexing (OFDM) signal with a power of  $P_t$  and a total bandwidth of  $W_b = K\Delta_f$ . Here,  $\Delta_f$  represents the spacing of the subcarrier and  $K$  is the number of subcarriers. Due to a discrepancy in local oscillators, the UE has a known clock bias, denoted  $B$ .

Let  $r_m = |\mathbf{x} - \mathbf{x}_m|$  represent the distance between the UE and the  $m$ -th sensor. For convenience, let  $k \in \{-K/2, \dots, K/2 - 1\}$  denote the index of the  $k$ -th subcarrier. The signal

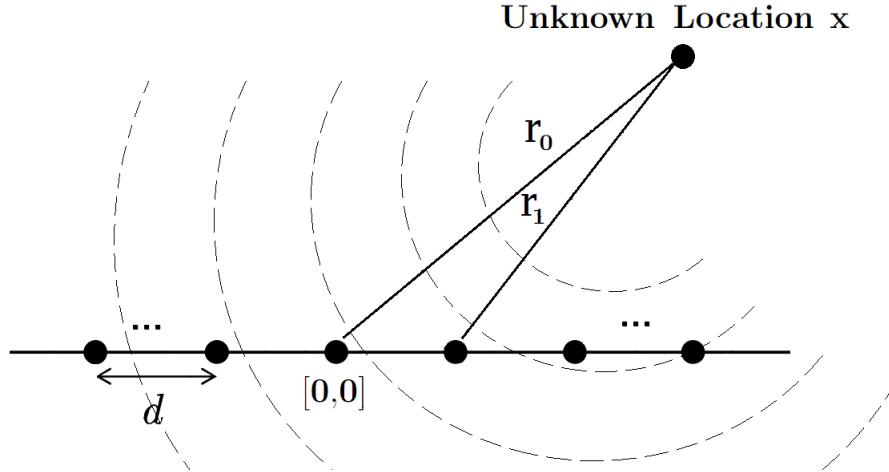


Figure 6.1: In a near-field scenario with a transmitting source and a receiver array, the phase across antenna elements changes nonlinearly, while in a spatial wide-band setting, the delay across elements varies significantly (ZHI; CHIA, 2007).

received by the  $m$ -th sensor can be expressed as follows, according to (ZHI; CHIA, 2007):

$$y_m[k] = \sum_{l=0}^L \alpha_{m,l}s[k]e^{-j\frac{2\pi}{\lambda}\epsilon_{m,l}[k]} + w_m[k] \quad (6.1)$$

where  $s[k]$  is the pilot symbol allocated to the  $k$ -th subcarrier and  $\alpha_{m,l}$  represents the complex channel gain at antenna  $m$  with respect to the  $l$ -th path, and  $L$  is the number of paths. The channel gain is characterized by  $\alpha_{m,l} = \rho_{m,l}e^{j\psi_{m,l}}$ , where  $\rho_{m,l} = \lambda/(2\pi r_{m,l})$  and  $\psi_{m,l}$  is a uniformly distributed random phase within the interval  $[0,2\pi]$ . If  $l = 0$ , the parameter is associated with the LOS component; otherwise, for  $l > 1$ , the parameters are associated with the NLOS components. The term  $w_m[k]$  denotes complex zero-mean Gaussian noise with a variance of  $N_0/2$ .

Considering the array center as the phase reference point  $\mathbf{x}_{0,0}$  and the center subcarrier  $k = 0$ , the phase  $\epsilon_{m,l}[k]$  at any antenna  $m$  and any subcarrier  $k$  can be expressed as (WYMEERSCH, 2020):

$$\epsilon_{m,l}[k] = (r_{m,l} - r_{0,l}) + k\frac{\tau_m}{KT_s f_c}, \quad (6.2)$$

where  $T_s = 1/W_b$ . The first term,  $r_m - r_0$ , represents the difference in path length concerning the center antenna. The second term,  $k\frac{\tau_m}{KT_s f_c}$ , depends on the absolute delay  $\tau_m$  and increases with the subcarrier index.

In Chapter 5, Section 5.1.1 elaborates on the difference in distances for linear arrays, given by  $r_m - r_0 = \sqrt{r_0^2 + m^2 d^2 - 2r_0 m d \cos(\theta)} - r_0$ . This expression can be approximated as  $r_m - r_0 \approx -d \cos \theta$  by employing a Taylor expansion centered around  $z = md/r_0 = 0$ .

We operate in the near-field regime when the distance between antennas falls within the range of  $0.62\sqrt{D^3/\lambda} < \|\mathbf{x}\| < 2D^2/\lambda$ , where the curvature of the electromagnetic wave becomes significant. This condition is detailed in Chapter 2, Section 2.1.2. Furthermore, we consider narrow-band operation valid when  $D \ll c/W_b$ , signifying that the signal delay between antennas is indistinguishable (CHEN *et al.*, 2002).

Under these assumptions, the phase, as described in (HUANG; BARKAT, 1991), can be expressed as:

$$\epsilon_{m,l}[k] = r_{m,l} + (kf_t - 1)r_{0,l} - kf_t B, \quad (6.3)$$

where  $f_t = \Delta_f/f_c$  and  $B$  is a certain bias due to discrepancy between local oscillators. We can generalise the signal model of Eq. ((6.1)) to the matrix model:

$$\mathbf{Y} = \sum_{l=0}^L \mathbf{A}_l \mathbf{V}_{:,l} \mathbf{F}_{:,l}^H \mathbf{S} + \mathbf{W}, \quad (6.4)$$

where  $\mathbf{Y} \in \mathbb{C}^{M \times K}$ ,  $\mathbf{V} \in \mathbb{C}^{M \times L}$  contains the array response to each path, so the  $(m,l)$ -th element is  $\mathbf{V}_{m,l} = e^{-j\frac{2\pi}{\lambda}(r_{m,l} - r_{0,l})}$ ,  $\mathbf{S} = \text{diag}(s_0, \dots, s_{K-1})$ ,  $r_{m,l}$  is the distance between the  $m$ -th antenna element and the point scatterer. For  $l = 0$ ,  $r_{m,0}$  is the distance between the  $m$ -th antenna and the user. The  $L \times L$  diagonal matrix  $\mathbf{A}_l = \text{diag}(\alpha_{0,l}, \alpha_{1,l}, \dots, \alpha_{M,l})$ . The matrix  $\mathbf{F} \in \mathbb{C}^{K \times L}$ , and its  $(k,l)$ -th element is  $\mathbf{F}_{k,l} = e^{j\frac{2\pi}{\lambda}((kf_t - 1)r_{0,l})}$ .

## 6.2 NEAR-FIELD USER POSITION ESTIMATION

Our approach involves ELAA comprising  $N$  subarrays for DOA and range estimation as described in Chapter 5 in Section 5.2.1. Initially, we leverage these subarrays to estimate their individual DOAs. These estimated DOAs are then used to trace lines originating from each subarray. The intersection point of these lines corresponds to the position of interest.

We partition the rows of  $\mathbf{Y}$  in Eq. (6.4) into non-overlapping subarrays, each containing  $N$  elements. From the near-field border  $\|\mathbf{x}\| < 2(Md)^2/\lambda$ , we establish an expected distance  $\bar{d}$ ,

which consists of the maximum range that we expect to find a user equipment and use near-field maximum distance to obtain

$$N \leq \sqrt{d\lambda}/(2d^2). \quad (6.5)$$

The subarray  $n$  corresponds to the observations at antennas  $(n-1)N$  through  $nN$ , with array center  $\tilde{\mathbf{x}}_n = \mathbf{x}_{M/2} + [d((n)N + N/2, 0)]^T$ . In this case, the indexing for  $n$  starts at 1. The total number of subarray is  $M$ , assuming  $M$  is divider by  $N$ .

Each subarray collects its signal from its respective antenna subarray to process them and extract the subspace. The received signal at the  $n$ th subarray is defined as  $\mathbf{Y}_n \in \mathbb{C}^{N \times K}$ . For subspace estimation, we first remove the pilot contribution by performing the following operation:

$$\hat{\mathbf{Y}}_n = \mathbf{Y}_n \mathbf{S}^H (\mathbf{S} \mathbf{S}^H)^{-1}. \quad (6.6)$$

Once the pilot is removed, the signal is processed by the adaptive algorithm of subspace estimation. After that, we can use the rotational invariance of the subspace to extract the angle. The method is detailed in the subsequent subsection.

### 6.2.1 DOA Estimation

Leveraging the rotational invariance inherent to each subarray, we employ the PAST algorithm to estimate their respective subspaces. Once convergence is reached, this algorithm is consistently extended to successive subarrays, utilizing computations grounded in the final subspace estimate derived from the preceding subarray, designated as  $n-1$ .

#### 6.2.1.1 PAST Estimation

The PAST estimation is a widely utilized method in signal processing and adaptive filtering due to its efficiency and robustness. PAST belongs to the family of subspace tracking algorithms and is particularly well-suited for tracking changes in the subspace of a signal or system over time. One of the key advantages of PAST is its computational efficiency. Unlike some other subspace tracking algorithms that require expensive matrix inversions or eigenvalue decompositions, PAST employs a recursive update formula that significantly reduces computational

complexity (SERGIO; DINIZ, 2002).

Moreover, PAST exhibits robustness in tracking time-varying subspaces, making it suitable for applications where the underlying signal or system dynamics change over time (VASEGHI, 2000). This adaptability is crucial in scenarios where accurate and real-time tracking of subspace variations is essential for system performance. In summary, the PAST algorithm, initially proposed by Slock et al. (CHAN *et al.*, 2006), offers a computationally efficient and robust solution for tracking time-varying subspaces, making it valuable in array processing.

In his work (YANG, 1995), Yang introduced the PAST algorithm designed for tracking principal components. The PAST estimation consists of an interpretation of the signal subspace as the solution of a projection-like unconstrained minimization problem, which is solved using Recursive Least-Squares (RLS) approaches by appropriately approximating the projection. The dominant subspace estimation consists in minimizing the approximated scalar cost function  $J(\mathbf{U}_n)$ , also known as the linear Principal Component Analysis criterion:

$$J(\mathbf{U}_n(k)) = \mathbf{E} \left\{ \left\| \hat{\mathbf{Y}}_n - \mathbf{U}_n \mathbf{U}_n^H \hat{\mathbf{Y}}_n \right\|^2 \right\}, \quad (6.7)$$

with the argument  $\mathbf{U}_n(k) \in \mathbb{C}^{N \times \gamma}$  ( $\gamma < N$ ) and  $\gamma$  being the rank represents the argument and  $\hat{\mathbf{Y}}_n$  denotes the data vector, that in our case is the signal described in Eq. (6.6). The error surface of this function exhibits several local minima and a single global minimum. At a local minimum, it is characterized by  $\mathbf{U}_n = \hat{\mathbf{U}}_n \mathbf{Q}$ , where  $\hat{\mathbf{U}}_n$  contains any subset of eigenvectors from  $\mathbf{C} = \mathbf{E}\{\hat{\mathbf{Y}}_n \hat{\mathbf{Y}}_n^H\}$  in  $\hat{\mathbf{U}}_n$ . The matrix  $\mathbf{Q} \in \mathbb{C}^{\gamma \times \gamma}$  is an arbitrary unitary matrix. When the cost function  $J(\mathbf{U}_n)$  reaches its lowest possible value,  $\hat{\mathbf{U}}_n$  will not consist of any eigenvectors, but rather the  $\gamma$  most significant ones (YANG, 1995).

We employ the well-established RLS algorithm to minimize the cost function  $J(\mathbf{U}_n)$ . This can be achieved by reformulating the cost function as follows:

$$J'(\mathbf{U}_n(k)) = \sum_{i=1}^k \beta^{k-i} \left| \hat{\mathbf{Y}}_n(i) - \mathbf{U}_n(k) \mathbf{U}_n^H(k) \hat{\mathbf{Y}}_n(i) \right|^2. \quad (6.8)$$

In this case, an exponentially weighted sum with the forgetting factor  $\beta$  replaces the expectation operator. When the forgetting factor is set to 1, all samples receive equal weight, ensuring that the previous data are not forgotten. By adjusting the forgetting factor to a value between 0 and 1,  $0 < \beta < 1$ , the resulting algorithm can be used to track nonstationary changes in the

sources, as outlined in (LANDQVIST; MOHAMMED, 2005).

We can modify the cost function in Eq. (6.8) by approximating  $\mathbf{U}^H \hat{\mathbf{Y}}_n(i)$  as  $\mathbf{U}^H(i-1) \hat{\mathbf{Y}}_n(i)$ . This approximation results in an alternative cost function:

$$J''(\mathbf{U}(k)) = \sum_{i=1}^k \beta^{k-i} \left\| \hat{\mathbf{Y}}_n(i) - \mathbf{U}_n(k) \mathbf{U}_n^H(i-1) \hat{\mathbf{Y}}_n(i) \right\|^2. \quad (6.9)$$

By defining  $\hat{\mathbf{Y}}'_n(i) = \mathbf{U}_n^H(i-1) \hat{\mathbf{Y}}_n(i)$ , we can further simplify the expression as follows:

$$J''(\mathbf{U}_n(k)) = \sum_{i=1}^k \beta^{k-i} \left\| \hat{\mathbf{Y}}_n(i) - \mathbf{U}_n(k) \hat{\mathbf{Y}}'_n(i) \right\|^2. \quad (6.10)$$

Similar to the cost function of the RLS method, this cost function is quadratic. The only distinction is that here an error vector  $\mathbf{e}(k)$  is needed instead of an error scalar  $e(k)$ . We conclude that we may approximately minimize the original cost function  $J(\mathbf{U}_n)$  by using RLS with the input signal  $\hat{\mathbf{Y}}'_n(k) = \mathbf{U}_n^H(k-1) \hat{\mathbf{Y}}_n(k)$  and the desired signal  $\hat{\mathbf{Y}}_n$ . Consequently, the PAST algorithm may be summarized in the Algorithm 1 (LANDQVIST; MOHAMMED, 2005). The variables  $\mathbf{h}(k)$  and  $\mathbf{g}(k)$  are utilized in the equations to calculate the RLS in between steps.

---

**Algorithm 1** The PAST algorithm for tracking the signal subspace

---

If  $m = 1$ : Initialize  $\mathbf{P}(0)$  and  $\mathbf{U}(0)$  randomly and appropriately. If  $m > 1$ : Initialize using the estimates from the  $(m-1)$ -th subarray.

**for**  $k = 1, 2, \dots$  **do**

$$\hat{\mathbf{Y}}'_n(k) = \mathbf{U}^H(k-1) \hat{\mathbf{Y}}_n(k)$$

$$\mathbf{h}(k) = \mathbf{P}(k-1) \hat{\mathbf{Y}}'_n(k)$$

$$\mathbf{g}(k) = \mathbf{h}(k) / \left[ \beta + \left( \hat{\mathbf{Y}}'_n(k) \right)^H \mathbf{h}(k) \right]$$

$$\mathbf{P}(k) = \beta^{-1} \text{tri} \left\{ \mathbf{P}(k-1) - \mathbf{g}(k) \mathbf{h}^H(k) \right\}$$

$$\mathbf{e}(k) = \hat{\mathbf{Y}}_n - \mathbf{U}(k-1) \hat{\mathbf{Y}}'_n(k)$$

$$\mathbf{U}_n(k) = \mathbf{U}_n(k-1) + \mathbf{e}(k) \mathbf{g}^H(k)$$

**end for**

---

To ensure that the matrix  $\mathbf{P}(k) \approx \mathbf{C}^{-1}(k)$  is symmetric, we use the notation  $\text{tri}\{\cdot\}$  to indicate that only the upper triangular portion of the argument is calculated, and its transpose is replicated to the lower triangular part. As a result, the algorithm avoids the need for any matrix inversions, with the most complex operation being scalar division (YANG, 1995).

It is essential to understand that the converged  $\mathbf{U}_n$  does not directly contain the eigenvectors of the correlation matrix. The reason behind this is that the cost function, once minimized, does not lead to a unique solution. In other words, there could be multiple  $\mathbf{U}_n$  matrices that minimize the cost function, and they might not necessarily correspond to the eigenvectors of the correlation matrix. Nonetheless, the product  $\mathbf{U}_n \mathbf{U}_n^H$  is unique, and it represents the signal subspace projection matrix.

The columns of the matrix  $\mathbf{U}_n$  that minimize the cost function  $J(\mathbf{U}_n)$  form an orthonormal basis for the signal subspace generated by the dominant eigenvalues  $\gamma$  of the correlation matrix. This orthonormal basis is crucial for identifying the directions of received signals, or DOA.

To estimate the DOA, we take the most representative column of  $\mathbf{U}_n$ , corresponding to this matrix's first column. This column is then rewritten in the form of two vectors,  $\mathbf{u}_1 = [e^{-j\omega_0}, \dots, e^{-j\omega(N-2)}]$  and  $\mathbf{u}_2 = [e^{-j\omega_1}, \dots, e^{-j\omega(N-1)}]$ , containing complex exponents related to the spatial frequencies of the received signals.

The steering vector for a linear array is given by  $\omega_i = 2\pi \frac{d}{\lambda} i \cos \theta$ . The difference between consecutive spatial frequencies,  $\omega_i - \omega_{i-1}$ , is proportional to the cosine of the angle of arrival  $\theta$ . This relationship allows us to estimate the angle  $\hat{\theta}_n$  of a subarray as:

$$\hat{\theta}_n = \cos^{-1} \left( \frac{\lambda}{2\pi Nd} \sum_{i=0}^{N-1} \arg(\text{diag}[\mathbf{u}_1^*] \mathbf{u}_2)_i \right), \quad (6.11)$$

where  $\arg(\text{diag}[\mathbf{u}_1^*] \mathbf{u}_2)$  yields a vector containing the arguments of the complex number entries of the vector  $\text{diag}[\mathbf{u}_1^*] \mathbf{u}_2$ .

### 6.2.2 Range Estimation

Two critical parameters are required to determine a UE's location: the signal's angle of arrival and the distance between the user and the antenna. Having presented a method for estimating the angle, we utilize this parameter to express a line originating from two subarrays mathematically. We then calculate the intersection point of the subarray lines, following a similar approach as presented in (ZHI; CHIA, 2007) and (WYMEERSCH, 2020).

Line intersections occur when two or more lines converge at a shared point. In this context,

we consider the lines as the distances we aim to determine, and the common point represents the UE with coordinates  $\mathbf{x} = [x,y]^T$  (BOLDRINI *et al.*, 1980). Considering the estimate angles and distance values across subarrays, our emphasis is on the angle and distance of both the initial and final subarrays. This enables us to represent the coordinates as follows:

$$\mathbf{x} = \frac{\tilde{x}_A \cdot \tan(\hat{\theta}_A) - \tilde{x}_B \cdot \tan(\hat{\theta}_B)}{\tan(\hat{\theta}_A) - \tan(\hat{\theta}_B)} \quad (6.12)$$

$$y = x \cdot \tan(\hat{\theta}_A) - \tilde{x}_A \cdot \tan(\hat{\theta}_B), \quad (6.13)$$

where,  $\tilde{x}_A$  represents the center of first subarray,  $\tilde{x}_B$  denotes the center of last subarray,  $\hat{\theta}_A$  refers to the angle estimated by PAST for first subarray, and  $\hat{\theta}_B$  corresponds to the angle estimated by PAST for last subarray. Incorporating both the angle and range estimation methods, we summarize the proposed user location Algorithm 2 for subarray localization.

---

**Algorithm 2** Subarray Localization

---

Assume the number of antennas per subarray as in Eq. (6.5).

Select two subarrays to trace the lines. Choose the first and the last ones.

**for**  $n = \{1, N\}$  **do**

    Collect  $\mathbf{Y}_n$ .

    Verify the most recent estimate of  $\mathbf{U}_n$ .

    Obtain  $\mathbf{U}_n$  using the PAST Algorithm 1. If no previous estimate of  $\mathbf{U}_n$  exists for other subarrays, initialize as a zero matrix.

    Estimate  $\hat{\theta}_n$  using Eq. (6.11).

    Calculate the center of the subarray:  $\tilde{x}_n = x_{M/2} + [d((n)N + N/2, 0)]^T$ .

**end for**

Calculate  $x$  and  $y$  using Eq. (6.12) and Eq. (6.13).

Determine the UE position as  $\mathbf{x} = [x,y]^T$ .

---

It is essential to highlight that the range estimation, which relies on the curvature of the electromagnetic wave, is not influenced by the bias  $B$ . This stands in contrast to the use of pilots spread across the frequency domain for delay estimation. Furthermore, it is possible to combine both techniques to estimate the bias  $B$  more effectively.

### 6.3 SIMULATION AND NUMERICAL RESULTS

We consider a scenario at a carrier  $f_c$  of 28 GHz ( $\lambda \approx 1.07$  cm), a bandwidth  $W$  of 100 MHz,  $c = 0.3$  m/ns  $N_0 = 4.0049 \times 10^{-9}$  mW/GHz, a transmit power  $P_t$  of 1 mW (with  $E\{|s[k]|\}^2 = P_t/W$ ) and  $K = 256$  subcarriers with QPSK pilots. The UE has bias  $B = 20$  m. The array has  $N = 128$  elements spaced at  $\lambda/2$ , corresponding to a total size of 69.11 cm and a far-field distance of 89 m. To test the performance of the algorithm, 500 Monte Carlo simulations are performed.

To validate the effectiveness of the method proposed in this work, including a PAST with SVD-based initialization of the first subarray, we conduct a comparative analysis. We contrast the RMSE and CDF curves with established techniques from the literature, 2D-IFFT (WYMEERSCH, 2020) and ESPRIT (ZHI; CHIA, 2007). All estimators employ the subarray approach and are tested in a multipath propagation setting that includes both LOS and NLOS components. We change  $d$  with random values of  $\theta \sim \mathcal{U}(\pi/4, 3\pi/4)$  and evenly distribute a scatterer with a radar cross-section of  $10 \text{ m}^2$  in the plane, this corresponds to a large scattering object and the forgetting factor  $\beta$  in Algorithm 1 is set to 0.97 (YANG, 1995).

The performance of each estimation method, in terms of position RMSE, as a function of the distance between the UE and the BS, is depicted in Figure 7.7. Besides estimation models, the Position Error Bound (PEB) is also presented in the figure. The PEB represents the minimum error attainable when the position is measured by an unbiased estimator (JOURDAN

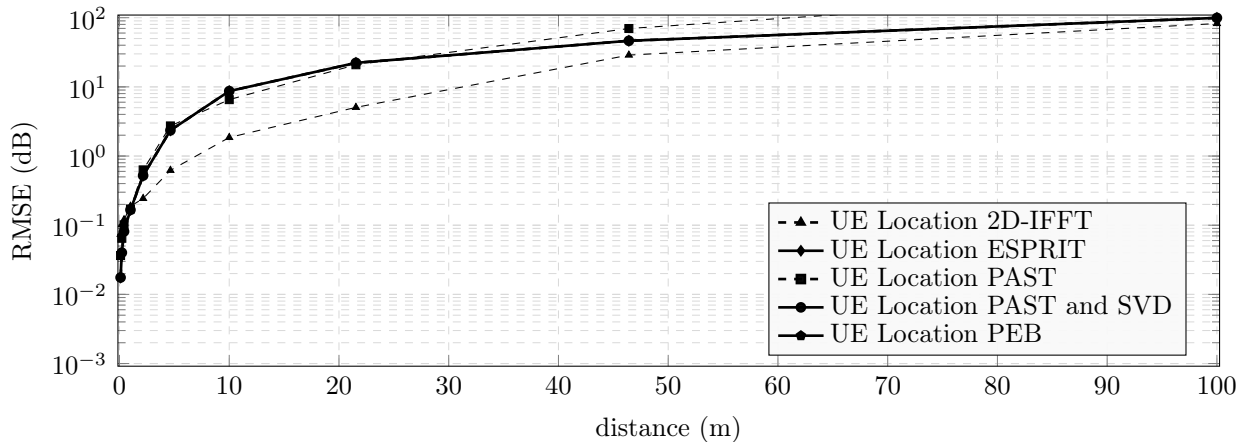


Figure 6.2: RMSE curve of the method proposed in this paper PAST, an enhanced variant PAST and SVD, 2D-IFFT (ZHI; CHIA, 2007) and ESPRIT (WYMEERSCH, 2020) with respect the user distance.

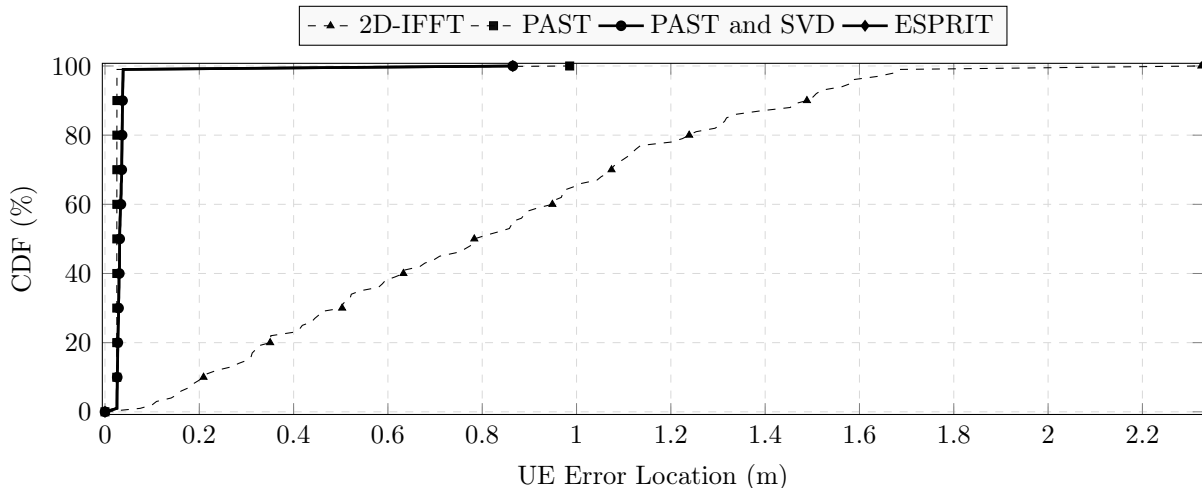


Figure 6.3: Comparison of empirical CDFs between estimators,  $\|x\| = 3,5$  m.

*et al.*, 2006). We observe that the PAST-based estimation exhibits lower position errors than ESPRIT and 2D-IFFT for distances closer to the BS (ranging from 0.1 m to 1 m). This can be attributed to the fact that PAST is an iterative search algorithm that projects data onto a lower-dimensional subspace, refining the DOA estimates with each iteration. However, beyond 1 m of distance, the PAST estimation’s RMSE increases compared to the 2D-IFFT DOA estimation. This may occur as the FFT beams approach the far-field beams of each subarray, which impacts the estimation performance.

The model operates in the near-field regime only when  $0.62\sqrt{(Md)^3/\lambda} < \|\mathbf{x}\| < 2(Md)^2/\lambda$  (between 3.4 m and 89 m). Although the 2D-IFFT DOA estimation demonstrates the best performance in terms of RMSE within the near-field distance compared to other methods, its precision is limited. This limitation is evident in Figure 6.3 and Figure 6.4, where the CDF curves indicate a higher variance for the estimator compared to the subspace-based methods. We examined estimators’ behavior within the near-field region by assessing two distances in this simulation: 3.5 meters proximal to the array, and 25 meters, distant from the array, both confined within the near-field range.

The CDF curves of the proposed method exhibit enhanced precision, comparable to that of

Table 6.1: Summary of Percentiles for Cumulative Distribution Function ( $\|x\| = \{3.5, 25\}$  m)

Percentile	3.5 m				25 m			
	PAST	PAST/SVD	ESPRIT	2D-IFFT	PAST	PAST/SVD	ESPRIT	2D-IFFT
10	0.0250	0.0252	0.0259	0.2090	0.3983	0.2987	0.3847	0.5427
50	0.0251	0.0255	0.0312	0.8065	0.4730	0.3738	0.4103	0.9101
90	0.0253	0.2570	0.0373	1.5012	0.5325	0.5025	0.5563	1.3765

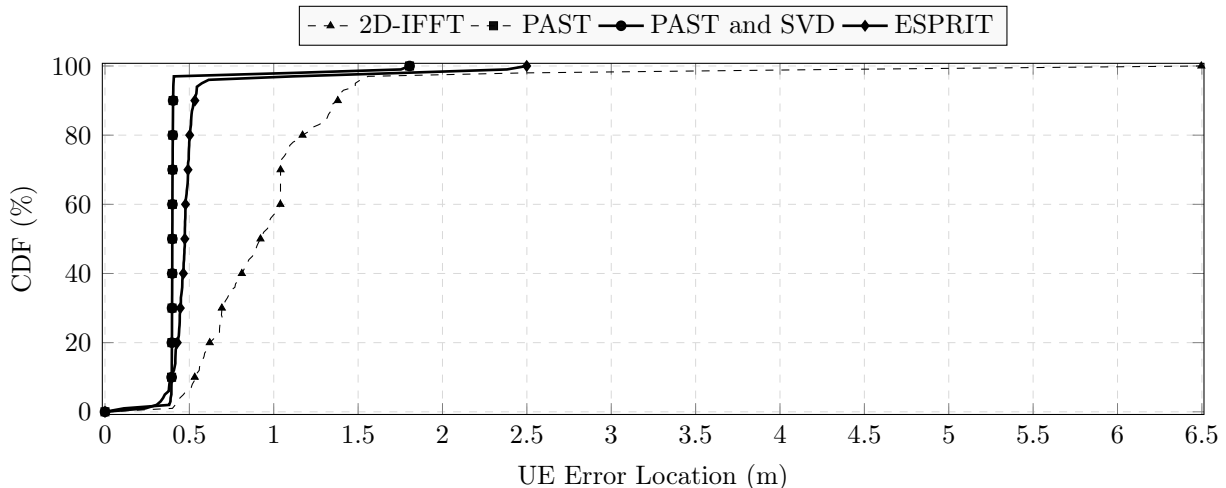


Figure 6.4: Comparison of empirical CDFs between estimators,  $\|x\| = 25$  m.

2D-IFFT. Additionally, compared to ESPRIT, the curves show a similar performance. However, it is crucial to highlight the lower computational burden of PAST. While the latter has a complexity of  $\mathcal{O}(Mr)$  per subarray, ESPRIT’s complexity is primarily dominated by the SVD, which is  $\mathcal{O}(M^3)$ . Therefore, the suggested technique shows reasonable needs, making it appropriate for subarrays with limited computational restrictions.

We compared the methods using the 10th, 50th, and 90th percentiles. Table I supports the findings in Figure 6.3 and Figure 6.4. The 2D-IFFT method has outliers, causing positioning errors over twice that of our method at the 90th percentile. At the 10th and 50th percentiles, all techniques achieve sub-meter accuracy, but our method performs better. Additionally, subspace-based methods have comparable performance.

## 6.4 CONCLUSION

In this chapter, we have presented a novel localization approach that combines the PAST algorithm and subarray processing for positioning estimation. We have achieved a balance between low complexity and high-accuracy localization. Our proposed method was compared to other well-known techniques using RMSE and CDF-based statistical analysis. The results show that our approach outperforms these techniques in terms of precision.

Despite to its successful performance, it is important to note that our algorithm in this chapter does not encompass 3D estimation, which involves computing azimuth, elevation angles

---

and range. This aspect will be addressed in the next chapter, where we will introduce a more comprehensive technique for 3D localization, we will introduce a technique that leverages the Jacobian matrix computed from the spatial gradients of the signal concerning the position.

## 3D USER LOCATION ESTIMATION

Estimating the three-dimensional position using antenna arrays poses a significant challenge in localization. This endeavor involves computing azimuth, elevation angles, and the range from a diverse array of environmental sources, classified as either near-field or far-field (MAZOKHA *et al.*, 2023).

3D-P estimation in the near field introduces unique challenges and opportunities, promising insights that could revolutionize wireless communication and signal processing. This becomes especially crucial with the advent of 6G cellular networks, where significant advancements are anticipated in localization and tracking (ELZANATY *et al.*, 2023; LIMA *et al.*, 2021).

This chapter delves into the problem of 3D localization, considering the use of ELAAs. These arrays are composed of URA, exhibiting properties akin to rotational invariance observed in far-field scenarios within the signal subspace. Leveraging this intrinsic attribute, we partition the localization challenge into smaller arrays, each independently estimating azimuth and elevation angles. In addition, our methodology employs the Taylor approximation technique, enabling us to address non-linear least squares problems adeptly.

### 7.1 SIGNAL MODEL

In this Chapter, we put our attention to a 3D configuration. Here, we consider a BS positioned near a single-antenna UE with an unknown location denoted as  $\mathbf{x} = [x, y, z]^T$ . The BS is equipped with a uniform rectangular antenna array comprising  $M$  elements, spaced at a uniform distance of  $d$  between adjacent elements. The center of the matrix acts as the reference point of the phase and the locations are represented by  $\mathbf{x}_{m_x, m_y} = [m_x d, m_y d, 0]^T$ , where  $m_x$  and  $m_y \in \{-M/2, \dots, M/2 - 1\}$ .

The signal model is structured with identical specifications as the one outlined in Chapter

6 in Section 6.1, differing only in that we now take into account a URA and operate within a 3D configuration.

## 7.2 TENSOR

Before delving into our 3D localization methods, we will introduce the concepts of tensors to provide a better understanding of our approach.

Tensors are generalizations of vectors and matrixes, for example, a third-order tensor or threeway array has three modes, indices or dimensions as shown in Fig. 7.1. A zero-order tensor is a scalar, a first-order tensor is a vector, a second-order tensor is a matrix, and tensors of order three and higher are called higher-order tensors (CICHOCKI *et al.*, 2009).

A tensor can be formally defined as:

**Definition 7.2.1.** (*Tensor*) Let  $I_1, I_2, \dots, I_N \in \mathbb{N}$  denote index upper bounds, A tensor  $\mathcal{Y} \in \mathbb{R}^{I_1 \times I_2 \times \dots \times I_N}$  of order  $N$  is an  $N$ -way array where elements  $y_{i_1, i_2, \dots, i_n}$  are indexed by  $i_n \in \{1, 2, \dots, I_n\}$  for  $1 \leq n \leq N$ .

Many modern applications generate large amounts of data with multiple aspects and high dimensionality for which tensors (i.e., multi-way arrays) provide a natural representation. Higher-

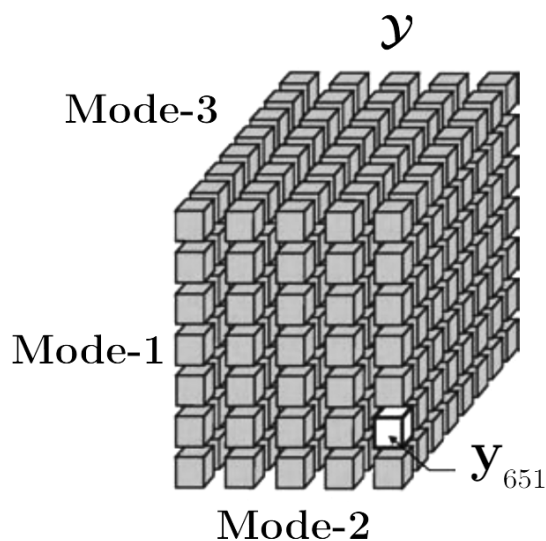


Figure 7.1: A three-way array (third-order tensor)  $\mathcal{Y} \in \mathbb{R}^{7 \times 5 \times 8}$  with elements  $y_{itq}$  (CICHOCKI *et al.*, 2009)

order tensor decompositions are nowadays frequently used in a variety of fields including telecommunication and signal processing. In this study, we will use the Tucker decomposition, one of the most commonly used decompositions.

### 7.2.1 Tucker Decompositions

The Tucker decomposition, also called the Tucker 3 or best rank  $(J, R, P)$  approximation, shown in Fig. 7.2 can be formulated as follows (CICHOCKI *et al.*, 2009):

Given a third-order data tensor  $\mathcal{Y} \in \mathbb{R}^{I \times T \times Q}$  and three positive indices  $\{J, R, P\} \ll \{I, T, Q\}$ , find a core tensor  $\mathcal{G} = [g_{jrp}] \in \mathbb{R}^{J \times R \times P}$  and three component matrices called factor or loading matrices or factors:  $\mathbf{A} = [\mathbf{a}_1, \mathbf{a}_2, \dots, \mathbf{a}_J] \in \mathbb{R}^{I \times J}$ ,  $\mathbf{B} = [\mathbf{b}_1, \mathbf{b}_2, \dots, \mathbf{b}_R] \in \mathbb{R}^{T \times R}$ , and  $\mathbf{C} = [\mathbf{c}_1, \mathbf{c}_2, \dots, \mathbf{c}_P] \in \mathbb{R}^{Q \times P}$ , which perform the following approximate decomposition:

$$\mathcal{Y} = \sum_{j=1}^J \sum_{r=1}^R \sum_{p=1}^P g_{jrp} (\mathbf{a}_j \circ \mathbf{b}_r \circ \mathbf{c}_p) + \mathcal{E} \quad (7.1)$$

or equivalently in the element-wise form:

$$\mathcal{Y}_{itq} = \sum_{j=1}^J \sum_{r=1}^R \sum_{p=1}^P g_{jrp} a_{ij} b_{tr} c_{qp} + e_{itq}, \quad (7.2)$$

where  $\mathbf{a}_j \in \mathbb{R}^I$ ,  $\mathbf{b}_j \in \mathbb{R}^T$ , and  $\mathbf{c}_j \in \mathbb{R}^Q$ , that is, the vectors within the associated component factor matrices  $\mathbf{A}$ ,  $\mathbf{B}$  and  $\mathbf{C}$ , and  $g_{jrp}$  are scaling factors which are the entries of a core tensor

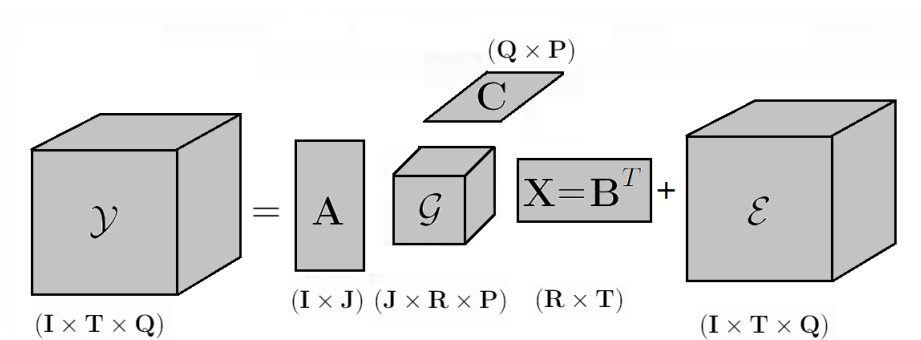


Figure 7.2: Tucker3 model is a weighted sum of the outer product of three vectors (factors) stored as columns of component matrices  $\mathbf{A} \in \mathbb{R}^{I \times J}$ ,  $\mathbf{B} = \mathbf{X}^T \in \mathbb{R}^{T \times R}$  and  $\mathbf{C} \in \mathbb{R}^{Q \times P}$ . The core tensor  $\mathcal{G} \in \mathbb{R}^{J \times R \times P}$  defines a linking structure between the set of components and  $J, R$ , and  $P$  denote the number of components. In order to achieve uniqueness for the Tucker models it is necessary to impose additional constraints such as sparsity and nonnegativity (CICHOCKI *et al.*, 2009)

$$\mathcal{G} = [g_{jrp}] \in \mathbb{R}^{J \times R \times P}.$$

The Tucker model can be described in several mathematically equivalent ways. One such representation involves expressing it in matrix form through mode- $n$  multiplications.

$$\mathcal{Y} = \mathcal{G} \times_1 \mathbf{A} \times_2 \mathbf{B} \times_3 \mathbf{C} + \mathcal{E} = \llbracket \mathbf{G}; \mathbf{A}, \mathbf{B}, \mathbf{C} \rrbracket + \mathcal{E}, \quad (7.3)$$

where  $\hat{\mathcal{Y}} = \llbracket \mathcal{G}; \mathbf{A}, \mathbf{B}, \mathbf{C} \rrbracket$  is the shorthand notation for the Tucker3 tensor decomposition. Using the unfolding approach we can obtain matrix forms expressed compactly by the Kronecker products:

$$\mathbf{Y}_{(1)} \cong \mathbf{A} \mathbf{G}_{(1)} (\mathbf{C} \otimes \mathbf{B})^T, \quad (7.4)$$

$$\mathbf{Y}_{(2)} \cong \mathbf{B} \mathbf{G}_{(2)} (\mathbf{C} \otimes \mathbf{A})^T, \quad (7.5)$$

$$\mathbf{Y}_{(3)} \cong \mathbf{C} \mathbf{G}_{(3)} (\mathbf{B} \otimes \mathbf{A})^T. \quad (7.6)$$

It is often convenient to represent the three-way Tucker model in its vectorized forms:

$$\begin{aligned} \text{vec}(\mathbf{Y}_{(1)}) &\cong \text{vec}(\mathbf{A} \mathbf{G}_{(1)} (\mathbf{C} \otimes \mathbf{B})^T) = (\mathbf{C} \otimes \mathbf{B}) \otimes \mathbf{A} \text{vec}(\mathbf{G}_{(1)}), \\ \text{vec}(\mathbf{Y}_{(2)}) &\cong \text{vec}(\mathbf{B} \mathbf{G}_{(2)} (\mathbf{C} \otimes \mathbf{A})^T) = (\mathbf{C} \otimes \mathbf{A}) \otimes \mathbf{B} \text{vec}(\mathbf{G}_{(2)}), \\ \text{vec}(\mathbf{Y}_{(3)}) &\cong \text{vec}(\mathbf{C} \mathbf{G}_{(3)} (\mathbf{B} \otimes \mathbf{A})^T) = (\mathbf{B} \otimes \mathbf{A}) \otimes \mathbf{C} \text{vec}(\mathbf{G}_{(3)}). \end{aligned} \quad (7.7)$$

The Tucker model discussed earlier is commonly referred to as the Tucker3 model. In this model, a third-order tensor is decomposed into three factor matrices, referred to as loading matrices, denoted as  $\{\mathbf{A}, \mathbf{B}, \mathbf{C}\}$ , along with a core tensor  $\mathcal{G}$ . When dealing with scenarios where we only have two factor matrices or even just one, the Tucker3 model for a three-way tensor transforms into simplified versions known as the Tucker 2 or Tucker 1 models (CICHOCKI *et al.*, 2009).

### 7.3 SUBSPACE SEPARATION

Now that we have discussed the concept of tensors, let us consider Eq. (6.4), which can be viewed as a concatenation of  $N$  received signals corresponding to subarrays of  $P$  antenna elements in the matrix  $\mathbf{Y} = [\mathbf{Y}_0^T, \dots, \mathbf{Y}_{N-1}^T]$ , where  $\mathbf{Y}_n \in \mathcal{C}^{P \times K}$ .

Using tensor decomposition, we address azimuth and elevation estimations more effectively by modeling linear subarrays in the second and third dimensions of the rectangular array. To each subarray, the signal can be associated with the tensor model. More specifically, the signal associated with the  $n$  th subarray can be expressed as

$$\mathcal{Y}_n = \mathcal{X}_n + \mathcal{W}_n, \quad (7.8)$$

where  $n \in \{0, 1, \dots, N-1\}$ ,  $\mathcal{Y}_n \in \mathbb{C}^{K \times I_1 \times I_2}$ ,  $P = I_1 I_2$ ,  $\mathcal{X}_n \in \mathbb{C}^{(K \times I_1 \times I_2)}$  is the training sequence, and  $\mathcal{W}_n$  represents tensor complex noise. Without a lack of generality, we consider  $I_1 = I_2 = I = \sqrt{P}$ , where  $\sqrt{P} \in \mathcal{Z}^+$ .

Azimuth and elevation are efficiently estimated using the ESPRIT algorithm, extracting the relevant subspace. This involves decomposing the tensor  $\mathcal{Y}_m$  using HOSVD, the concepts of which we will describe in the next section.

### 7.3.1 HOSVD

The HOSVD is a fundamental concept in multilinear algebra, extending the idea of SVD described in Chapter 4 in Section 4.3.1.1 to higher-dimensional data structures known as tensors. While SVD is specifically designed for matrices, HOSVD generalizes this decomposition to tensors of any order, enabling efficient analysis and manipulation of multidimensional data (MARKOPOULOS *et al.*, 2018).

The essence of HOSVD lies in decomposing a tensor into a set of core tensors and orthogonal factor matrices along each mode or dimension. This decomposition allows us to extract meaningful and interpretable information from complex data structures, aiding in tasks such as dimensionality reduction, feature extraction, and data compression (KOLDA; BADER, 2009), (MOOR *et al.*, 1995).

Consider the abstract tensor  $\mathcal{A}$  given in coordinates with respect to some basis as an  $\Gamma$ -way array, denoted by  $\mathcal{A} \in \mathbb{C}^{I_1 \times I_2 \times \dots \times I_\Gamma \times \dots \times I_\Gamma}$ , where  $\Gamma$  is the number of modes and the order of the tensor. Here,  $\mathbb{C}$  represents the complex numbers, encompassing both real numbers  $\mathbb{R}$  and pure imaginary numbers.

Now, let  $\mathbf{U}_\Gamma \in \mathbb{C}^{I_\Gamma \times I_\Gamma}$  be a unitary matrix containing a basis of the left singular vectors of

the standard mode- $\Gamma$  flattening  $\mathcal{A}_{[\Gamma]}$  of  $\mathcal{A}$ . Each column  $\mathbf{u}_j$  of  $\mathbf{U}_\Gamma$  corresponds to the  $j$ -th largest singular value of  $\mathcal{A}_{[\Gamma]}$ . Notably, the mode/factor matrix  $\mathbf{U}_\Gamma$  remains independent of the specific definition of the mode- $\Gamma$  flattening. Utilizing the properties of multilinear multiplication, we derive ( ):

$$\begin{aligned} \mathcal{A} &= \mathcal{A} \times (\mathbf{I}, \mathbf{I}, \dots, \mathbf{I}) \\ &= \mathcal{A} \times (\mathbf{U}_1 \mathbf{U}_1^H, \mathbf{U}_2 \mathbf{U}_2^H, \dots, \mathbf{U}_\Gamma \mathbf{U}_\Gamma^H) \\ &= (\mathcal{A} \times (\mathbf{U}_1^H, \mathbf{U}_2^H, \dots, \mathbf{U}_\Gamma^H)) \times (\mathbf{U}_1, \mathbf{U}_2, \dots, \mathbf{U}_\Gamma), \end{aligned} \quad (7.9)$$

The second equality holds because the  $\mathbf{U}_\Gamma$ 's are unitary matrices. Now, define the core tensor as  $\mathcal{S} := \mathcal{A} \times (\mathbf{U}_1^H, \mathbf{U}_2^H, \dots, \mathbf{U}_\Gamma^H)$ . Therefore, the HOSVD of  $\mathcal{A}$  is the decomposition:

$$\mathcal{A} = \mathcal{S} \times (\mathbf{U}_1, \mathbf{U}_2, \dots, \mathbf{U}_\Gamma). \quad (7.10)$$

This construction demonstrates that every tensor has an associated HOSVD.

### 7.3.2 Azimuth and Elevation Estimation

Azimuth and elevation measurements are accurately estimated using the ESPRIT algorithm, detailed in Chapter 4. The algorithm initiates by extracting the subspace associated with the second and third dimensions, providing crucial azimuth and elevation measurements.

This extraction is facilitated through the decomposition of the tensor  $\mathcal{Y}_n$  using the HOSVD method. The decomposition is expressed as follows:

$$\mathcal{X}_n = \mathcal{G}_n \times_1 \mathbf{U}_1^m \times_2 \mathbf{U}_2^m \times_3 \mathbf{U}_3^m, \quad (7.11)$$

where each term  $\mathbf{U}_i^m$  denotes an orthogonal matrix corresponding to the  $i$ th mode of the tensor  $\mathcal{Y}_n$ . The HOSVD is used to produce results based on the Tucker3 tensor model from the  $n$ th subarray.

Subsequently, the ESPRIT algorithm is used to independently calculate the azimuth and elevation measurements of the modes  $\mathbf{U}_2^m$  and  $\mathbf{U}_3^m$ , respectively. This approach considers  $\mathbf{U}_2^m$  and  $\mathbf{U}_3^m$  as two distinct ULAs. The first ULA consists of virtual antennas whose positions are only along the  $y$  axis, while the second ULA has antennas located only along the  $z$  axis.

Using the orthonormal matrix  $\mathbf{U}_2^m$ , it is possible to calculate the azimuth of the most

representative column, which is the first. This is done by transforming it into two vectors:  $\mathbf{u}_1 = [e^{-j\omega_0}, \dots, e^{-j\omega(I-2)}]$  and  $\mathbf{u}_2 = [e^{-j\omega_1}, \dots, e^{-j\omega(I-1)}]$ . Similar to Eq. (6.11), this enables us to estimate the value of  $\theta_n$  for subarray as:

$$\hat{\phi}_n = \sin^{-1} \left( \frac{\lambda}{2\pi Id} \sum_{i=0}^{I-1} \arg(\text{diag}[\mathbf{u}_1^* \mathbf{u}_2]_i) \right), \quad (7.12)$$

where  $\arg(\text{diag}[\mathbf{u}_1^* \mathbf{u}_2]_i)$  extracts the argument for the entry of the  $i$ th complex number of vector  $\text{diag}[\mathbf{u}_1^* \mathbf{u}_2]$ .

Elevation estimation is performed in a similar way using the matrix  $\mathbf{U}_3^m$ . As the virtual ULA is orientated, the estimated angle must be multiplied by a negative value. Thus, the estimated elevation of the subarray  $n$  is expressed as:

$$\hat{\theta}_n = -\sin^{-1} \left( \frac{\lambda}{2\pi Id} \sum_{i=0}^{I-1} \arg(\text{diag}[\mathbf{u}_1^* \mathbf{u}_2]_i) \right). \quad (7.13)$$

### 7.3.3 User Position Estimation

Once each subarray has estimated its azimuth and elevation, the connection between Cartesian coordinates can be utilized. This allows us to combine the estimated angles into  $\mathbf{q} = [\mathbf{q}_0^T, \dots, \mathbf{q}_{N-1}^T]^T$ , where  $\mathbf{q}_n = [\hat{\theta}_n, \hat{\phi}_n]^T$ , and apply the correlation with the user's position as specified by:

$$\begin{bmatrix} \phi_n \\ \theta_n \end{bmatrix} = \begin{bmatrix} \tan^{-1} \left( \frac{y_n - y}{x_n - x} \right) \\ \sin^{-1} \left( \frac{z_n - z}{r_n} \right) \end{bmatrix}, \quad (7.14)$$

where  $[x_n, y_n, z_n]$  are the center position of the  $n$ th subarray while  $\mathbf{x} = [x, y, z]$  is the user position, and  $r_n = \sqrt{(x_n - x)^2 + (y_n - y)^2 + (z_n - z)^2}$ . The relationship between user position, azimuth, and elevation follows a nonlinear function.

Our approach then consists of minimizing the nonlinear function

$$\begin{aligned} J(x, y, z) &= \sum_{n=0}^{N-1} \left\| \mathbf{q}_n - \begin{bmatrix} \tan^{-1} \left( \frac{y_n - y}{x_n - x} \right) \\ \sin^{-1} \left( \frac{z_n - z}{r_n} \right) \end{bmatrix} \right\|_2^2 \\ &= \sum_{n=0}^{N-1} \|\mathbf{q}_n - \mathbf{h}_n(x, y, z)\|_2^2, \\ &= \|\mathbf{q} - \mathbf{h}(\mathbf{x})\|_2^2, \end{aligned} \quad (7.15)$$

where  $\mathbf{h}_n(x, y, z) \equiv \mathbf{h}_n(\mathbf{x})$  is defined in Equation (7.14),  $\mathbf{h}(\mathbf{x}) = [\mathbf{h}_0(\mathbf{x}), \dots, \mathbf{h}_{N-1}(\mathbf{x})]^T$ , and  $\mathbf{q} = [\mathbf{q}_0^T, \dots, \mathbf{q}_{N-1}^T]^T$ .

The problem is non-linear and challenging to solve, so we use the Taylor series approximation for the function  $\mathbf{h}_n(\mathbf{x})$ . Its first-order approximation is expressed as  $\mathbf{h}_n(\mathbf{x}) \approx \mathbf{h}_n(\mathbf{x}_0) + \mathbf{H}_n(\mathbf{x} - \mathbf{x}_0)$ , where  $\mathbf{x}_0 = \mathbf{x} - d\mathbf{x}$  and the Jacobian matrix is

$$\mathbf{H}_n = \begin{bmatrix} \frac{\partial \phi_n}{\partial x} & \frac{\partial \phi_n}{\partial y} & \frac{\partial \phi_n}{\partial z} \\ \frac{\partial \theta_n}{\partial x} & \frac{\partial \theta_n}{\partial y} & \frac{\partial \theta_n}{\partial z} \end{bmatrix}. \quad (7.16)$$

We then form the matrix  $\mathbf{H} = [\mathbf{H}_0^T, \dots, \mathbf{H}_{N-1}^T]^T$  by combining the Jacobian  $N$  matrices. Therefore,  $\mathbf{h}(\mathbf{x}) \approx \mathbf{h}(\mathbf{x}_0) + \mathbf{H}(\mathbf{x} - \mathbf{x}_0)$ .

The cost function can be approximated as:

$$\begin{aligned} J(\mathbf{x}) &\approx \|\mathbf{q} - \mathbf{h}(\mathbf{x}_0) - \mathbf{H}(\mathbf{x} - \mathbf{x}_0)\|_2^2 \\ &= \|\mathbf{q} - \mathbf{h}(\mathbf{x}_0) - \mathbf{H}\mathbf{x} + \mathbf{H}\mathbf{x}_0\|_2^2 \\ &= \|\tilde{\mathbf{q}} - \mathbf{H}\mathbf{x}\|_2^2, \end{aligned} \quad (7.17)$$

where  $\tilde{\mathbf{q}} = \mathbf{q} - \mathbf{h}(\mathbf{x}_0) + \mathbf{H}\mathbf{x}_0$ . The solution to the approximate linear problem is  $\hat{\mathbf{x}} = \mathbf{H}^\dagger \tilde{\mathbf{q}}$ . By expanding the term  $\tilde{\mathbf{q}}$ , the new estimator is given by:

$$\begin{aligned} \hat{\mathbf{x}} &= \mathbf{H}^\dagger(\mathbf{q} - \mathbf{h}(\mathbf{x}_0) + \mathbf{H}\mathbf{x}_0) \\ &= \mathbf{H}^\dagger \mathbf{H}\mathbf{x}_0 + \mathbf{H}^\dagger(\mathbf{q} - \mathbf{h}(\mathbf{x}_0)) \\ &= \mathbf{x}_0 + \mathbf{H}^\dagger(\mathbf{q} - \mathbf{h}(\mathbf{x}_0)). \end{aligned} \quad (7.18)$$

This equation suggests an iterative procedure defined by:

$$\hat{\mathbf{x}}[k+1] = \hat{\mathbf{x}}[k] + \mathbf{H}^\dagger(\mathbf{q} - \mathbf{h}(\mathbf{x}[k])), \quad (7.19)$$

where the matrix  $\mathbf{H}$  is updated at each step as specified by its sub-matrices in Equation (7.16).

The derivatives are calculated as:

$$\begin{aligned}\frac{\partial \phi_n}{\partial x} &= -\frac{(y - y_n)}{(x - x_n)^2 + (y - y_n)^2}, \\ \frac{\partial \phi_n}{\partial y} &= \frac{(x - x_n)}{(x - x_n)^2 + (y - y_n)^2}, \\ \frac{\partial \phi_n}{\partial z} &= 0, \\ \frac{\partial \theta_n}{\partial x} &= \frac{(x + x_n)(z - z_n)}{\sqrt{\left(1 - \frac{(z - z_n)^2}{(x + x_n)^2 + (y + y_n)^2 + (z + z_n)^2}\right) \left((x + x_n)^2 + (y + y_n)^2 + (z + z_n)^2\right)^3}}, \\ \frac{\partial \theta_n}{\partial y} &= \frac{(y + y_n)(z - z_n)}{\sqrt{\left(1 - \frac{(z - z_n)^2}{(x + x_n)^2 + (y + y_n)^2 + (z + z_n)^2}\right) \left((x + x_n)^2 + (y + y_n)^2 + (z + z_n)^2\right)^3}}, \\ \frac{\partial \theta_n}{\partial z} &= -\frac{(x + x_n)^2 + (y + y_n)^2 + (z + z_n)^2 - z^2 + z_n^2}{\sqrt{\left(1 - \frac{(z - z_n)^2}{(x + x_n)^2 + (y + y_n)^2 + (z + z_n)^2}\right) \left((x + x_n)^2 + (y + y_n)^2 + (z + z_n)^2\right)^3}}.\end{aligned}$$

The Jacobian matrix  $\mathbf{H}$  can be ill-conditioned, resulting in a non-unique pseudoinverse. To address this, we employ the Levenberg-Marquadt algorithm, which is a combination of gradient descent and Gauss-Newton methods. This modifies Equation (7.19) to:

$$\hat{\mathbf{x}}[k + 1] = \hat{\mathbf{x}}[n] + (\mathbf{H}^T \mathbf{H} + \lambda \text{Diag}(\mathbf{H}^T \mathbf{H}))^{-1} \mathbf{H}^T (\mathbf{q} - \mathbf{h}(\mathbf{x}[k])), \quad (7.20)$$

where the  $\text{Diag}(\mathbf{H}^T \mathbf{H})$  operator extracts the main diagonal of matrix  $\mathbf{H}^T \mathbf{H}$  and  $\lambda$  is a damping factor. A summary of the solution is provided in Algorithm 3.

### 7.3.4 Computational Complexity Analysis

We can assess the algorithm's computational complexity by examining each operation to determine its cost. The  $m$ th subarray has a signal tensor with dimensions  $\mathbb{C}^{P \times I_1 \times I_2}$ , and the complexity of the HOSVD for a third-order tensor is  $\mathcal{O}(PI_1^2 I_2 + P^2 I_1 I_2 + PI_1 I_2^2)$ . This leads to a complexity of  $\mathcal{O}(M [LI_1^2 I_2 + L^2 I_1 I_2 + LI_1 I_2^2])$  for all  $M$  subarrays. Inside the loop 'While', the most significant operation is the pseudoinverse  $(\mathbf{H}^T \mathbf{H} + \lambda \text{Diag}(\mathbf{H}^T \mathbf{H}))^{-1} \mathbf{H}^T$ , which has a computational complexity  $\mathcal{O}(12M^2)$ . Thus, assuming the worst case, where  $K_{\max}$  iterations are needed to estimate the position of the user, the estimated complexity of the entire algorithm is  $\mathcal{O}(M [(PI_1^2 I_2 + P^2 I_1 I_2 + PI_1 I_2^2) + 12M^2 K_{\max}])$ . In our case, we assume  $I_1 = I_2 = I$ , so the computational complexity is  $\mathcal{O}(M [2PI^3 + P^2 I^2] + 12M^2 K_{\max})$ . Although we are dealing with

**Algorithm 3** Proposed Algorithm

---

Split the matrix into smaller sub-arrays to form the tensor signal model as in Eq. 7.8

**for** each subarray  $n$  **do**

    Use HOSVD to obtain the decomposition as shown in Equation (7.11)

    Use  $\mathbf{U}_2^m$  with Equation (7.12)

    Use  $\mathbf{U}_3^m$  with Equation (7.13)

    Set  $\mathbf{q}_n = [\hat{\phi}_n, \hat{\theta}_n]^T$

    Stack the new estimate into  $\mathbf{q} = [\mathbf{q}_0^T, \dots, \mathbf{q}_n^T]^T$

**end for**

Create an initial guess for  $\mathbf{x}[0]$

Define the maximum number of iterations as  $K_{\max}$

Compute the error vector  $\mathbf{e} = \mathbf{q} - \mathbf{h}(\mathbf{x}[0])$

**while**  $\|\mathbf{e}\| \geq \epsilon$  and  $k < K_{\max}$  **do**

    Calculate the matrix  $\mathbf{H} = [\mathbf{H}_0^T, \dots, \mathbf{H}_{M-1}^T]^T$ , where  $\mathbf{H}_n$  is defined in Equation (7.16).

    Update the error vector as  $\mathbf{e} = \mathbf{q} - \mathbf{h}(\mathbf{x}[k])$

    Compute  $\mathbf{x}[k+1]$  using Equation (7.20)

    Increment  $n$  by 1

**end while**

---

extra large arrays, the computational complexity is in the function of the dimension of the subarray, which we can design within an acceptable computational complexity, considering the limitations of signal processing capabilities.

## 7.4 SIMULATION AND NUMERICAL RESULTS

In our indoor scenario, we consider a carrier frequency  $f_c$  of 15 GHz, where the speed of light  $c$  is 0.3 m/ns, resulting in a wavelength  $\lambda$  of 0.02 meters. The system comprises  $K = 256$  subcarriers with quadrature phase shift keying (QPSK) pilots and a bandwidth  $W$  of 1 GHz and a subcarrier spacing  $d_f = W/K$ . For simulation purposes, we used an antenna element with an isotropic response pattern. To simulate a large array, we consider a set of URA subarrays with  $4 \times 4$  elements with half-wavelength spacing replicated to obtain a  $32 \times 32$  URA. Figure 7.3 represents the configuration of the array. Under such conditions, the near-field region  $r_{\text{NF}} < \frac{2D^2}{\lambda}$  is approximately 82 meters.

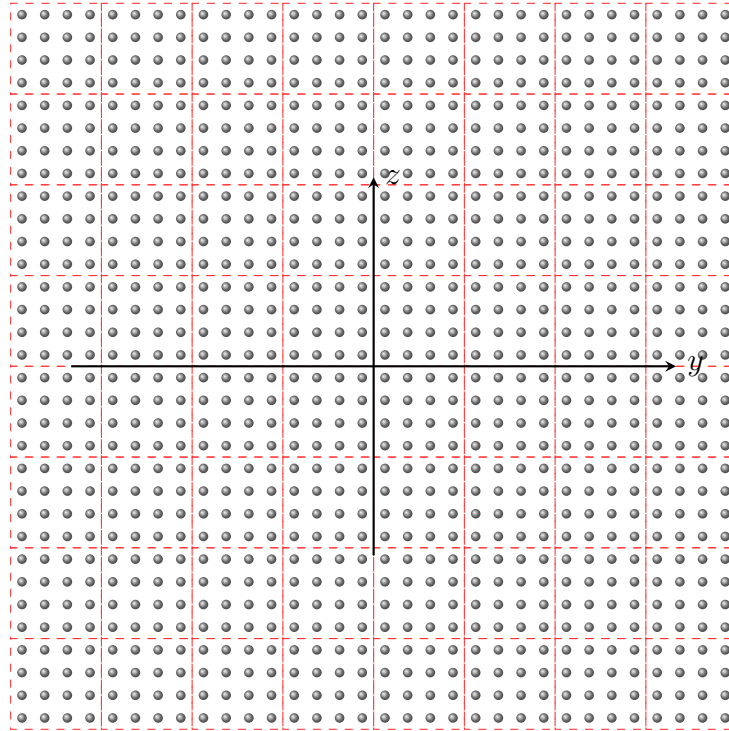


Figure 7.3: Visual representation of a 32x32 planar antenna array with 4x4 subarrays.

We evaluate our algorithm via simulations, considering multipath interference due to reflection, which may bias the estimation. These interference are NLOS components, i.e.,  $L > 0$  in Eq. (6.1). As a baseline, we also consider in our evaluation, the LOS scenario, i.e.,  $L = 0$  in Eq. (6.1). The simulation's performance metrics are the CDF of the UE location error and the RMSE of the localization algorithm.

In the following results, we consider the SNR at the receiver side. The noise variance calculation is based on the average spectrum power of the received signal per antenna. Therefore, in our simulations, we calculate the noise variance  $\sigma^2$  as the ratio of the mean received power and the desired SNR.

Figure 7.4 displays the CDF of the UE error location with a simulated SNR =  $-20$  dB for LOS only, 2, 4, and 8 scatters. The algorithm performance degrades with increasing scatters due to multipath interference. In contrast, Figure 7.5 shows the algorithm enhancement with lower noise power, SNR =  $-10$  dB. Specifically, the 90<sup>th</sup> percentile of the 8 scatters curves improves about 4.4 times from 27.863 to 6.344 meters. This improvement highlights the SNR's role in defining the algorithm's operational area within an acceptable error margin for a service.

The improvement shown in Fig. 7.5 compared to Fig. 7.4 is due to the impact of noise

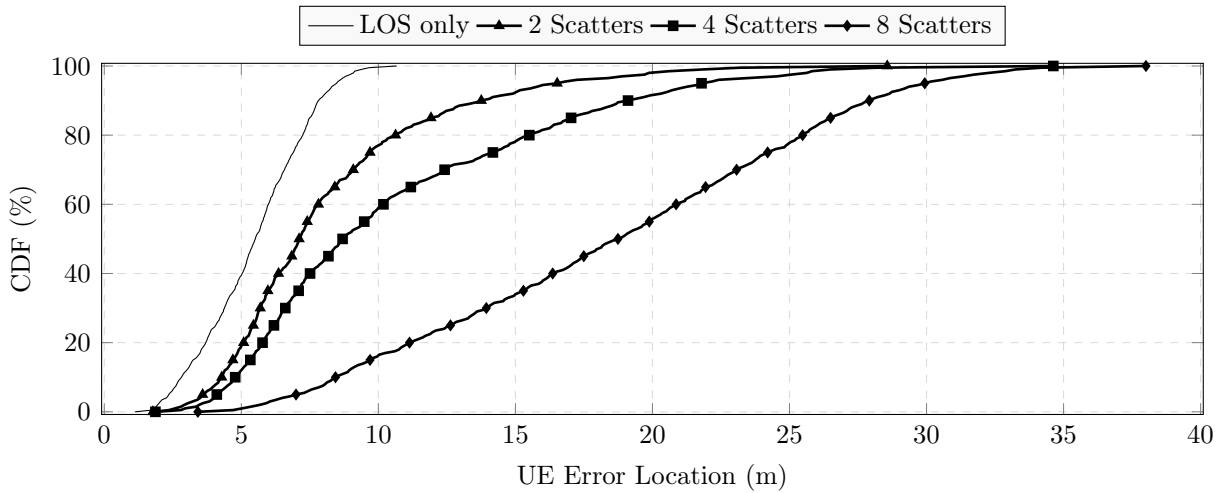


Figure 7.4: CDF of the UE location error for SNR = -20 dB.

power on the performance of HOSVD, a subspace method sensitive to rank selection. Although not optimized here, identifying this parameter could be a future research topic. We extract azimuth and elevation from the first eigenvector of the tensor’s second and third factor matrices, assuming that the signal LOS power is significantly higher than the NLOS components. However, a low SNR makes the distinction between LOS and NLOS challenging. Errors also arise from the reliability of iterative methods, dependence on the Jacobian matrix, the influence of the SNR on matrix conditioning, and convergence speed.

Figure 7.6 shows a scenario with 0 dB SNR, where the noise power has minimal impact and multiple paths mainly influence the algorithm performance. The proximity of curves for different numbers of scatterer demonstrates the effectiveness of the algorithm against multipath

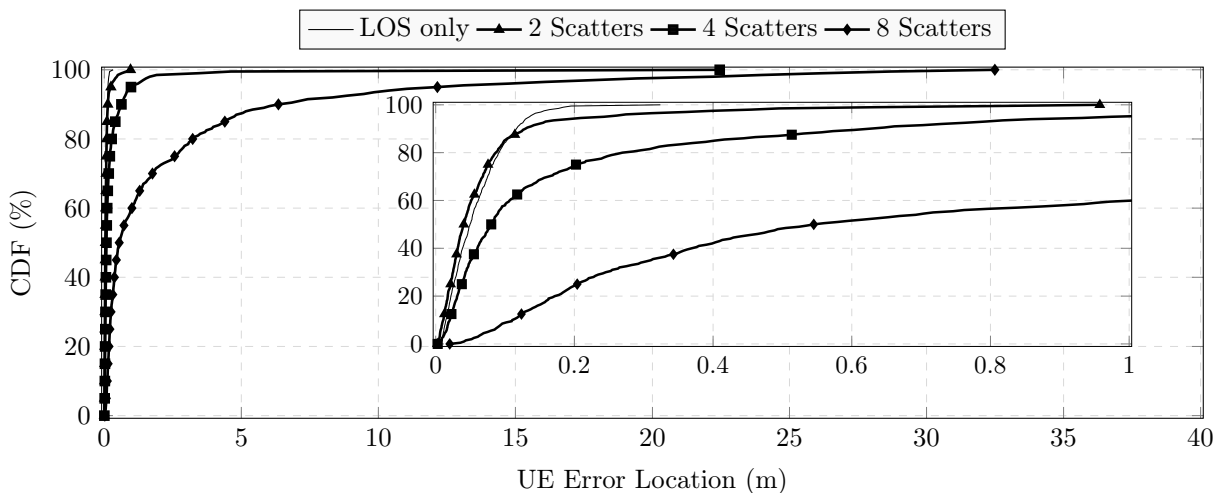


Figure 7.5: CDF of the UE Location Error for SNR = -10 dB.

Table 7.1: Comparison of 10<sup>th</sup>, 50<sup>th</sup>, and 90<sup>th</sup> percentiles across scenarios with varied SNRs for LOS only, 2, 4 and 8 scatters.

# of scatters	-20 dB			-10 dB			0 dB		
	10 <sup>th</sup>	50 <sup>th</sup>	90 <sup>th</sup>	10 <sup>th</sup>	50 <sup>th</sup>	90 <sup>th</sup>	10 <sup>th</sup>	50 <sup>th</sup>	90 <sup>th</sup>
LOS only	2.799 m	5.510 m	7.811 m	1.453 cm	4.944 cm	11.625 cm	0.602 cm	2.846 cm	8.378 cm
2	4.277 m	7.109 m	13.658 m	1.090 cm	4.026 cm	12.833 cm	0.873 cm	3.803 cm	11.330 cm
4	4.764 m	8.694 m	18.965 m	2.006 cm	7.989 cm	62.532 cm	1.741 cm	8.000 cm	59.481 cm
8	8.427 m	18.652 m	27.863 m	11.044 cm	53.987 cm	6.344 m	10.902 cm	52.894 cm	9.128 m

interference.

Table 7.1 compares the percentiles of 10<sup>th</sup>, 50<sup>th</sup>, and 90<sup>th</sup> in SNR scenarios of -20 dB, -10 dB and 0 dB, considering the LOS only scenario, as well as, the multipath one with 2, 4, and 8 scatters. The data suggest that submeter accuracy is attainable at SNR  $\geq -10$  dB for the 10<sup>th</sup> and 50<sup>th</sup> percentiles, while at 0 dB, this accuracy can be achieved except for the 90<sup>th</sup> percentile with 8 scatters. A notable improvement trend is observed as the SNR increases, with diminishing variability between percentiles, indicating a more predictable and reliable performance. However, as the number of scatter increases, there is a discernible impact on the 90<sup>th</sup> percentile values. The best performance is consistently seen with the highest SNR considered of 0 dB, where even in the presence of 4 scatters, the 90<sup>th</sup> percentile measurement does not exceed 53.987 centimeters, underscoring the technique’s potential for applications requiring high precision. Conversely, the most challenging setup is at -20 dB with 8 scatters, where the accuracy hovers around 27.863 meters at the 90<sup>th</sup> percentile, highlighting the conditions under which the performance of the system may be compromised.

We analyze the root mean square error by varying the distance between the UE and the

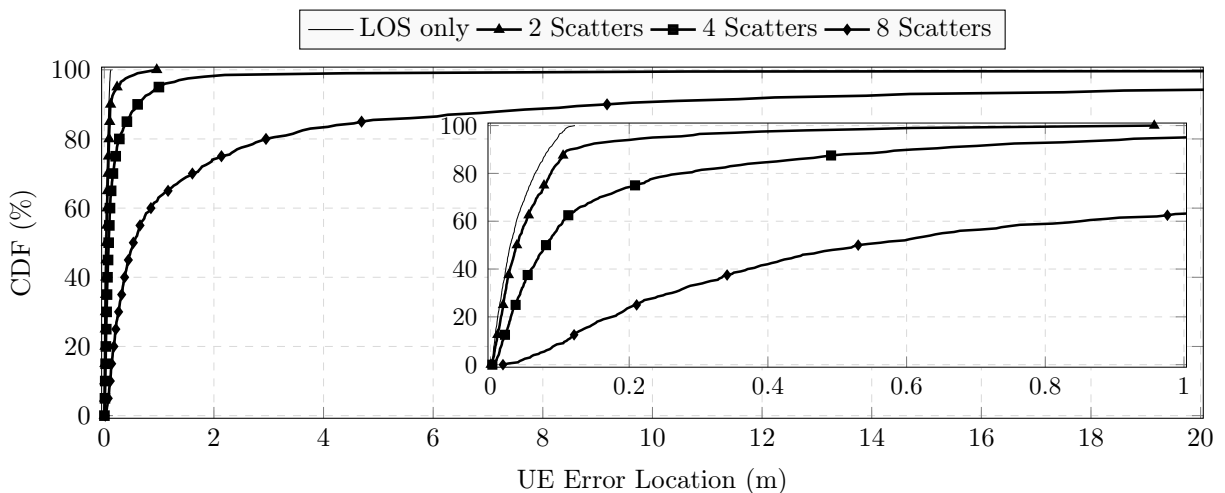


Figure 7.6: CDF of the UE Location Error for SNR = 0 dB.

access point. Figure 7.7 shows that the algorithm demonstrates efficacy in the challenging near-field scenario for distances closer to the antenna, especially for 10 dBm and 2 scatters. This is attributed to the combination of higher signal strength and a moderate number of scatters, which enhance the SNR. However, it should be noted that as the distances become larger, the performance of the algorithm tends to decrease. This is natural since we have a fixed transmitted power, and so the SNR tends to decrease. As we discussed previously, noise power is one of the sources of error that can degrade algorithm performance.

## 7.5 CONCLUSION

In this Chapter, we propose a 3D-P estimation method designed for wireless systems employing URAs. This approach virtually partitions the array into subarrays, each is tasked with independently estimating azimuth and elevation angles. To handle the multidimensional data effectively, we employ HOSVD, reducing tensor size for a more concise representation of data structure, particularly beneficial in URA applications. Additionally, we utilize Taylor series approximation to address non-linear least square problems, contributing to accurate position estimations.

The results show that even for low SNRs, it is still possible to achieve accuracy within the sub-meter range. This occurs with 90% probability if there are few scatters in the scenario; in other words, the multipath interference is very low. Furthermore, the algorithm has shown

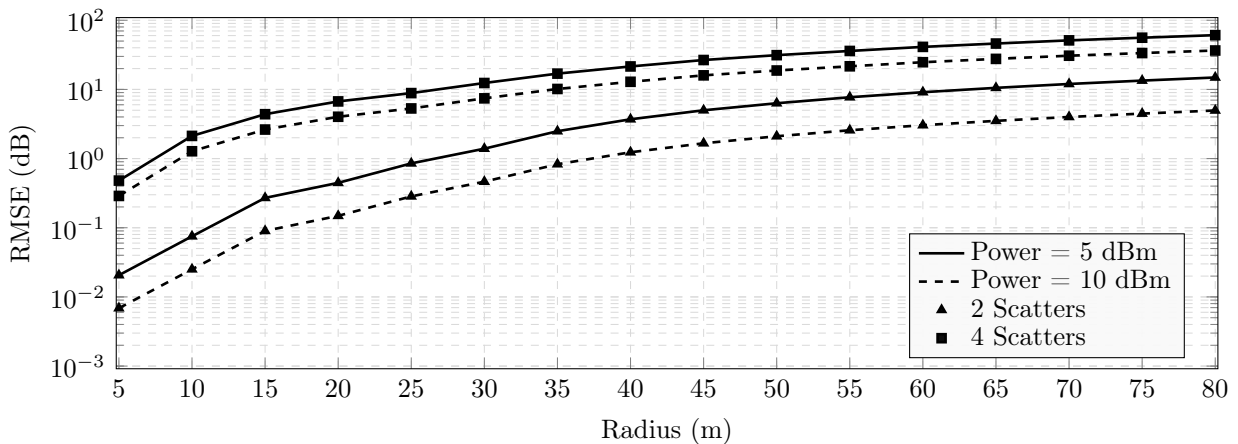


Figure 7.7: The curves represent different power levels (5 dBm, 10 dBm) and scatter scenarios (2, 4).

excellent performance in canceling multipath interference with very high SNRs.

Additionally, the RMSE vs. Radius plot further underscores the algorithm's proficiency for different numbers of scatters and power of transmission. The low RMSE values at different distances from the base station ranging from 5 to 100 meters highlight its consistent accuracy in user localization. Even when users assume random positions within this radius, the algorithm maintains low error rates. This performance, both in terms of CDF under multipath interference conditions and RMSE across varying distances, attests to the algorithm's robustness, making it well-suited for real-world deployment scenarios.

In summary, the algorithm proposed shows great potential in addressing the issues related to wireless communication and signal processing, especially in the changing environment of 6G networks. Its effectiveness in determining the 3D location using antenna arrays in close-range scenarios despite multipath interference is a useful tool for precise location in various settings.

### 8.1 FINAL CONSIDERATIONS

Source localization using a sensor array is a pivotal research area within array signal processing, finding applications in radar, sonar, medical electronics, and beyond. The problem of source localization can be approached in two distinct manners, depending on the distance between the source and the array. When the source lies beyond the Fresnel region, it is categorized as far-field, necessitating a specific modeling approach. Conversely, when the source is within the Fresnel region, the problem shifts to the near-field domain, requiring a different modeling strategy. Our research predominantly focuses on the intricate near-field scenario and its associated applications.

The localization of transmitted signals in antenna arrays, particularly in near-field scenarios, remains a challenging yet critical aspect of signal processing research.

One of the cornerstones of our research lies in the strategic utilization of sub-array techniques. By partitioning the antenna array into smaller sub-arrays, we reduced computational complexity and unlocked the potential for integration with other advanced techniques. The incorporation of sub-array techniques facilitated seamless integration with sophisticated algorithms like the PAST algorithm in 2D localization and the HOSVD algorithm in 3D localization. This approach allowed us to balance computational efficiency and high-accuracy localization harmoniously, overcoming traditional limitations associated with near-field scenarios.

In this dissertation, we explored two distinct yet interconnected aspects of source localization: 2D source localization in near-field and 3D source location in the near-field.

- *2D Source Localization in Near Field* The first part of our research focused on 2D source localization in near field, where the proximity of the source to the antenna array introduces unique challenges. By combining the PAST algorithm with sub-array processing, we

achieved a delicate balance between computational efficiency and localization accuracy. Our method exhibited superior performance in terms of precision, as evidenced by the CDF curves and RMSE metrics.

One of the notable advantages of our approach is its reduced computational burden, making it well-suited for scenarios with limited computational resources. The comparative analysis against established techniques like 2D-IFFT and ESPRIT highlighted the robustness and reliability of our proposed method, particularly in noisy environments with low SNRs.

- *3D Source Location in Near Field* In the second part of our research, we explored 3D-P estimation using URAs and advanced signal processing techniques. Leveraging HOSVD, Taylor approximation, and the Levenberg-Marquadt algorithm, we developed a sophisticated algorithm capable of accurate 3D source localization in challenging near-field environments. Notably, while relying solely on ESPRIT for angle estimation, This methodological evolution was particularly evident in the algorithm’s ability to estimate distance with higher accuracy and reliability in 3D scenarios compared to 2D scenarios. The incorporation of the Jacobian matrix, computed from spatial signal gradients, played an important role in refining position estimates, especially in challenging near-field environments with interference multipath scenarios.

Our comprehensive evaluation metrics, including CDFs and RMSE, demonstrated the algorithm’s adaptability and robustness across varying signal strengths and distances from the base station. The algorithm consistently maintained low error rates, showcasing its proficiency in diverse scenarios and its potential for real-world deployment.

## 8.2 FUTURE DIRECTIONS

In conclusion, our research has contributed valuable insights and innovative methods to the field of source localization in near-field scenarios. The combination of advanced algorithms, subarray processing, and adaptive techniques has paved the way for enhanced accuracy, reduced computational complexity, and improved performance in wireless communication systems.

Moving forward, future research endeavors will focus on further refining and optimizing the

proposed algorithms, especially focusing on the impact of noise power on HOSVD performance, a subspace method sensitive to rank selection. Although not optimized here, identifying this parameter could be a future research topic.

Another consideration in this work is that we extract azimuth and elevation from the first eigenvector of the second and third factor matrices of the tensor, assuming that the signal LOS power is significantly higher than the NLOS components. However, a low SNR makes the differentiation of LOS and NLOS challenging. Errors also arise from the reliability of iterative methods, dependence on the Jacobian matrix, the influence of the SNR on matrix conditioning, and convergence speed. These refinements in future work could make the localization method even more robust in terms of user location.

Additionally, as the landscape of wireless communication evolves, our research lays a solid foundation for addressing the challenges and requirements of emerging technologies, such as 6G networks.

## REFERENCES

- ABOUTANIOS, E.; HASSANIEN, A.; EL-KEYI, A.; NASSER, Y.; VOROBYOV, S. A. *et al.* *Advances in DOA estimation and source localization*. [S.l.]: Hindawi, 2017. Cited 2 times in pages 39 and 40.
- ABU-SHABAN, Z.; KEYKHOSRAVI, K.; KESKIN, M. F.; ALEXANDROPOULOS, G. C.; SECO-GRANADOS, G.; WYMEERSCH, H. Near-field localization with a reconfigurable intelligent surface acting as lens. In: IEEE. *ICC 2021-IEEE International Conference on Communications*. [S.l.], 2021. p. 1–6. Cited in page 5.
- BALANIS, C. A. Antenna theory: A review. *Proceedings of the IEEE*, IEEE, v. 80, n. 1, p. 7–23, 1992. Cited 3 times in pages 7, 8, and 15.
- BALANIS, C. A. *Advanced engineering electromagnetics*. [S.l.]: John Wiley & Sons, 2012. Cited 2 times in pages 11 and 12.
- BALANIS, C. A. *Antenna theory: analysis and design*. [S.l.]: John Wiley & Sons, 2016. Cited 7 times in pages iv, 9, 10, 11, 14, 15, and 16.
- BJÖRNSON, E.; DEMIR, Ö. T.; SANGUINETTI, L. A primer on near-field beamforming for arrays and reconfigurable intelligent surfaces. In: IEEE. *2021 55th Asilomar Conference on Signals, Systems, and Computers*. [S.l.], 2021. p. 105–112. Cited 3 times in pages iv, 61, and 62.
- BOLDRINI, J. L.; COSTA, S. I.; FIGUEREDO, V.; WETZLER, H. G. *Álgebra linear*. [S.l.]: Harper & Row, 1980. Cited in page 75.
- BRENA, R. F.; GARCÍA-VÁZQUEZ, J. P.; GALVÁN-TEJADA, C. E.; MUÑOZ-RODRIGUEZ, D.; VARGAS-ROSALES, C.; FANGMEYER, J. *et al.* Evolution of indoor positioning technologies: A survey. *Journal of Sensors*, Hindawi, v. 2017, 2017. Cited 3 times in pages 27, 29, and 37.
- CAPON, J. High-resolution frequency-wavenumber spectrum analysis. *Proceedings of the IEEE*, IEEE, v. 57, n. 8, p. 1408–1418, 1969. Cited 3 times in pages 41, 45, and 46.
- CEKLI, E.; CIRPAN, H. Unconditional maximum likelihood approach for near-field source localization. In: *ICECS 2001. 8th IEEE International Conference on Electronics, Circuits and Systems (Cat. No.01EX483)*. [S.l.: s.n.], 2001. v. 2, p. 753–756 vol.2. Cited in page 3.
- CHAKRABARTY, S.; HABETS, E. A. Multi-speaker doa estimation using deep convolutional networks trained with noise signals. *IEEE Journal of Selected Topics in Signal Processing*, IEEE, v. 13, n. 1, p. 8–21, 2019. Cited in page 4.
- CHALLA, R. N.; SHAMSUNDER, S. High-order subspace-based algorithms for passive localization of near-field sources. In: IEEE. *Conference record of the twenty-ninth asilomar conference on signals, systems and computers*. [S.l.], 1995. v. 2, p. 777–781. Cited in page 4.

- CHAN, S.; ZHANG, Z.; ZHOU, Y. A new adaptive kalman filter-based subspace tracking algorithm and its application to doa estimation. In: IEEE. *2006 IEEE International Symposium on Circuits and Systems*. [S.l.], 2006. p. 4–pp. Cited in page 72.
- CHEN, J.; HUDSON, R.; YAO, K. Maximum-likelihood source localization and unknown sensor location estimation for wideband signals in the near-field. *IEEE Transactions on Signal Processing*, v. 50, n. 8, p. 1843–1854, 2002. Cited 2 times in pages 3 and 70.
- CHEN, J.; ZHAO, F.; ZHOU, S.; TIAN, H. FDTD Simulation of Lightning Current along Vertical Grounding Rod Appended to a Horizontal Grounding grid. In: . [S.l.: s.n.], 2010. p. 1478–1481. ISBN 9781424456239. Cited 2 times in pages iv and 52.
- CHEN, S.; WANG, J.; LIN, T. High-resolution near-field source localization using compressive sensing and array interpolation. *IEEE Transactions on Antennas and Propagation*, v. 68, n. 6, p. 4387–4398, 2020. Cited in page 4.
- CHEN, Z.; GOKEDA, G.; YU, Y. *Introduction to Direction-of-arrival Estimation*. [S.l.]: Artech House, 2010. Cited 13 times in pages 39, 42, 43, 45, 47, 48, 49, 50, 52, 53, 55, 56, and 58.
- CICHOCKI, A.; ZDUNEK, R.; PHAN, A.; AMARI, S. *Nonnegative Matrix and Tensor Factorizations: Applications to Exploratory Multi-way Data Analysis and Blind Source Separation*. Wiley, 2009. ISBN 9780470747285. Disponível em: <<https://books.google.com.br/books?id=KaxssMiWgswC>>. Cited 4 times in pages v, 81, 82, and 83.
- CUI, M.; DAI, L. Near-field wideband beamforming for extremely large antenna arrays. *arXiv preprint arXiv:2109.10054*, 2021. Cited 2 times in pages 2 and 3.
- CUI, M.; WU, Z.; LU, Y.; WEI, X.; DAI, L. Near-field mimo communications for 6g: Fundamentals, challenges, potentials, and future directions. *IEEE Communications Magazine*, IEEE, v. 61, n. 1, p. 40–46, 2022. Cited 4 times in pages 1, 2, 59, and 62.
- DEY, N.; ASHOUR, A. S. *Direction of arrival estimation and localization of multi-speech sources*. [S.l.]: Springer, 2018. Cited 2 times in pages 39 and 40.
- EIBERT, T. F.; VOLAKIS, J. L. Fundamentals of antennas, arrays, and mobile communications. In: *Antenna engineering handbook*. [S.l.]: McGraw-Hill New York, NY, USA, 2007. p. 1–14. Cited 2 times in pages 7 and 13.
- ELZANATY, A.; GUERRA, A.; GUIDI, F.; ALOUINI, M.-S. *Reconfigurable Intelligent Surfaces for Localization: Position and Orientation Error Bounds*. 2020. Cited 2 times in pages 4 and 5.
- ELZANATY, A.; GUERRA, A.; GUIDI, F.; DARDARI, D.; ALOUINI, M.-S. Towards 6g holographic localization: Enabling technologies and perspectives. *IEEE Internet of Things Magazine*, IEEE, 2023. Cited 2 times in pages 18 and 80.
- EMENONYE, D.-R.; DHILLON, H. S.; BUEHRER, R. M. Ris-aided localization under position and orientation offsets in the near and far field. *IEEE Transactions on Wireless Communications*, v. 22, n. 12, p. 9327–9345, 2023. Cited in page 5.
- FOUTZ, J.; SPANIAS, A.; BANAVAR, M. *Narrowband direction of arrival estimation for antenna arrays*. [S.l.]: Springer Nature, 2022. Cited 4 times in pages 42, 47, 48, and 52.

- GEOK, T. K.; AUNG, K. Z.; AUNG, M. S.; SOE, M. T.; ABDALIZ, A.; LIEW, C. P.; HOSSAIN, F.; TSO, C. P.; YONG, W. H. Review of indoor positioning: Radio wave technology. *Applied Sciences*, MDPI, v. 11, n. 1, p. 279, 2020. Cited 5 times in pages 28, 31, 32, 33, and 35.
- GEZICI, S. A survey on wireless position estimation. *Wireless personal communications*, Springer, v. 44, p. 263–282, 2008. Cited 3 times in pages 27, 28, and 33.
- GOLUB, G. H.; LOAN, C. F. V. *Matrix computations*. [S.l.]: JHU press, 2013. Cited 2 times in pages 54 and 55.
- GROSICKI, E.; ABED-MERAIM, K.; HUA, Y. A weighted linear prediction method for near-field source localization. *IEEE Transactions on Signal Processing*, IEEE, v. 53, n. 10, p. 3651–3660, 2005. Cited in page 4.
- GUERRA, A.; GUIDI, F.; DARDARI, D.; DJURIĆ, P. M. Near-field tracking with large antenna arrays: Fundamental limits and practical algorithms. *IEEE Transactions on Signal Processing*, v. 69, p. 5723–5738, 2021. Cited in page 4.
- GUSTAFSSON, F. Particle filter theory and practice with positioning applications. *IEEE Aerospace and Electronic Systems Magazine*, v. 25, n. 7, p. 53–82, 2010. Cited 2 times in pages 4 and 5.
- HAARDT, M. Efficient one-, two-, and multidimensional high-resolution array signal processing. *Ph. D. Thesis, Shaker Verlag, Aachen*, 1996. Cited in page 53.
- HE, H.; WANG, Y.; SAILLARD, J. Near-field source localization by using focusing technique. *EURASIP Journal on Advances in Signal Processing*, Springer, v. 2008, p. 1–9, 2008. Cited in page 64.
- HUANG, Y.-D.; BARKAT, M. Near-field multiple source localization by passive sensor array. *IEEE Transactions on antennas and propagation*, IEEE, v. 39, n. 7, p. 968–975, 1991. Cited 3 times in pages 3, 59, and 70.
- HUANG, Z.; XUE, B.; WANG, W.; DONG, F.; WANG, D. A low complexity localization algorithm for mixed far-field and near-field sources. *IEEE Communications Letters*, IEEE, v. 25, n. 12, p. 3838–3842, 2021. Cited in page 3.
- HUSAIN, B.; STEEG, M.; STÖHR, A. Estimating direction-of-arrival in a 5g hot-spot scenario using a 60 ghz leaky-wave antenna. In: IEEE. *2017 IEEE International Conference on Microwaves, Antennas, Communications and Electronic Systems (COMCAS)*. [S.l.], 2017. p. 1–4. Cited in page 39.
- IEEE Standard for Definitions of Terms for Antennas. *IEEE Std 145-2013 (Revision of IEEE Std 145-1993)*, p. 1–50, 2014. Cited in page 8.
- JINGJING, P.; RAJ, S. P.; SHAOYANG, M. A search-free near-field source localization method with exact signal model. *Journal of Systems Engineering and Electronics*, BIAI, v. 32, n. 4, p. 756–763, 2021. Cited in page 59.
- JOURDAN, D. B.; DARDARI, D.; WIN, M. Z. Position error bound and localization accuracy outage in dense cluttered environments. In: *2006 IEEE International Conference on Ultra-Wideband*. [S.l.: s.n.], 2006. p. 519–524. Cited in page 77.

- KAMILARIS, A.; PRENAFETA-BOLDÚ, F. X. Deep learning in agriculture: A survey. *Computers and electronics in agriculture*, Elsevier, v. 147, p. 70–90, 2018. Cited in page 4.
- KARIYA, T.; KURATA, H. *Generalized least squares*. [S.l.]: John Wiley & Sons, 2004. Cited in page 54.
- KOLDA, T. G.; BADER, B. W. Tensor decompositions and applications. *SIAM review*, SIAM, v. 51, n. 3, p. 455–500, 2009. Cited in page 84.
- KORSO, M. N. E.; RENAUX, A.; BOYER, R.; MARCOS, S. Deterministic performance bounds on the mean square error for near field source localization. *IEEE Transactions on Signal Processing*, v. 61, n. 4, p. 871–877, 2013. Cited 2 times in pages 3 and 5.
- KRAUS, J. D. *Antennas mcgraw-hill*. New York, 1988. Cited 2 times in pages 7 and 13.
- KRIM, H.; VIBERG, M. Two decades of array signal processing research: the parametric approach. *IEEE signal processing magazine*, IEEE, v. 13, n. 4, p. 67–94, 1996. Cited 2 times in pages 41 and 43.
- LANDQVIST, R.; MOHAMMED, A. *The Projection Approximation Subspace Tracking Algorithm Applied to Whitening and Independent Component Analysis in Wireless Communications*. [S.l.: s.n.], 2005. Cited in page 73.
- LAVATE, T. B.; KOKATE, V.; SAPKAL, A. Performance analysis of music and esprit doa estimation algorithms for adaptive array smart antenna in mobile communication. In: *IEEE. 2010 Second International Conference on Computer and Network Technology*. [S.l.], 2010. p. 308–311. Cited 2 times in pages 3 and 52.
- LEE, S. Y.; CHANG, J.; LEE, S. Deep learning-based method for multiple sound source localization with high resolution and accuracy. *Mechanical Systems and Signal Processing*, Elsevier, v. 161, p. 107959, 2021. Cited in page 4.
- LI, J.; STOICA, P. *MIMO radar signal processing*. [S.l.]: John Wiley & Sons, 2008. Cited in page 33.
- LIBERTI, J. C.; RAPPAPORT, T. S. *Smart antennas for wireless communications: IS-95 and third generation CDMA applications*. [S.l.]: Prentice Hall PTR, 1999. Cited 2 times in pages 18 and 50.
- LIMA, C. D.; BELOT, D.; BERKVEN, R.; BOURDOUX, A.; DARDARI, D.; GUILLAUD, M.; ISOMURSU, M.; LOHAN, E.-S.; MIAO, Y.; BARRETO, A. N. *et al.* Convergent communication, sensing and localization in 6g systems: An overview of technologies, opportunities and challenges. *IEEE Access*, IEEE, v. 9, p. 26902–26925, 2021. Cited in page 80.
- LIN, L.; SO, H.-C.; CHAN, Y. T. Accurate and simple source localization using differential received signal strength. *Digital Signal Processing*, Elsevier, v. 23, n. 3, p. 736–743, 2013. Cited in page 36.
- LITVA, J.; LO, T. K. *Digital beamforming in wireless communications*. [S.l.]: Artech House, Inc., 1996. Cited in page 50.

- LIU, T.; FENG, H.; QIU, T.; LUAN, S.; ZHANG, J. Robust localization for near-and far-field signals with an unknown number of sources. *Fractal and Fractional*, MDPI, v. 7, n. 2, p. 184, 2023. Cited in page 2.
- LIU, W.; XIN, J.; ZUO, W.; LI, J.; ZHENG, N.; SANO, A. Deep learning based localization of near-field sources with exact spherical wavefront model. In: IEEE. *2019 27th European Signal Processing Conference (EUSIPCO)*. [S.l.], 2019. p. 1–5. Cited in page 4.
- LIU, W.; YANG, Y.; XU, M.; LÜ, L.; LIU, Z.; SHI, Y. Source localization in the deep ocean using a convolutional neural network. *The Journal of the Acoustical Society of America*, AIP Publishing, v. 147, n. 4, p. EL314–EL319, 2020. Cited in page 4.
- LIU, Y.; WANG, Z.; XU, J.; OUYANG, C.; MU, X.; SCHOBER, R. Near-field communications: A tutorial review. *IEEE Open Journal of the Communications Society*, IEEE, 2023. Cited 4 times in pages 1, 2, 60, and 62.
- MARKOPOULOS, P. P.; CHACHLAKIS, D. G.; PRATER-BENNETTE, A. L1-norm higher-order singular-value decomposition. In: IEEE. *2018 IEEE Global Conference on Signal and Information Processing (GlobalSIP)*. [S.l.], 2018. p. 1353–1357. Cited in page 84.
- MAZOKHA, S.; NADERI, S.; ORFANIDIS, G. I.; SKLIVANITIS, G.; PADOS, D. A.; HALLSTROM, J. O. Single-sample direction-of-arrival estimation for fast and robust 3d localization with real measurements from a massive mimo system. In: IEEE. *ICASSP 2023-2023 IEEE International Conference on Acoustics, Speech and Signal Processing (ICASSP)*. [S.l.], 2023. p. 1–5. Cited in page 80.
- MILLIGAN, T. A. *Modern antenna design*. [S.l.]: John Wiley & Sons, 2005. Cited 2 times in pages 8 and 14.
- MOOR, B. D.; VANDEWALLE, J. *et al.* The application of higher order singular value decomposition to independent component analysis. In: *SVD and Signal Processing III*. [S.l.]: Elsevier, 1995. p. 383–390. Cited in page 84.
- OZTURK, C.; KESKIN, M. F.; WYMEERSCH, H.; GEZICI, S. Ris-aided near-field localization under phase-dependent amplitude variations. *IEEE Transactions on Wireless Communications*, v. 22, n. 8, p. 5550–5566, 2023. Cited in page 5.
- RAO, B. D.; ARUN, K. Model based processing of signals: A state space approach. *Proceedings of the IEEE*, IEEE, v. 80, n. 2, p. 283–309, 1992. Cited in page 53.
- ROY, R.; KAILATH, T. Esprit-estimation of signal parameters via rotational invariance techniques. *IEEE Transactions on acoustics, speech, and signal processing*, IEEE, v. 37, n. 7, p. 984–995, 1989. Cited 4 times in pages 41, 52, 53, and 57.
- RUI, L.; HO, K. Efficient closed-form estimators for multistatic sonar localization. *IEEE Transactions on Aerospace and Electronic Systems*, IEEE, v. 51, n. 1, p. 600–614, 2015. Cited in page 33.
- SAWADA, H.; MUKAI, R.; MAKINO, S. Direction of arrival estimation for multiple source signals using independent component analysis. In: IEEE. *Seventh International Symposium on Signal Processing and Its Applications, 2003. Proceedings*. [S.l.], 2003. v. 2, p. 411–414. Cited in page 39.

- SCHMIDT, R. Multiple emitter location and signal parameter estimation. *IEEE transactions on antennas and propagation*, IEEE, v. 34, n. 3, p. 276–280, 1986. Cited 5 times in pages 41, 42, 43, 49, and 50.
- SERGIO, D. P.; DINIZ, R. *Adaptive Filtering: Algorithms and Practical Implementation*. [S.l.]: Nowell, MA: Kluwer Academic Publishers, 2002. Cited in page 72.
- SHERMAN, J. Properties of focused apertures in the fresnel region. *IRE Transactions on Antennas and Propagation*, v. 10, n. 4, p. 399–408, 1962. Cited in page 61.
- SO, H. C.; CHAN, Y. T.; CHAN, F. K. W. Closed-form formulae for time-difference-of-arrival estimation. *IEEE Transactions on Signal Processing*, v. 56, n. 6, p. 2614–2620, 2008. Cited 2 times in pages 32 and 33.
- SONG, H.-L. Automatic vehicle location in cellular communications systems. *IEEE Transactions on Vehicular Technology*, IEEE, v. 43, n. 4, p. 902–908, 1994. Cited in page 35.
- STARER, D.; NEHORAI, A. Passive localization of near-field sources by path following. *IEEE Transactions on Signal Processing*, IEEE, v. 42, n. 3, p. 677–680, 1994. Cited in page 4.
- STOICA, P.; WANG, Z.; LI, J. Robust capon beamforming. In: IEEE. *Conference Record of the Thirty-Sixth Asilomar Conference on Signals, Systems and Computers, 2002*. [S.l.], 2002. v. 1, p. 876–880. Cited in page 45.
- TANGSHENG, X.; LI, W.; SONG, Z.; LINLIN, Z.; JIN, K.; WEI, C. Study on Online Calculation Method of Transmission Line Parameters. In: *11th IET International Conference on Developments in Power Systems Protection (DPSP 2012)*. Birmingham, UK: IET, 2012. v. 2, n. 2, p. 3–6. Cited 2 times in pages 49 and 51.
- TREES, H. L. V. *Optimum array processing: Part IV of detection, estimation, and modulation theory*. [S.l.]: John Wiley & Sons, 2002. Cited 7 times in pages iv, 18, 19, 20, 22, 23, and 24.
- VASEGHI, S. V. Adaptive filters. *Advanced Digital Signal Processing and Noise Reduction, Saeed V. Vaseghi Copyright© 2000 John Wiley & Sons Ltd ISBNs: 0-471-62692-9 (Hardback): 0-470-84162-1 (Electronic)*, p. 205, 2000. Cited in page 72.
- VOLAKIS, J. L.; VOLAKIS, J. L. *Antenna engineering handbook*. [S.l.]: McGraw-hill New York, 2007. v. 1755. Cited 3 times in pages 14, 16, and 17.
- WEISS, A.; FRIEDLANDER, B. Range and bearing estimation using polynomial rooting. *IEEE Journal of Oceanic Engineering*, IEEE, v. 18, n. 2, p. 130–137, 1993. Cited in page 4.
- WYMEERSCH, H. A fisher information analysis of joint localization and synchronization in near field. In: *2020 IEEE International Conference on Communications Workshops (ICC Workshops)*. [S.l.: s.n.], 2020. p. 1–6. Cited 5 times in pages v, 4, 69, 74, and 76.
- YANG, B. Projection approximation subspace tracking. *IEEE Transactions on Signal processing*, IEEE, v. 43, n. 1, p. 95–107, 1995. Cited 4 times in pages 68, 72, 73, and 76.
- YANG, X. *Direction of Arrival Estimation with Coprime Arrays*. Tese (Theses) — UNIVERSITE DE NANTES, nov. 2020. Disponível em: <<https://hal.science/tel-03035464>>. Cited 8 times in pages iv, 19, 20, 22, 23, 24, 25, and 54.

YANG, Y.; MA, J.; DAWALIBI, F. P. An Efficient Method for Computing the Magnetic Field Generated by Transmission Lines with Static Wires. In: *Proceedings. International Conference on Power System Technology*. Kunming, China: IEEE, 2002. p. 871–875. ISBN 0780374592. Disponível em: <<https://ieeexplore.ieee.org/document/1047524>>. Cited in page 56.

YUEN, N.; FRIEDLANDER, B. Performance analysis of higher order esprit for localization of near-field sources. *IEEE transactions on Signal Processing*, IEEE, v. 46, n. 3, p. 709–719, 1998. Cited in page 4.

ZEKAVAT, R.; BUEHRER, R. M. *Handbook of position location: Theory, practice and advances*. [S.l.]: John Wiley & Sons, 2011. v. 27. Cited 9 times in pages 27, 28, 29, 30, 31, 32, 33, 37, and 38.

ZHI, W.; CHIA, M. Y.-W. Near-field source localization via symmetric subarrays. *IEEE Signal Processing Letters*, v. 14, n. 6, p. 409–412, 2007. Cited 7 times in pages v, 4, 63, 65, 69, 74, and 76.

ZHOU, X.; ZHU, F.; JIANG, Y.; ZHOU, X.; TAN, W.; HUANG, M. The simulation analysis of doa estimation based on music algorithm. In: *2020 5th International Conference on Mechanical, Control and Computer Engineering (ICMCCE)*. [S.l.: s.n.], 2020. p. 1483–1486. Cited in page 3.

ZUO, W.; XIN, J.; LIU, C.; ZHENG, N.; SANO, A. Improved capon estimator for high-resolution doa estimation and its statistical analysis. *IEEE/CAA Journal of Automatica Sinica*, IEEE, v. 10, n. 8, p. 1716–1729, 2023. Cited in page 45.